Optimizing the Observation Schedule of the JANUS Instrument to Improve the Jovian System Ephemerides

Master Thesis

by

Floor Melman

TU Delft

Delft University of Technology

Optimizing the Observation Schedule of the JANUS Instrument to Improve the Jovian System Ephemerides

Master Thesis

by

F.T. Melman

to obtain the degree of Master of Science
at the Delft University of Technology,
to be defended publicly on Wednesday November 28, 2018 at 01:00 PM.

Student number:	4229223	
Project duration:	May 18, 2018 – November 28, 2018	
Thesis committee:	Prof.dr. L.L.A. Vermeersen,	TU Delft, Committee chair
	Dr.ir. D. Dirkx,	TU Delft, Supervisor
	Dr. R. Fónod,	TU Delft, External examinator

This thesis is confidential and cannot be made public until December 31, 2021.

TU Delft

Preface

Jupiter and its moons have always been intriguing to me. There were numerous occasions that while observing the night sky and the planets, that I spotted Jupiter and thought: "*that little dot over there, that is the thing I am working on*." This is also what I liked about my thesis. It combines both the physical aspects of Jupiter and its moons, something you can see on a daily basis, with the engineering skills that are required to unveil its mysteries.

This thesis has been written to fulfill the requirements of the degree of Master of Science at the faculty of Aerospace Engineering at the Delft University of Technology. The work was completed over the course of 6 months including a three week holiday. The project was undertaken as a part of PRIDE (Planetary Radio Interferometer and Doppler Experiment), an experiment related to the JUpiter ICy moons Explorer (JUICE) at the request of my supervisor Dr.ir.D.Dirkx. Before presenting the work, I would like to thank those persons without which this thesis would not have been possible.

First of all, I would like to thank my supervisor Dr.ir.D.Dirkx for his guidance throughout the project. The weekly meetings were essential for the discussions on the different possible approaches and to provide confidence that I was heading in the right direction. I am especially thankful for the flexibility provided with regards to the tight graduation deadline which was required related to my next adventure in my professional career. Furthermore, I would like to thank Vidhya Pallichadath for the discussions regarding the observation planning and segmentation of the JUICE mission phases as well as providing me with very useful trajectory documents.

I also would like to thank my friend and fellow student Victor Trees for his support and the fruitful discussions we had regarding our theses. Finally, I would like to thank my friends and family for the support throughout my studies in Delft. Without them my time here would not have been such a great experience.

F.T. Melman
Delft, November 2018

Summary

The JUpiter Icy moons Explorer (JUICE) will visit Jupiter and its icy moons (Europa, Ganymede, and Callisto) and will study, among others, the ability of these icy moons to sustain life. An important condition for life is the availability of liquid water. Due to the relative large eccentricity of the orbits of the icy moons, they experience substantial tidal heating. This has resulted in the depletion of water on Io and the presence of a subsurface ocean on Europa and Ganymede. The eccentricity is maintained by the Laplace resonance for which the orbital periods of the moons Io, Europa, and Ganymede fit the ratio 1:2:4. Consequently, the moons experience an accumulating force during each cycle of the Laplace resonance imposed by the other moons such that relatively high eccentricities are maintained in this system. Thus, studying the Laplace resonance as well as the tidal characteristics of the moons can unveil detailed information regarding their interiors and their ability to sustain life. Both the Laplace resonance and the tides can be observed by their respective signature on the orbital dynamics of the moons.

To this end, the JUICE spacecraft is equipped with different instruments of which the 3GM (Gravity and Geophysics of Jupiter and the Galilean moons) and JANUS camera are of prime interest for this thesis. Furthermore, an additional experiment called PRIDE (Planetary Radio Interferometer and Doppler Experiment) is relevant but requires no on-board hardware. The 3GM and PRIDE experiments will generate range, range-rate, and lateral position observations during the 29 flybys of the Galilean moons (approximately lasting 2.5 years) and will provide up to 8 hours of tracking of the spacecraft each day during the Ganymede orbital tour. The Ganymede orbital tour will have a duration of approximately 1 year and will consist of a highly eccentric orbit phase as well as a low circular orbit phase at an altitude of 500 kilometer. The previously mentioned observations can be used to estimate, among others, the ephemerides[1] of the moons and the parameters related to tidal dissipation.

Previous studies, however, have shown that the lack of flybys of Io and the fact that the two Europa flybys are separated in time by only two weeks results in an unstable solution of the normal equations (the equations necessary to estimate the positions of the moon and the tidal parameters). This is related to the fact that the dynamics of especially Io and to a lesser extend Europa have to be estimated from their corresponding signature on the orbit of Ganymede. These signatures are present as a result of the Laplace resonance. Therefore, optical space-based astrometry of especially Io (using the JANUS camera) is required to stabilize the solution to the normal equations. Optical space-based astrometry is expected to be more effective in stabilizing the solution (or reducing the condition number, which is a measure of the stability of a problem) when its observation schedule is optimized. The optimization of the observation schedule is the goal of this thesis. Furthermore, the influence of the optimized observation schedule on the formal errors of especially Io is assessed. The formal error provides a measure of how the uncertainty in the estimated states is affected by the observational uncertainties and planning.

To this end, a large number of space-based astrometric observations were generated considering a number of operational constraints. Assuming a certain number of observations, the most suitable observations in reducing both the condition number and the formal error of the position of Io were selected by the NSGA-II algorithm (Non-dominated Sorting Genetic Algorithm II). As both the condition number and the formal errors are affected by weight (equal to the inverse of the squared observation uncertainty) of the corresponding observation, the uncertainty of the space-based astrometry was carefully assessed. For the JANUS camera, the errors in determining the center-of-figure of a detected moon are expected to dominate the total uncertainty. This is partially related to the relatively large field-of-view which will enable the detection of more reference stars. The latter is required for precise calibration of the image. However, the current models predicting the uncertainty, by which the center-of-figure of an imaged moon can be determined, are not unambiguously defined. Therefore, a hybrid method was assumed which was based on multiple models aiming to provide the most accurate representation of the current state-of-the-art.

[1] Tabulated positions of a celestial body for a given period in time.

Optimizing the observation epochs resulted in the condition number to be reduced by almost two orders of magnitude (from $6.2 \cdot 10^{16}$ to $5.1 \cdot 10^{14}$). This is however not enough to be able to retain at least one significant digit in case double precision is used. However, due to ambiguity in both the estimation of the observation uncertainty of the space-based astrometry and the uncertainty with which the position of JUICE can be determined, the actual attainable condition number can be either higher or lower. Nevertheless, the optimized epochs were found to be preferentially distributed among the closest approaches of JUICE with respect to Io. This is directly related to the high sensitivity of the observation with respect to the estimated states during these epochs. Furthermore, the accuracy by which the lateral position of the moon can be determined is lower in case the moon is observed at a close distance. Finally, the space-based astrometry of Europa was found to be of secondary importance which is illustrated by the fact that only 10 % of the optimized epochs were devoted to Europa.

The assessment of the resulting formal errors showed that the uncertainty with which the position of Io can be determined is substantially improved (by an order of magnitude) by the inclusion of space-based astrometry. This is related to the fact that these observations provide the only direct observations of Io which present a clearer signature on its dynamics. The formal errors of both Europa and Ganymede were also improved. The improvement of the formal errors of Ganymede is a result of the signature of the orbit of Ganymede in the observed dynamics of Io as no direct astrometry was present for Ganymede. Finally, no improvement of the formal errors was observed for Callisto which is related to the limited dynamic coupling between Callisto and the other moons.

Consequently, the fact that the optimized epochs are preferentially distributed along the closest approaches of JUICE with respect to Europa can be used by mission designers to plan the observational schedule of JANUS accordingly. This knowledge, combined with further research which is required on the actual number of recommended space-based astronomic observations, can potentially further stabilize the solution. In this way, the dynamics of the Galilean moons and the associated parameters can be estimated with an unprecedented accuracy which will unveil new information regarding the ability of the icy Galilean moons to sustain life.

Contents

1 Introduction

This chapter gives some required introductory background information in Section 1.1. Consequently, Section 1.2 poses the research questions that will be addressed in this thesis after which Section 1.3 presents an outline of the report.

1.1. Introductory Background Information

Already in 1610, Galileo Galilei discovered Jupiter and its four largest moons[1], which are therefore called the Galilean moons. Nowadays, Jupiter is the most visited outer-planet in the Solar System. The Jovian system was first visited by Pioneer 10 and 11 and Voyager 1 and 2. These missions only performed flybys but already made important discoveries and found numerous new moons. Three other spacecraft (Ulysses, Cassini, and New Horizons) performed flybys of Jupiter on their way to their final target. From 1995 to 2003 the Galileo spacecraft studied the Jovian system (including the moons and the rings) extensively.[1] Currently NASA's Juno spacecraft is orbiting Jupiter and studies, among others, Jupiter's gravity field in great detail. In May 2012 the JUICE (acronym for JUpiter ICy moons Explorer) mission was selected by the European Space Agency (ESA) as part of the Cosmic Vision Program 2015-2025 (Grasset et al. 2013). The JUICE mission will investigate the Jovian system in great detail, during the years 2030 to 2033, with a great emphasis on Galilean moon Ganymede which might potentially offer conditions for life. Furthermore, the JUICE spacecraft will also investigate Ganymedes neighboring moons Europa and Callisto in detail to check their potential to sustain life (Grasset et al. 2013).

The JUICE spacecraft carries a total of eleven experiments [2] of which the PRIDE experiment is of particular interest for this thesis. PRIDE is an acronym for Planetary Radio Interferometer and Doppler Experiment and is unique in the sense that it does not require any additional on-board hardware (Dirkx et al. 2017). It only requires hardware which is already available for communications and tracking. Furthermore, PRIDE uses the hardware of the 3GM experiment (acronym for Gravity and Geophysics of Jupiter and the Galilean moons. The data acquired by 3GM and PRIDE can be used to estimate the ephemerides of the Galilean moons (Io, Europa, Ganymede, and Callisto) in great detail. These ephemerides can, among others, be used to acquire information regarding the interior structure, composition, and rheology of the moons (Dirkx et al. 2016). For example, the estimation of the parameters that determine the amount of tidal dissipation in the moons yields valuable information regarding the thickness of the icy layer and the subsurface oceans on both Europa and Ganymede. Subsequently, this information can be used to model the evolution of the Jovian system or extrapolated to other planetary systems.

Until now, the dynamics of Jupiter and the Galilean moons were primarily determined using astrometric observations, supplemented by by radiometric tracking data from spacecraft that have visited

[1] NASA Science "Exploration | Jupiter - Solar System Exploration" solarsystem.nasa.gov `https://solarsystem.nasa.gov/planets/jupiter/exploration/?page=0&per_page=10&order=launch_date+desc%2Ctitle+asc&search=&category=33&tags=Jupiter` (accessed April 9, 2018)

[2] ESA Science & Technology"ESA Science & Technology: JUICE - Science Payload" sci.esa.int `http://sci.esa.int/juice/50073-science-payload/` (accessed April 9, 2018)

Jupiter such as the Galileo and Voyager missions. The JUICE mission provides radio tracking data and space-based optical astrometry, using either the JANUS camera system or the navigation camera (NavCam), over the course of its nominal mission lifetime of 3.5 years. The radiometric tracking data, complemented by both Earth- and space-based astrometry can be used to estimate the dynamics of the Galilean moons with an extraordinary accuracy (Dirkx et al. 2017). This allows a more detailed analysis of the physical properties of the Jovian system of which tidal dissipation in Io and Jupiter might be the most interesting.

A thorough study by Dirkx et al. (2017), however, has shown that using only the radiometric tracking data results in an ill-conditioned or unstable solution. Condition numbers on the level of 10^{16} were found such that no significant digits are retained using double precision. The instability is a result of the fact that no flybys are planned for Io and only two closely separated flybys are planned for Europa (Dirkx et al. 2016). Thus, the radio tracking data of these flybys will not be able to show any significant behavior of Europa over the complete mission duration of JUICE. Therefore, the dynamics of Io and Europa have to be estimated from their corresponding signature in the dynamics of Ganymede through the Laplace resonance. Consequently, JUICE-based optical astrometry of especially Io and to a lesser extend Europa is required to stabilize the solution (i.e. reducing the condition number). Dirkx et al. (2017) state that optimizing the observation schedule of the JANUS camera system might potentially further reduce the condition number.

The goal of this thesis is to optimize the observation schedule for the JANUS optical astrometry such that the stability and quality of the generated ephemerides is improved. The former is achieved by minimizing the condition number while the latter can be accomplished by minimizing the formal errors of the initial states by means of a covariance analysis. To this end, the dynamics (point mass interactions, oblateness interactions as well as tidal interactions) will be modeled. Subsequently, using a linearization around a reference solution, the normal equations matrix can be generated which can be evaluated on both the condition number and formal errors. The covariance matrix, however, is sensitive to the weighing matrix which is inversely proportional to the measurement uncertainty squared. Therefore, the uncertainty of the optical JUICE-based astrometry needs to be modeled accurately considering, among others, the number of reference stars available for calibration. Optimization of the observation schedule of the JANUS camera is important for two reasons. First of all, the operational flexibility for JUICE is low, such that arbitrary JUICE-based astrometry would pose a disproportional demand on the available data volume and might conflict with other science operations. Secondly, optimization of the observation schedule may provide insight in the operational conditions which are required to stabilize the normal equations matrix.

As confirmed by Dirkx et al. (2017), the formal errors show a great variation with observation settings. Therefore, the sensitivity of the condition number to the observation settings (i.e. VLBI cadence, VLBI measurement uncertainty, JANUS cadence) will be assessed. This analysis will provide insight into the influence of a variety of observation and operational settings to the stability of the solution. This sensitivity analysis, together with the results of the optimized JANUS epochs, will be essential in the observational planning of especially the JANUS instrument. Similar to Dirkx et al. (2017), the orbit determination of the spacecraft is decoupled form the ephemeris generation to reduce the computational burden and improve interpretability of the results.

1.2. Research Questions

To be able to address the problem as defined above, one main research question as well as three sub-questions are defined.

Will optimization of the observation schedule of the JANUS instrument to complement the JUICE radiometric tracking data improve the estimation of the ephemerides of the Galilean moons in terms of stability of the solution and the uncertainty in the estimation?

- What is the impact of the range of illumination conditions of the different Galilean moons on the uncertainty of the observations (right ascension and declination) related to JUICE-based optical astrometry of the different Galilean moons?

- What is the impact of the optimization of the observation schedule of the JANUS instrument to complement the JUICE radiometric tracking data on the condition number of the normal equations?

- What is the impact of optimization of the observation schedule of the JANUS instrument to complement the JUICE radiometric tracking data on the formal errors of the ephemerides of the Galilean moons given that the condition number of the normal equations is sufficiently low?[3]

1.3. Outline of the Report

To answer the research questions as posed in the previous section the report is structured in the following way. Chapter 2 gives an overview regarding the physical processes that are relevant within this study. Furthermore, this chapter gives a general overview regarding the scientific objectives and the mission time-line of the JUICE mission. Chapter 3 discusses the relevant acceleration models required to fully model the dynamics of the Galilean moons as well as the most important considerations regarding the numerical propagation and integration. The tracking types relevant within the PRIDE experiment are subsequently discussed in Chapter 4 next to the applicable operational constraints. Furthermore, the method used to compute both the condition number and the formal errors is discussed in Chapter 5 as well as the method that is used to decouple the orbit determination of JUICE from the generation of the ephemerides. Moreover, the method to estimate the uncertainty of the optical astrometric observations is discussed in the same chapter. The approach that is used to optimize the observation schedule of the JANUS camera is discussed in Chapter 6 in addition to the different settings used for the sensitivity analysis as well as the most important background information regarding the optimization algorithm used within this thesis. The results of the required verification and validation which is necessary for the correct interpretation of the results can be found in Chapter 7. The results of the sensitivity analysis as well as the results of the optimization of the epochs for JANUS astrometry are presented and discussed in Chapter 8. Note that, however, the results from the analysis of the uncertainty model for the optical space-based astrometry are already discussed in Chapter 7 as part of the validation of the uncertainty model. Finally, the research questions are answered and recommendations are given in Chapter 9.

[3] A condition number for which at least one significant digit is retained when using double precision.

2

Scientific Background

To understand and generalize the results as presented in this report some scientific background is required. Therefore, Section 2.1 gives a general overview regarding the general properties and interiors of the Galilean moons. Subsequently, Section 2.2 discusses the principle of orbital resonances using a simplified system. This theory is then applied to the Laplace resonance in Section 2.3, which governs the dynamics of the inner Galilean moons. Subsequently, the principles of tidal interaction and tidal dissipation are discussed in Section 2.4. The effects on the corresponding orbit of the satellite are discussed in Section 2.5. Finally, the relevant background information regarding the JUICE mission is discussed in Section 2.6. This information provides, among others, the scientific relevance of this study within the scientific objectives of the JUICE mission.

2.1. Characteristics of the Galilean Moons

The current understanding of the Galilean moons is mostly based on observations made by the Galileo spacecraft. The most important equilibrium parameters found by Schubert et al. (2004), using the Galileo data, are presented in Table 2.1. Note that the terms forced and free eccentricity are introduced in Section 2.3. The former is a result of eccentricity forcing by the Laplace resonance (discussed in Section 2.2), while the latter has a primordial origin (as a result of the formation of the particular system). A visualization of the (modeled) interiors of the Galilean moons is given in Figure 2.1.

Table 2.1: Equilibrium radius and the forced and free eccentricity of the Galilean moons. The radii are from (Schubert et al. 2004) while the forced and free eccentricity for the three inner moons are from (Yoder 1979). The free eccentricity Callisto is from (Cassen et al. 1980). As Callisto is not part of the Laplace resonance it has no forced eccentricity.

Satellite	Radius [km]	e_{forced}	e_{free}
Io	1821.6 ± 0.5	0.0041	$1 \pm 2 \cdot 10^{-5}$
Europa	1565.0 ± 8.0	0.0101	$9 \cdot 10^{-4}$
Ganymede	2631.2 ± 1.7	0.0006	0.0015
Callisto	2410.3 ± 1.5	n/a	0.0074

The Galilean moons are mostly composed of the elements metal, rock and water. An exemption to this is Io, which contains no water. As can be seen in Figure 2.1, the innermost three moons are stratified into layers. Io contains an iron core and a silicate or rocky mantle. Subsequently, Europa and Ganymede are stratified in a similar fashion, but also include a water ice-liquid shell which surrounds the rocky mantles (Schubert et al. 2004). Intriguingly, Schubert et al. (2004) show that the three inner Galilean satellites are comparable in size and internal structure if the water shells are removed from Europa and Ganymede. In this sense, Callisto is fundamentally different as it lacks an iron core and shows only partial stratification resulting in its constituents (water, rock and metal) being intimately mixed throughout its interior (Schubert et al. 2004).

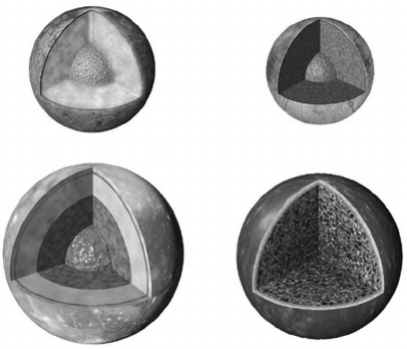

Figure 2.1: Modeled interiors of the Galilean moons showing stratification in layers for Io, Europa and Ganymede and partial stratification for Callisto (Schubert et al. 2004). From left to right and from top top bottom respectively Io, Europa, Ganymede, and Callisto are shown.

2.2. Orbital Resonance

The Galilean moons are one of the various systems in our Solar System which are trapped in an orbital resonance. For the inner three Galilean moons this means that the ratio of their orbital periods fits the ratio 1:2:4. Thus, as Ganymede orbits Jupiter once, Europa orbits Jupiter twice and Io orbits Jupiter four times. A result of this resonance is that Io overtakes Europa at the same location every orbit. This location is called the longitude of conjunction, referring to the point in which the two satellites and the central planet are aligned. Resonances tend to enhance the eccentricity and therefore have a significant influence on tidal heating within the Jovian system (the latter will be discussed in Section 2.4.2).

In this section, the principle of the Laplace resonance will be briefly discussed. For a thorough discussion on orbital resonances, the interested reader is referred to Greenberg (2010). The principle of orbital resonance can be explained by considering a simple case of two satellites orbiting a central planet as shown in Figure 2.2.

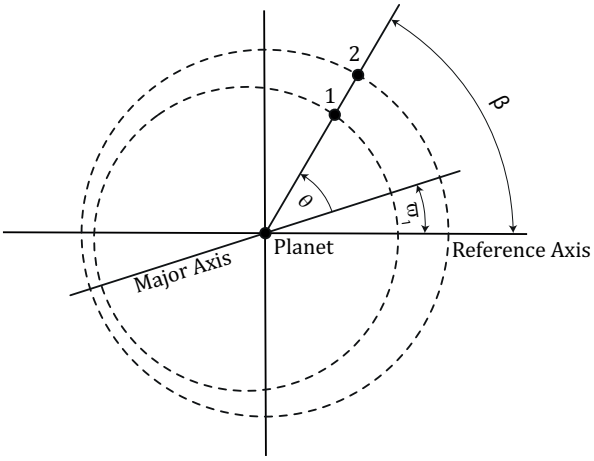

Figure 2.2: Geometry of a simplified orbital resonance near a ratio 1:2. Note that β represents the longitude of conjunction.

In this figure the first satellite has a slightly eccentric orbit, where the second satellite has a circular orbit. Furthermore, the first satellite is considered to behave as a test particle such that it does not have any influence on the second satellite. Finally, both satellites are in a 1:2 commensurable orbit such that the orbital period of the second satellite is twice the orbital period of the first satellite. Due to the commensurable nature of these orbits the longitude of conjunction is constant. The force imposed on the first satellite imposed by the second satellite is relatively small with respect to the gravitational force imposed by the central planet. However, due to the commensurable nature of both orbits and the fact that the magnitude of this force is largest at the longitude of conjunction, this force accumulates

and gradually modifies the orbit of the first satellite (Greenberg 2010).

At this point, two cases can be considered. In the first case, the longitude of conjunction is located before apocenter and after pericenter (the case shown in Figure 2.2). In this case the second satellite tends to increase the eccentricity of the first satellite (Greenberg 2010) as it gives an additional pull on a body which is already moving outward with respect to the central body (meaning that the radial velocity is positive). On the other hand, for the second case in which the conjunction occurs after apocenter but before pericenter the eccentricity is reduced (as the radial velocity of the first satellite is negative). The latter is mathematically illustrated by Equation 2.1 (Greenberg 2010).

$$\frac{de_1}{dt} \propto \sin\theta \tag{2.1}$$

The force imposed on the first satellite by the second satellite not only changes the eccentricity, it also tends to change the longitude of pericenter ($\bar{\omega}_1$ in Figure 2.2) which is mathematically described by Equation 2.2 (Greenberg 2010).

$$\frac{d\bar{\omega}_1}{dt} \propto -\left(\frac{1}{e_1}\right)\cos\theta \tag{2.2}$$

The origin of the libration (oscillating motion) of the longitude of conjunction is discussed using the general principles which govern orbital resonances (as discussed at the beginning of this section). This discussion is based on the theory given by Greenberg (2010). For this example, it is assumed that the ratio of the orbital periods is slightly larger than 1:2, meaning that both satellites are not in perfect resonance. When the longitude of conjunction is located in the first quadrant after pericenter ($0 < \theta < \pi/2$), both the longitude of conjunction and the argument of pericenter are moving in the same direction at approximately the same rate. Given that $d\theta/dt = 0$, Equation 2.1 shows that the eccentricity of the first satellite should increase. Consequently, according to Equation 2.2 $d\bar{\omega}_1/dt$ becomes less negative. This causes the angle between the argument of pericenter and the longitude of conjunction to decrease. Thus, in general when the conjunction occurs in the semi-circle around pericenter, the pericenter is accelerated towards the longitude of conjunction. A similar principle holds for the semi-circle around apocenter. To this end, both the argument of pericenter and the angle θ between pericenter and the longitude of conjunction are librating about either $0°$ or $180°$. During such a period of libration the eccentricity varies periodically and adjusts the rate of change of the argument of pericenter (Greenberg 2010).

If the amplitude of this libration would be zero (imposing $\theta = d\theta/dt = 0$), the eccentricity would have a value such that the rate of change of the argument of pericenter would match the rate of change of the longitude of conjunction (this to ensure $\theta = 0$). This particular value of the eccentricity is called the 'forced' eccentricity (Greenberg 2010) (see Table 2.1 for the forced eccentricities of the Galilean moons). In case of a non-zero libration amplitude, the accompanying value of the eccentricity is called the 'free' eccentricity. The value of the forced eccentricity is dependent on the rate of change of the longitude of conjunction. This means that when the orbits of both satellites are close to the exact 1:2 ratio, according to Equation 2.2 the eccentricity should be large to ensure a low rate of change of the argument of pericenter, matching the low rate of change of the longitude of conjunction. The latter means that systems that are close to an exact commensurability ratio have a rather high forced eccentricity (Greenberg 2010).

A near 1:2 commensurability can also be expressed as $n_1 - 2n_2 = \nu$, where n_i are the mean orbital motion of satellite i (Murray and Dermott 1999) and ν denotes the amount by which the resonance is not exact. As previously discussed, a low value of ν (meaning the orbits of both satellite are close to exact resonance) results in a high forced eccentricity which is confirmed by checking Equation 2.2. Considering that the integral of the mean motion n_i returns the mean longitude λ_i, the longitude of conjunction θ can be expressed in terms of the mean longitudes as given in Equation 2.3.

$$\theta = 2\lambda_2 - \lambda_1 - \bar{\omega}_1 \tag{2.3}$$

Finally, the interaction between both satellites, enhanced by the 1:2 commensurability, modifies the mean motions n as can be seen in Equation 2.4 (Greenberg 2010).

$$\frac{dn_1}{dt} \propto e \sin\theta \tag{2.4}$$

Assuming that $\theta > 0$, Equation 2.4 shows that the mean motion of the first satellite should increase. Therefore, the variation of λ_1 also increases with respect to λ_2. Thus, according to Equation 2.3, θ should move back to $\theta = 0$. Consequently, it can be concluded that the mean motion has a stabilizing effect on the angle θ (Greenberg 2010).

The example discussed in this section only includes the effect of the second satellite on the first satellite. However, the first (inner) satellite has a similar effect on the second satellite and therefore the major axis of the orbit of the second satellite could be locked to conjunction in a similar way (Greenberg 2010). In the next section, the theory presented here is specified to be applicable for the Laplace resonance.

2.3. The Laplace Resonance

The Laplace resonance involves three of the four Galilean moons. Io, Europa, and Ganymede are involved in a 1:2:4 commensurability of their mean orbital motions. This is characterized by Equation 2.5 (Murray and Dermott 1999).

$$\begin{aligned} n_1 - 3n_2 + 2n_3 &= 0 \\ \phi_L = \lambda_1 - 3\lambda_2 + 2\lambda_3 &= 180^\circ \end{aligned} \tag{2.5}$$

The relation of the mean orbital motions is exactly equal to zero. However, the resonant argument ϕ_L librates about 180° with an amplitude of 0.175° and a period of 2059.6 days (Lainey et al. 2006).

The Laplace resonance consists of two resonance pairs. The orbits of Io and Europa are in a 2:1 commensurability characterized by Equation 2.6 (e.g. Greenberg 2010; Murray and Dermott 1999; Schubert et al. 2010). In this equation the first subscript denotes which pair is considered, where 1 is used for the Io/Europa pair and 2 for the Europa/Ganymede pair. The second subscript denotes from which satellite the argument of pericenter $\bar{\omega}_i$ is involved, where 1 indicates Io, 2 indicates Europa and 3 indicates Ganymede.

$$\begin{aligned} \theta_{11} = \lambda_1 - 2\lambda_2 + \bar{\omega}_1 \approx 0^\circ \qquad & \theta_{12} = \lambda_1 - 2\lambda_2 + \bar{\omega}_2 \approx 180^\circ \\ n_1 - 2n_2 = \nu & \end{aligned} \tag{2.6}$$

It can be seen that, as described in the previous section, the longitude of conjunction librates about the pericenter of Io's orbit and the apocenter of Europa's orbit. Furthermore, it can be noted that the rate of change of the argument of pericenter ν is equal for both Io and Europa.

The orbits of Europa and Ganymede are also in a 2:1 commensurability characterized by Equation 2.7 (e.g. Greenberg 2010; Murray and Dermott 1999; Schubert et al. 2010).

$$\begin{aligned} \theta_{22} = \lambda_2 - 2\lambda_3 + \bar{\omega}_2 \approx 0^\circ \qquad & \theta_{23} = \lambda_2 - 2\lambda_3 + \bar{\omega}_3 \text{ circulates through } 360^\circ \\ n_2 - 2n_3 = \nu & \end{aligned} \tag{2.7}$$

Comparing Equation 2.7 with Equation 2.6, the similarities between θ_{11} and θ_{22} can be observed (both angles librate about 0°). Most remarkable, ν (or amount by which the commensurability is not exact) is exactly the same for both pairs resulting in a similar rate of change of the argument of pericenter for both Io and Europa (Greenberg 2010). Furthermore, it can be noted that the longitude of conjunction with respect to the argument of pericenter of Ganymede (angle θ_{23}) does not librate about either pericenter or apocenter but circulates through 360°. The latter is a result of the initial conditions and thus the origin of this particular resonance.

Murray and Dermott (1999) state that the rate of change of the argument of pericenter $\bar{\omega}_i$ has a secular part as well as a resonant part, which correspond to a free eccentricity and a forced eccentricity (see Equation 2.4). The secular contribution is caused by the oblateness of Jupiter, where the

resonant contribution is due to the gravitational interaction between the satellite pairs. For θ_{11}, θ_{12}, and θ_{22} the free component has been damped out, resulting in a relatively low amplitude of the oscillations. However, for Ganymede, the free component dominates, corresponding to the circulation of θ_{23} (Greenberg 2010). The resonant argument ϕ_L (see Equation 2.5) is close to zero indicating that the system of the inner Galilean satellites is near to equilibrium state. This means that the tidal dissipation in Jupiter is balanced by the tidal dissipation in Io (Murray and Dermott 1999).

The sequence of conjunctions is visualized in Figure 2.3. When observing again the expressions for θ_{12}, θ_{22} in Equations 2.6 and 2.7, it can be seen that the conjunction of Io and Europa always takes place on the opposite side of Jupiter with respect to the conjunction of Europa and Ganymede. The latter is visualized in subfigures (a) and (c).

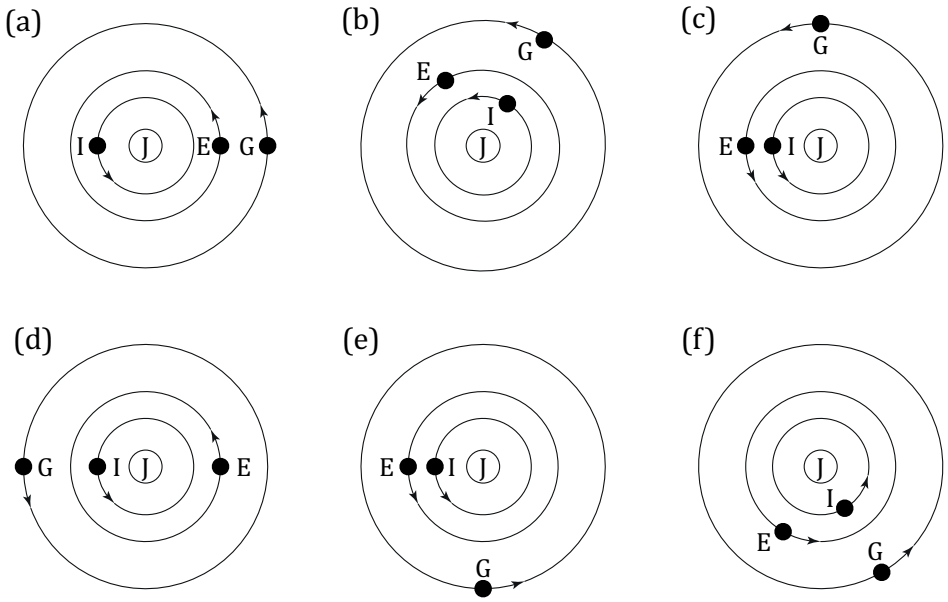

Figure 2.3: The relative geometry of the conjunctions occurring within the Jovian system. The configurations at times (a) $t = 0$, (b) $t = T_{rep}/6$, (c) $t = T_{rep}/4$, (d) $t = T_{rep}/2$, (e) $t = 3T_{rep}/4$, and (f) $t = 5T_{rep}/6$. Note that T_{rep} is the period of repetition of the conjunctions. The letters J, I, E, and G denote Jupiter, Io, Europa, and Ganymede respectively.

2.4. Tidal Interaction & Dissipation

To understand how the the improved ephemerides of the Galilean moons will enhance the knowledge regarding the interiors of the Galilean moons, basic knowledge regarding tidal interaction and dissipation is required. Therefore, the rotational and tidal deformation of a planetary body is discussed in Section 2.4.1, furthermore the principles of tidal dissipation within the Jovian system are discussed in Section 2.4.2.

2.4.1. Tidal & Rotational Deformation

Even without the presence of tides, planetary bodies deviate from an exact spherical shape as a result of rotational flattening (Hussmann et al. 2010). This gives rise to an equatorial bulge as can be seen in Figure 2.4(a). Next to an equatorial bulge, satellites possess a tidal bulge. Note that this section describes the tides raised by a planet on a satellite. However, similar behavior is observed for the tides raised by a satellite on a planet. A tidal bulge is the result of a differential in the gravity potential of the central planet on different parts of the satellite (or the other way around). This causes a periodic deformation represented as a tidal bulge which can be seen in Figure 2.4(b).

The orientation of the tidal bulge as shown in Figure 2.4, where the x axis is aligned with the sub-planet line (the line from the center of the satellite to the center of the planet), would only be possible for a satellite made of inviscid material. However, because of the viscosity of the material that comprises the satellite, friction occurs and tidal energy is transformed into heat (e.g. Greenberg 2010).

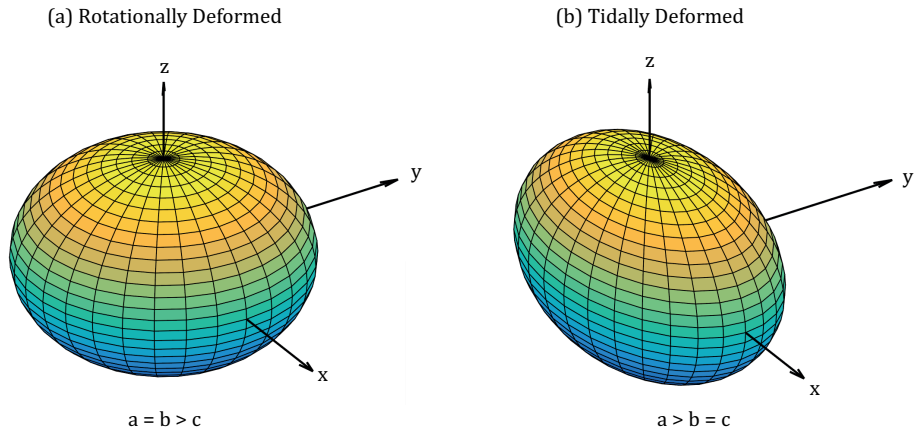

Figure 2.4: (a) Rotational deformation (b) tidal deformation, the body that raises the tide lies in the direction of the $\hat{x}$ axis. Note that this figure assumes no tidal dissipation.

This causes the tidal bulge to be misaligned with respect to the sub-planet line, resulting in a tidal lag angle. This will be further discussed in Section 2.5. Note that Figure 2.4 represents an equilibrium tide assuming a completely rigid, ocean-free, spherical planet which is orbited by one distant satellite. However, as discussed in Section 2.1, at least Europa and Ganymede are fully stratified and both are thought to possess a subsurface ocean, such that the outer ice shell is decoupled from the interior. Therefore, according to Murray and Dermott (1999), the tidal bulge of the ocean will not correspond to the equilibrium tide for Europa and Ganymede.

2.4.2. Tidal Dissipation in the Jovian System

Among the most important sources of energy on planetary bodies are radiogenic, potential (accretional), kinetic (rotational), deformation (tides), and chemical energy (Hussmann et al. 2010). This section will focus on tidal heating as a result of the generated kinetic energy. As discussed in Section 2.4.1, planetary bodies are distorted by both rotation and tides. However, rotation changes relatively slow with respect to the rate at which the tidal distortion occurs. Therefore, the deformation as a result of rotation is considered to be quasi-static (Hussmann et al. 2010). The dynamical deformation as a result of tides can lead to both elastic and plastic deformation which will result in dissipation of energy. The combination of plastic deformation with internal friction can generate substantial amounts of energy. This is especially relevant for satellites (like Io) which have an eccentric orbit close to the primary planet.

The effect of the eccentricity on the deformation of the tidal bulge is visualized in Figure 2.5 in a stationary rotating reference frame centered around the satellite. It shows how the ideal tidal bulge would orient itself along an eccentric orbit as the result of radial (Figure 2.5(a) and (c)) and librational tides (Figure 2.5(b) and (d)). The tide-raising effect is maximal at pericenter when the distance between both bodies is minimum. Consequently, at apocenter the tide-raising effect is minimal. This variation of the magnitude of the tidal bulge is called a radial tide. Furthermore, as the satellite moves along its eccentric orbit the direction of the tide raising potential is changed. This effect is called the librational tide.

Consequently, satellites in an eccentric orbit are subject to the variation of the gravitational and tidal forces over its orbital period. As the materials comprising the interior of the satellite are inelastic, part of the energy concerned in the tidal deformation as a consequence of the periodically changing tidal potential, is dissipated into heat (Hussmann et al. 2010). Therefore, the three inner Galilean moons have been affected by tidal heating over a longer time-scale as their eccentricities are maintained by the Laplace resonance (Greenberg 2010). As the tidal potential is dependent on both the mass and the distance towards the primary body, Io should experience the most significant tidal heating, followed by Europa which experiences less tidal heating, and Ganymede which is only marginally heated by tidal dissipation. This theory can be directly related to the observable differences between the three inner Galilean moons. Namely, the large amount of volcanic activity and the depletion of any water on

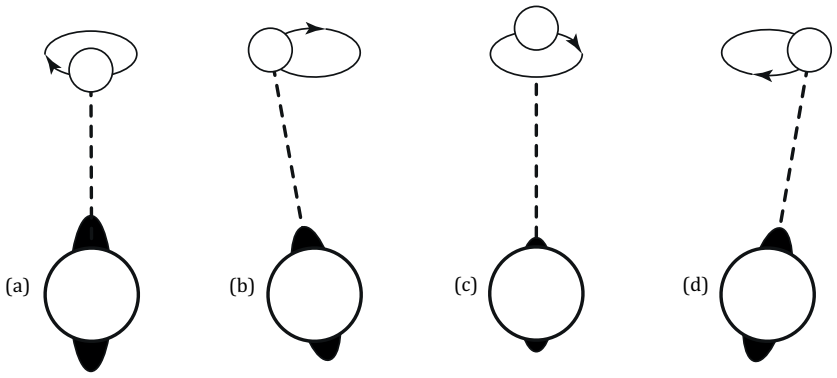

Figure 2.5: Tidal bulge shown schematically of the course of one orbit. The reference frame is centred on and rotates with the satellite.

Io, the thick liquid water layer and active surface reprocessing on Europa, and finally the marginally thermally driven processes on Ganymede are a direct consequence of tidal heating (Greenberg 2010). Furthermore, Callisto not being part of the Laplace resonance and located at a significantly larger distance from Io hardly experiences any tidal heating. This might be a explanation for the limited amount of interior stratification compared to the inner Galilean moons.

2.5. Tidal Interaction

As discussed in Section 2.4.1, tides are a result of the difference in the experienced gravitational accelerations on different parts of a body. Two types of tides can be considered. Tides raised on a planet by a satellite and tides raised on a satellite by a planet, which will be discussed in respectively Section 2.5.1 and 2.5.2. Both have an opposing effect on the eccentricity and semi-major axis (and consequently the mean orbital motion). The resulting equations describing the change in both the semi-major axis and eccentricity as a consequence of tides are discussed in Section 2.5.3.

2.5.1. Tides Raised on Jupiter

All the Galilean satellites raise tides on Jupiter. Because the orbital motion of the satellites is slower than the rotational speed of Jupiter ($\Omega_J > n_{sat}$) and dissipation (see Section 2.5) occurs inside Jupiter, the tidal bulge of Jupiter cannot instantaneously redirect itself to the changing tidal potential. Therefore the tidal elongation of Jupiter will be slightly ahead of the sub-planet line as can be seen in Figure 2.6 (e.g. Greenberg 2010; Hussmann et al. 2010; Murray and Dermott 1999). The angle between the tidal elongation and the sub-planet line is referred to as the tidal lag angle ϵ.

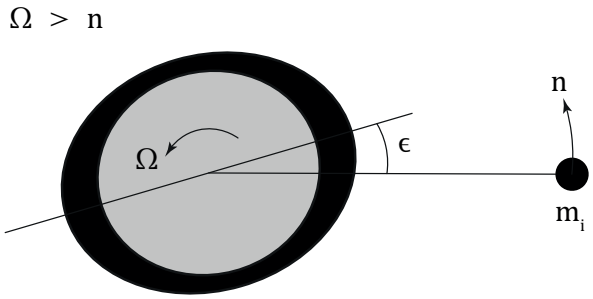

Figure 2.6: Visualization of the tidal lag angle ϵ as a result of tidal dissipation. For Jovian system, the rate of rotation of Jupiter is faster than the rotation rate of the tidally locked satellites ($\Omega > n$).

The result of the tidal elongation not being directed towards the sub-planet line is that the angular momentum of the orbit of the satellite and the rotation of Jupiter will be exchanged. In case the tidal bulge is slightly ahead of the sub-planet line, the rotation rate of the planet will be reduced while both the semi-major axis and the eccentricity of the satellite orbit will be increased (thereby reducing the mean orbital motion of the satellite) (e.g. Greenberg 2010). Note that the total amount of angular

momentum is conserved but not the total amount of orbital and rotational energy. This is the result of tidal dissipation in which orbital energy is dissipated into heat.

2.5.2. Tides Raised on the Satellites

The Galilean satellites are currently all tidally locked, meaning that their rotation rate has slowly evolved to an equilibrium state because of tidal dissipation in their interior. In equilibrium, the rotational rate of the satellites is synchronous with their orbital motion. This implies that the average rotation rate is constant. However, internal and external forces cause an oscillation of the rotational motion about its equilibrium value (Hussmann et al. 2010). The most contributing factor in this case is the eccentricity of the orbits of the satellites.

The eccentricity will have a dual influence on tidal dissipation. Firstly, the tidal torque acting on the satellite varies as the distance to Jupiter varies from pericenter to apocenter. Secondly, the rotational motion varies or librates due to the eccentricity of the orbit and the satellite pointing itself towards the empty focus of the orbit. However, as the rotation of the tidal bulge does not correspond to the rotation of the satellite, the satellite constantly changes it shape along the eccentric orbit. These effects are called radial and librational tides respectively (refer to Figure 2.5 Section 2.4.2 for a visualization of the radial and librational tides). The source of the tidal dissipation in the satellite is its orbital energy. Therefore, the tide raised in the satellite will reduce the semi-major axes (consequently increasing the mean orbital motion). Furthermore, because the orbital angular momentum is conserved, the eccentricity is reduced by the tides raised in the satellite (Hussmann et al. 2010).

2.5.3. Effect of Tides on the Orbit of the Satellites

The rate of change of the mean orbital motion of the satellite (accounting for both the tides raised in Jupiter and the satellite) is given by Equation 2.8 (Ferraz-Mello et al. 2008).

$$\dot{n}_{sat} = -c\left(\underbrace{1}_{\text{A}} - \left(\underbrace{7D}_{\text{B}} - \underbrace{12.75}_{\text{C}}\right)e^2\right)n \tag{2.8}$$

Where D and c are given below.

$$D = \left(\frac{Q}{k_2}\right)_J \left(\frac{k_2}{Q}\right)_{sat} \left(\frac{R_{sat}}{R_J}\right)^5 \left(\frac{m_J}{m_{sat}}\right)^2$$

$$c = \frac{9}{2}\left(\frac{R_J}{a}\right)^5 \left(\frac{k_2}{Q}\right)_J \left(\frac{m_{sat}}{m_J}\right) n$$

In this equation, R_J and R_{sat} are the equatorial radii of respectively Jupiter and the satellite in meters. Furthermore, m_J and m_{sat} are the masses of respectively Jupiter and the satellite. k_2 is the unitless second degree Love number, described by Greenberg (2010) as the factor that represents the effects of the physical response of the material comprising the planet or satellite on the amplitude of the tides, as well as the amplification of the tidal response due to the self-gravity of the planet's tidal deformation. The latter can be compared to the tide-raising potential of another (close-by) body that initializes the tidal deformation of the planet. Furthermore, the unitless Q represents the lag in the tidal response due to the internal dissipation and is related to the angle ϵ (see Figure 2.6) by $2\epsilon = Q^{-1}$ (Murray and Dermott 1999). k_2 and Q are often combined into a single parameter (Q/k_2). This parameter relates the physical properties and processes regarding the material that comprises either the planet or satellite to both the amplitude and lag of the tidal bulge. It can be estimated using observations, thereby unveiling information about the interiors of Jupiter and the Galilean moons. In Equation 2.8, part A and C account for the tides raised in Jupiter, where part B is the part which is caused by the tides raised in the satellite. Greenberg (2010) neglects part C as the eccentricity is rather small for the Galilean moons and is insignificant with respect to term A.

Subsequently, Equation 2.9 (e.g. Ferraz-Mello et al. 2008; Lainey et al. 2009; Yoder 1979) gives the rate of change of the semi-major axis accounting for both the tides raised on Jupiter and the tides raised on the satellites.

$$\dot{a} = \underbrace{+3\left(\frac{k_2}{Q}\right)_J \left(\frac{m_{sat}}{m_J}\right)\left(\frac{R_J}{a}\right)^5 na}_{\text{Tides raised on Jupiter}} \underbrace{-21\left(\frac{k_2}{Q}\right)_{sat} \left(\frac{m_{sat}}{m_J}\right)\left(\frac{R_{sat}}{a}\right)^5 nae^2}_{\text{Tides raised on Satellite}} \tag{2.9}$$

From Equation 2.9 it can be seen that the tides raised on Jupiter have an opposing effect to the tides raised on the satellite. However, the contribution of the tides raised on the satellite to the semi-major axis has a different format (i.e. not the same equation in which the parameters regarding Jupiter are replaced by the corresponding satellite parameters such as $(k_2/Q)_J$) compared to the contribution of the tides raised on Jupiter to the semi-major axis. This can be explained by the fact that the for tides raised on a satellite angular momentum cannot be exchanged between the orbit and the rotation of the satellite as the satellite is tidally locked. However, as discussed in Section 2.5.2, both the radial and librational tides give rise to changes in the semi-major axes. Therefore the second term in Equation 2.9 is different compared to the first term. A similar equation is found in literature for the rate of change of the eccentricity as a result of the tides raised on both Jupiter and the satellites. This relation is shown in Equation 2.10 (e.g. Ferraz-Mello et al. 2008; Lainey et al. 2009).

$$\dot{e} = \underbrace{+\frac{57}{8}\left(\frac{k_2}{Q}\right)_J \left(\frac{m_{sat}}{m_J}\right)\left(\frac{R_J}{a}\right)^5 ne}_{\text{Tides raised on Jupiter}} \underbrace{-\frac{21}{2}\left(\frac{k_2}{Q}\right)_{sat} \left(\frac{m_{sat}}{m_J}\right)\left(\frac{R_{sat}}{a}\right)^5 ne}_{\text{Tides raised on Satellite}} \tag{2.10}$$

As can be seen in Equations 2.8 to 2.10, the effects of tidal dissipation in the planet and in the satellite are opposing eachother (e.g. Hussmann et al. 2010). The resulting change in the semi-major axis and eccentricity is thus a result of the combination of both effects. Thus, observing the progression of the orbit of the satellites yields information regarding the parameters representing tidal dissipation. As discussed in Section 2.5.2, the eccentricity of the orbit gives rise to variations in the tidal bulge by means of radial and librational tides.

2.6. JUICE Mission Overview

To place this thesis, being part of the PRIDE (Planetary Radio Interferometry and Doppler Experiment), in the broader context of the JUICE mission, relevant background information is required. Therefore Section 2.6.1 gives the scientific background of the JUICE mission. Furthermore, the relevant scientific instruments will be briefly discussed in Section 2.6.2. Finally, the mission profile, which will be used to schedule the observations, will be discussed in Section 2.6.3.

2.6.1. Scientific Context

The JUICE mission was selected by the European Space Agency at the first large (L-class) mission within the Cosmic Vision Program 2015-2025 in May 2012 (Grasset et al. 2013). The Cosmic Vision program was issued in October 2005 and describes the most important science questions to which upcoming space missions should be devoted. Four themes were identified by solar system and astronomy communities. The first two themes are relevant within the context of the JUICE mission and are cited below (Grasset et al. 2013).

1. *"What are the conditions for planet formation and the emergence of life?"*
2. *"How does the Solar System work?"*

Within the context of this study on the generation of the ephemerides of the Galilean moons using PRIDE and supplementary JANUS astrometry, only the first theme is relevant. Grasset et al. (2013) define the following exploration priority within the first theme: *"Life and habitability in the Solar System: Explore in-situ the surface and subsurface of the solid bodies in the Solar System most likely to host - or have hosted -life. Explore the environmental conditions that make life possible"*. This objective is fully covered by JUICE as it will study the surface, subsurface and the subsurface water oceans of Ganymede, Callisto, and Europa, thereby significantly pushing the state-of-the-art of our understanding of the Jovian icy moons.

The habitability theme for the Galilean moons, as addressed in the first theme, has become relevant as soon as subsurface oceans on the Galilean moons were discovered using data form the Galileo mission (JUICE Science Study Team 2012). Habitability is defined as *"the potential of an environment (past or present) to support life of any kind"* (Grasset et al. 2013, and the references therein). Habitability does not directly implicate the existence of life in the past, present or future but instead refers to the environmental conditions which are necessary to harbor life (Grasset et al. 2013). Currently, habitability is thought to rely on four conditions: liquid water, biological essential elements (such as C, H, O, N, P, and S), energy and time (stability of the system). Consequently, assuming extrasolar planetary systems are comparable to our Solar System, icy satellites possessing a liquid subsurface ocean could be more prevailing habitats within the universe. Much more than Earth-like exoplanets as those require very specific conditions that allow the existence of a surface ocean (JUICE Science Study Team 2012).

The JUICE mission focuses on the characterization of the conditions previously mentioned that may have led to the evolution of the Jovian icy moons as habitable environments (JUICE Science Study Team 2012). To this end, JUICE will determine the amount of liquid water within the Jovian system. Furthermore, it will accomplish a characterization of the biologically essential elements present on the satellite surfaces. The JUICE mission will be focused on Europa, Ganymede, and Callisto as for these moons liquid water oceans have been proposed based on Galileo observations (e.g. Grasset et al. 2013). The focus on the icy moons and the harsh radiation environment explain the lack of proposed flybys of Io. Finally, JUICE aims to analyze the processes within the Jovian system which are necessary to ensure a stable environment (requirement for habitability) on geologic time-scales (JUICE Science Study Team 2012). One of these processes, as described in the previous section, is the gravitational coupling by the Laplace resonance. The tidal heating as a result of the eccentricity which is maintained by the orbital resonance might be an important heat source and thus a condition for habitability (Grasset et al. 2013).

The 3GM and PRIDE experiments will be used to contribute to the estimation of the parameters related to the aforementioned characteristics that are required to sustain life. For example, the thickness of the icy layer of both Europa and Ganymede is constrained by, among others, the tidal Love number k_2 and h_2, surface motions, the dynamical rotation state (especially librations) as well as the induced magnetic field. Using the 3GM data the both the second degree Love number k_2 as well as the libration amplitude can be determined. Combining this data with the data from the laser altimeter, the JANUS camera, and the magnetometers on JUICE, a hypothetical range of the thickness of both the ice shell and the subsurface ocean can be determined. The focus of PRIDE is mostly on the generation of the ephemerides which are necessary to study, among others, the evolution of the Laplace resonance.

Moreover, JUICE radiometric tracking complemented by Earth-based astrometry will provide constraints on the evolution of the Laplace resonance and tidal dissipation. As Earth-based astrometry is available over a period of more than 100 years (Lainey et al. 2009), it is able to capture a stronger signature on the effect of tidal dissipation (by estimating (k_2/Q)). This is related to the secular effect of tidal dissipation on the semi-major axis and eccentricity of the moons (as shown in Equation 2.9 and 2.10). Therefore the mean motion changes such that the effect on the longitude will be cumulative (Lainey et al. 2009, supplementary information) and the signature of tidal dissipation on the orbit increases quadratically in time (Dirkx et al. 2017).

Knowledge about the gravitational mutual interactions of the Galilean moons (precise and over longer time-scales) is essential in assessing the ability of the icy moons to sustain life. For example, Lainey et al. (2009) conclude that the orbit of Io is moving inward towards Jupiter and that the system is progressing out of the exact Laplace resonance. This has implications on the existence of the subsurface oceans of Europa and Ganymede and consequently on the presence of liquid water and the stability of the environment in the future (e.g. Grasset et al. 2013). Finally, knowledge about the evolution of the Laplace resonance will enable the testing of different hypotheses on the origin of the resonance. These hypotheses might, to a large extend, explain the large difference between the interiors of both Ganymede and Callisto as discussed in Section 2.1 and will improve the understanding of the orbital resonances in the Jovian system over geological timescales.

There are currently three major hypotheses that describe origin of the Laplace resonance. Firstly, Greenberg (1987) argue an primordial origin in which the just formed moons migrate into resonance as a result of interaction within the circumjovian disk. This would mean that the Laplace resonance is stable over very long times scales such that the subsurface oceans have been present on Europa and Ganymede on geological time-scales.

Secondly, the Laplace resonance could have be formed by distinct expansion of the orbits as a result of the tidal torques imposed by Jupiter (Yoder 1979). This assumes Io and Europa spiraling outwards as a results of the tidal torques induced by Jupiter. As the tidal torque is dependent on the distance to the planet, Io experiences higher tidal torques an thus moves outward at a higher velocity compared to Europa such that they can catch up in a 2:1 mean motion resonance (Schubert et al. 2010). Consequently, both Io and Europa spiral outwards together and catch up with Ganymede, thereby establishing the Laplace resonance. This would mean the moons were not constantly in resonance on geological time-scales such that the stability of their environments required to sustain life might have evolved in time.

Finally, Showman and Malhotra (1999) argue that the inner three Galilean moons might have passed through other three body resonances characterized by $(2n_2 - n_1)/(2n_3 - n_2) = 1/2$, 3/2 or 2 (Showman et al. 1997). These resonance can be restored to 1 for the Laplace resonance as a consequence of tidal torques. As a result of the different resonances, the forces eccentricity of Ganymede could have been as high as 0.01-0.02. The would enable significant tidal heating which can, potentially, explain why extensive resurfacing has occurred for Ganymede but not for Callisto (Schubert et al. 2010). However, the latter remains a "major puzzle" in planetary sciences (Showman and Malhotra 1999). This would mean the amount of tidal heating on the Galilean moons might have varied substantially over time, such that a stable environment (required to sustain life) might not have been present (or greatly varies) on geological time-scales.

2.6.2. Relevant Science Instruments

The JUICE mission carries a total of ten instruments which are used within eleven scientific experiments (the PRIDE experiment does not require any hardware on-board the spacecraft). For this study, only the JANUS and 3GM instruments are relevant as well as the PRIDE experiment.

The science contribution of 3GM is defined as follows: "*Interior state of Ganymede, presence of a deep ocean and other gravity anomalies. Ganymede and Callisto surface properties. Atmospheric science of Jupiter, Ganymede, Europa and Callisto, and Jupiter rings.*" (JUICE Science Study Team 2014). The 3GM instrument contains two elements which operate separately and independently. Those elements are the Ka-band transponder (KaT) and the ultra-stable oscillator (USO). Both elements are an integral part of the spacecraft Telemetry, Telecommunications and Command (TT&C) system and are both part of the JUICE radio science instrument package. 3GM observables are generated by tracking the JUICE spacecraft using the ESA ESTRACK stations resulting in two-way range and range-rate observations JUICE Science Study Team (2014) (for more details regarding the cadence and observational uncertainty of the 3GM observations, refer to Chapter 4). Note that the USO is only used for atmospheric observations and is thus irrelevant within this study. The KaT enables a Ka/Ka two-way link which is almost immune to noise caused by interplanetary plasma delay. The X/X and X/Ka radio links of the TT & C system are used to completely cancel the interplanetary plasma delay as discussed in more detail in Chapter 4. The heritage for the 3GM experiment, especially for the relatively new implementation of the Ka-band transponder, is derived from the BepiColombo radio science experiment (MORE) and the Juno Ka-band transponder (KaT) (JUICE Science Study Team 2014).

The JANUS instrument, on the other hand, is a camera system which is able to observe or asses: "*Local-scale geologic processes on Ganymede, Europa, and Callisto; Io Torus imaging, Jupiter cloud dynamics & structure. Global morphology or the Ganymede surface. Global to regional scale morphology of the Callisto and Europa surface. Physical and dynamical properties of minor moons and rings*" (JUICE Science Study Team 2014). The main science product of the JANUS experiment will be geo-referenced image maps of the Galilean moons including digital terrain models (JUICE Science Study Team 2014). The science return of JANUS relevant within this study are images which can be used for space-based optical astrometry as mentioned in the last sentence of the JANUS science contribution. These images will be used together with Earth-based astrometry and radio tracking data to determine the position and dynamics of the Galilean satellites. JANUS can work either with spacecraft inertial pointing or spacecraft slew motion. The latter is important to consider in the operations of generating space-based optical astrometry. The technical details of the JANUS camera will be discussed (together with the technical details of the NavCam camera) in Chapter 5. The JANUS instrument is based on heritage from cameras which were developed for the BepiColombo, DAWN, and Rosetta mission (JUICE Science Study Team 2014).

2.6.3. Mission Profile

The JUICE mission has 7 top level mission phases which are shown in Table 2.2. This table also shows the start and end date (in months) of the respective phase as well as the number of flybys for each moon. The presented mission phases correspond to the Consolidated Report on Mission Analysis (CReMA) version 3.2.

Table 2.2: Relevant science/mission phases of the JUICE mission corresponding to the CReMA 3.2 and CReMA 4.0 trajectories and launch option 141a (Boutonnet and Varga 2017). Note that the number of flybys per moon are given for respectively Io, Europa, Ganymede, and Callisto.

Phase		Start	End	Number of flybys per moon
1	Cruise/Interplanetary transfer	06-2022	10-2029	n/a
Jovian Tour				
2	Jupiter equatorial phase no 1/Energy reduction	10-2029	08-2030	0/0/4/0
3	Europa science	09-2030	10-2030	0/2/1/1
4	Jupiter high latitudes/Callisto science	11-2030	07-2031	0/0/1/9
5	Jupiter equatorial phase no 2 /Transfer to Ganymede	07-2031	08-2032	0/0/9/2
In-orbit around Ganymede				
6	Ganymede Elliptical Orbit (GEO)	09-2032	02-2033	Duration: 150 days
7	Ganymede Circular Orbit (GCO-500)	02-2033	06-2033	Duration: 130 days

The interplanetary transfer is performed using an Earth-Venus-Earth-Mars-Earth gravity assist to arrive at Jupiter approximately 7.4 years after launch. The Jovian tour lasts approximately 2.5 years after which the JUICE spacecraft orbits Ganymede for slightly less than a year. This relatively short duration of the Ganymede tour is related to the combination of the desired low circular orbit at 200 km at the end of the mission combined with the decreasing β angle (Grasset et al. 2013) (the β angle denotes the angle between the Sun and Ganymede and the orbital plane of JUICE). Consequently, the JUICE spacecraft will experience longer eclipses with respect to the total orbital period during the later phases of the Ganymede tour. Therefore, the batteries will deplete triggering the end of the mission. During phase 2 to 5 a large number of flybys of Callisto and Ganymede are planned as well as two Europa flybys. During the first 10 months, JUICE will be in an equatorial orbit around Jupiter and will primarily investigate Jupiter's atmosphere, magnetosphere and dynamics. This phase is followed by the Europa science which contains two flybys of Europa and which is initiated and terminated by respectively a Ganymede and Callisto flyby. Consequently, the inclination is increased to a maximum of 26° using multiple Callisto flybys (Grasset et al. 2013). This enables JUICE to observe the atmosphere and magnetosphere of Jupiter at higher latitudes. Furthermore, the Callisto flybys enable JUICE to observe the interior of Callisto. Thereafter, the Ganymede orbit phase is initiated by a Ganymede eccentric orbit. The latter will be reduced to a circular orbit at 5000 km altitude. After the first circular orbit phase, the orbit is lowered to a 500 km circular orbit using an elliptical orbit with a pericenter at 500 km in between both circular orbits.

During these phases, the different instruments on the JUICE spacecraft have to work concurrently to meet the imposed science requirements. As the operations of different instruments might conflict with each other, 18 operational modes have been identified by four working groups. Each working group identifies segments during the main mission phases, which are used to prioritize events which have a high priority in satisfying the science requirements. Based on the segments of all four science working groups an operational schedule can be defined. Currently, the Europa science and GCO500 phases are the sizing cases with respect to the required data-volume and power consumption (JUICE Science Study Team 2014). This means that acquiring space-based astrometry (using the JANUS camera) during or around the Europa flybys and/or the GCO500 orbit poses an additional challenge as the available data volume during these event is limited.

3

Simulating the Dynamics

To estimate the initial states of the Galilean moons and the associated model parameters, the dynamics of the moons need to be modeled. The accelerations considered for this thesis and the accompanying models are discussed in Section 3.1. The physical constants that are used for the respective gravitational, rotational, and tidal models are presented in Section 3.2. Finally, Section 3.3 discusses the most important considerations regarding the numerical integration as well as the used time and reference systems.

3.1. Simulating the Dynamics of the Galilean Moons

This section discusses the accelerations that are considered in the dynamical modeling of the states of the Galilean moons. First of all, Section 3.1.1 discusses the general considerations for the dynamical modeling of the satellites. Secondly Section 3.1.2 discusses the accelerations due to the point mass interactions between the different bodies after which the accelerations as a result of the extended bodies are discussed in Section 3.1.3. The considerations regarding the relativistic effects are discussed in Section 3.1.4. The accelerations as a result of the tidal interaction between Jupiter and the satellites, as discussed in Section 2.5, are given in Section 3.1.5. Finally, the complete equation of motion is summarized in Section 3.1.6.

3.1.1. General Considerations

The motion of the satellites is propagated with respect to a Jovicentric (centred at the center of mass of Jupiter) with inertial axes which are fixed and oriented with respect to ICRF (J2000) similar as in Dirkx et al. (2016) and Lainey et al. (2009). A more elaborate discussion on the reference frames used is given in Section 3.3.2. Furthermore, a notation similar to Lainey, Duriez and Vienne (2004) is used. In this notation a body is indicated as P_i with a mass m_i and that i denotes the body that is considered. In this particular case, Jupiter, Io, Europa, Ganymede and Callisto are represented by $i = 0$ to $i = 4$ respectively. Furthermore, the minor moons Amalthea, Thebe and Himalia are denoted by $i = 5$ to $i = 7$ respectively. For Jupiter (or a central body in general) $i = 0$, r_{ij} denotes the distance between body P_i and body P_j. The distance to the central body is only indicated with one index ($r_{i0} = r_i$). In the equations for perturbing forces or potentials, for example $F_{\bar{i}\hat{0}}$, the first index denotes the body affected and the second index denotes the affecting body (i.e. the body that generates the force or potential). A ponctual (point mass) body will be denoted by a bar $\bar{i}$, where an extended or oblated body will be denoted by a hat $\hat{i}$.

3.1.2. N-body Problem

Assuming N ponctual bodies P_i with mass m_i, orbiting around a central body P_0 (Jupiter in this case), Equation 3.1 (e.g. Lainey et al. 2009) gives the acceleration encountered by each body P_i.

$$\ddot{\vec{r}}_i = -\frac{G(m_0 + m_i)\vec{r}_i}{r_i^3} + \sum_{j=1, j\neq i}^{N} Gm_j \left(\frac{\vec{r}_j - \vec{r}_i}{r_{ij}^3} - \frac{\vec{r}_j}{r_j^3} \right) \tag{3.1}$$

In this equation the first term accounts for a regular Kepler orbit, where the second term accounts for ponctual third body perturbations. Furthermore, the first term differs slightly from notations usually found in literature in which m_i is usually neglected. However, m_i is included to ensure the reaction force on the central body induced by P_i considered. This is important when propagating the dynamics with respect to the center of mass of the central body instead of the barycenter of the planetary system.

3.1.3. Oblateness Accelerations

As the Galilean satellites orbit Jupiter at a relatively low altitude, the extended body interaction of both Jupiter on the satellites as well as the interaction of the satellites on Jupiter have to be considered. The acceleration encountered by a body P_i which is caused by the mutual extended body interactions is given by Equation 3.2 (e.g. Lainey et al. 2009; Lainey, Duriez and Vienne 2004). This equation comprises three terms: A, B, and C.

$$\ddot{\vec{r}}_i = G(m_0 + m_i) \left(\underbrace{\nabla_i U_{\bar{i}\hat{0}} - \nabla_0 U_{\bar{0}\hat{i}}}_{\text{A}} \right) + \sum_{j=1, j\neq i}^{N} Gm_j \left(\underbrace{\nabla_j U_{\bar{j}\hat{0}} - \nabla_0 U_{\bar{0}\hat{j}}}_{\text{B}} + \underbrace{\nabla_i U_{\bar{i}\hat{j}} - \nabla_j U_{\bar{j}\hat{i}}}_{\text{C}} \right) \tag{3.2}$$

In this equation U represents the gravity potential generated by the extended body. The first term of A represents the acceleration caused by the oblateness of the central body (Jupiter) which is encountered at the position of satellite P_i. The second term represents the oblateness effect of satellite P_i encountered by the central body. Term B represents similar accelerations as in A but now considering satellites P_j and the central body. These accelerations (the oblateness gravity field of Jupiter experience by P_j) are relevant as these accelerations directly influence the state of the third bodies required in, among others, the right hand term of Equation 3.1 for body P_i. Finally, term C represents the aforementioned accelerations for interacting satellites P_i and P_j. Lainey et al. (2009) neglect the second term of A (the oblateness gravity field of the satellite P_i received by Jupiter P_0), the second term of B (the oblateness gravity field of satellite P_j received by Jupiter P_0) and the term C (mutual interaction between the oblateness gravity field of both body P_i and P_j) completely as these therms are small with respect to the governing accelerations. The mutual extend body accelerations (otherwise referred to as figure-figure interactions) are already neglected in Equation 3.2 as these terms are very small (Dirkx et al. 2016; Lainey, Duriez and Vienne 2004). The gravitational potential $U_{\bar{i}\hat{0}}$ of extended body P_0, as acquired by ponctual body P_i is given by Equation 3.3 (Lainey et al. 2009). In this equation $U_{\bar{i}\hat{0}}^{(1)}$ represents the zonal harmonics and $U_{\bar{i}\hat{0}}^{(2)}$ represents the sectorial as well as the terresal harmonics.

$$U_{\bar{i}\hat{0}} = U_{\bar{i}\hat{0}}^{(1)} + U_{\bar{i}\hat{0}}^{(2)} \tag{3.3}$$

In this equation $U_{\bar{i}\hat{0}}^{(1)}$ is represented by Equation 3.4 and $U_{\bar{i}\hat{0}}^{(2)}$ by Equation 3.5.

$$U_{\bar{i}\hat{0}}^{(1)} = \sum_{n=2}^{\infty} -\frac{R_0^n}{r_i^{n+1}} J_n P_n(\sin\phi_k) \tag{3.4}$$

$$U_{\bar{i}\hat{0}}^{(2)} = \sum_{n=2}^{\infty} \frac{R_0^2}{r_i^{n+1}} \sum_{p=1}^{n} P_n^{(p)}(\sin\phi_k) \left[c_{np}\cos(p\lambda_k) + s_{np}\sin(p\lambda_k) \right] \tag{3.5}$$

In the Equations 3.4 and 3.5, ϕ_k and λ_k are respectively the latitude and longitude of body P_i with respect to body P_0. Furthermore, P_n is the n^{th}-degree Legendre polynomial which is given in Equation

3.6. R_0 is the equatorial radius of body P_0 and r_i is the distance between bodies P_0 and P_i. Equation 3.3 can be represented in multiple ways, for example by combining both terms or even including the ponctual interactions. However, the current representation is used to make a clear distinction between zonal harmonics which are only a function of the latitude ϕ_k on one side, and the sectorial and tesseral harmonics which are dependent on both the longitude and latitude on the other side.

$$P_n(x) = \frac{1}{2^n n!}\frac{d^n}{dx^n}(x^2-1)^2 \tag{3.6}$$

Note that the gradient of the potential of the extended body $\nabla_k U_{\bar{k}\hat{l}}$ is given in Cartesian coordinates centred on body P_l. To acquire an explicit formulation of Equation 3.3, the gradient of the spherical harmonic potential must be written relative to the Cartesian coordinates (x_k, y_k, z_k) with fixed axes with respect to Jupiter (P_0, x, y, z) (Lainey, Duriez and Vienne 2004). Therefore, the rotational state of the moons with respect to an inertial reference frame is required, which is usually given by the Euler angles (Ψ, I, ξ), which respectively represent precession, obliquity, and rotation of satellite P_k under consideration. These Euler angles relate to both the longitude λ_k and the latitude ϕ_k. The aforementioned Euler angles can be acquired by substituting $\psi = \alpha_0 + 90°$, $I = 90° - \delta_0$, and $\chi = W + W_0$ (Lainey, Duriez and Vienne 2004). Where α_0, δ_0 and W are given by Archinal et al. (2011) as a function of the current Julian day for both Jupiter and the Galilean moons. Furthermore, W_0 denotes the longitude of the central meridian which is defined with respect to specific surface features for all the Galilean moons.

3.1.4. Relativistic Correction

Whereas the contribution of relativistic effects is usually small (e.g. Dirkx et al. 2016; Lainey, Duriez and Vienne 2004) and can often be neglected, a rigorous model of the motion of the Galilean satellites should include terms that account for the theory of general relativity. According to Dirkx et al. (2016) adding relativistic corrections does not necessarily add additional parameters to the problem. Vice versa, there is no risk that the observability of the physical parameters influences the relativistic correction. Three types of relativistic corrections are described by the International Earth Rotation and Reference Systems Service (IERS) (Petit and Luzum 2010), which are (in order of decreasing effect with respect to the main Newtonian acceleration) the Schwarzschild terms, the effects of the Lense-Thirring precession and the geodesic (de Sitter) precession. For satellite orbiting the Earth, the Lense-Thirring and de Sitter terms are multiple orders of magnitude smaller with respect to the Schwartzschild term (Petit and Luzum 2010). Therefore, and to be compliant with Lainey, Duriez and Vienne (2004) only the Schwarzschild term is considered in this thesis.

The formulation of the Schwartzschild relativistic correction can be acquired by defining the N-body problem as discussed in Section 3.1.2 using a relativistic formulation. According to Lainey, Duriez and Vienne (2004) the relativistic effects induced by the masses of the Sun and the satellites can be neglected, leaving only the terms dependent on the mass of Jupiter. Subsequently, to account for the relativistic effects in a Jovicentric reference frame Equation 3.7 (Montenbruck and Gill 2012) should be added to the total equation of motion for body P_i.

$$\ddot{\vec{r}}_i = -\frac{Gm_0}{r_i^2}\left(\left(4\frac{Gm_0}{c^2 r_i} - \frac{\dot{r}_i}{c^2}\right)\vec{n}_i + 4\frac{\dot{r}_i^2}{c^2}(\vec{n}_i \cdot \dot{\vec{n}}_i)\dot{\vec{n}}_i\right) \tag{3.7}$$

In this equation, c is the speed of light and $\vec{n}_i$ and $\dot{\vec{n}}_i$ denote respectively the unit vectors of the position and velocity of a satellite i with respect to Jupiter.

Note that Lainey, Duriez and Vienne (2004) showed that not including the relativistic effects as resulted in a position error of 2 km over a period of 100 years. Despite its rather small effect, this acceleration is included for completeness. Nevertheless, due to time constrains the dynamical model still has a substantial difference with respect to the L2 ephemerides (Lainey et al. 2009) (see Chapter 7). Furthermore, during the mission duration of JUICE, no substantial signature is expected to build up. Therefore, the inclusion of the relativistic acceleration has no added value in this study. However, the inclusion of the relativistic acceleration is necessary especially in case the JUICE radiometric tracking data is combined with Earth-based astrometry to estimate the parameter (k_2/Q) over timescales longer

than 100 years. This prevents, the signature of the relativistic accelerations to spill into other parameters as its signature builds up over a period of more than 100 years.

3.1.5. Tidal Accelerations

There exist various methods to model tidal dissipation within a planet-moon system. Tidal dissipation is included in the dynamics for two reasons. Firstly, the tidal interaction between Jupiter and the Galilean moons has shown to have a crucial influence on their long-term dynamics which is manifested in secular changes in the semi-major axis, eccentricity and inclination of the moons as well as difference in the rotation of Jupiter as discussed in Section 2.5 (e.g. Dirkx et al. 2017; Yoder 1979). Secondly, by relating observations to the dynamical model including tidal dissipation, important information regarding the interiors of the moons can be retrieved.

The fundamental knowledge of modeling body tides was governed by Darwin (1880) and generalized by Kaula (1964). In this method the gravitational potential of the deformed body is decomposed into multipoles [1] and expanded into orbital elements using Love numbers as discussed in Section 2.5. In their study to the sensitivity of, among others, the tidal characteristics on the dynamics of the system, Dirkx et al. (2016) have used the aforementioned potentials to computed the tidal correction values $\Delta(c,s)_{np}^{(i,j)}(t)$ (representing a tide raised by body j acting on body i changing the spherical harmonic coefficient of order n and degree p). These corrections are returned into Equation 3.4 and 3.5 (substituted for c_{np} and s_{np}) to indirectly account for the tidal potential. This method, however, has proven to be rather complicated and sensitive to scaling.[2] Furthermore, according to Ferraz-Mello et al. (2008) care must be taken as some coefficients are not unambiguously defined and the need for successive summations makes the implementation of this method rather complicated.

Another, more promising method is developed by Boué et al. (2016). In this method the rotation, position and the accompanying deformation are all included in a single state vector and are integrated simultaneously assuming a viscoelastic body of Maxwell material. The implementation of such a model, however, will significantly increase both the model complexity and computational effort.

Finally, the constant time lag model is preferred as the expression for the tidal force is both very compact and physically intuitive. The constant time lag model uses a fictitious satellite to illustrate the time lag between the tide raising potential and the deformation of the body. To this end, a dynamical tide is modeled by a static tide by shifting back the time varying parameters (i.e. the moons is rotated back by $\vec{v}\Delta t$ and the attitude of the planet by $\vec{\omega}_p \Delta t$) (Efroimsky and Lainey 2007). This principle is visualized in Figure 3.1. The time lag Δt is a function of the tidal frequency and Q (note that Q is assumed to be constant) such that Δt is not a constant and varies with the tidal frequency T (see Equation 3.9). As Q is constant, this implies that ϵ in Figure 2.6 is constant as well (note that $2\epsilon = Q^{-1}$).

The tidal force as experienced on Jupiter induced by the moon is given in Equation 3.8 (Efroimsky and Lainey 2007). Note that in this equation the resulting potential as a consequence of the tidal distortion of the satellite by the planet is not considered. Furthermore, only the leading term is retained (dependent on the second degree Love number), higher order terms dependent on k_3 and higher are neglected by Efroimsky and Lainey (2007) even though they might be relevant. Finally, the higher order terms ($\mathcal{O}(\vec{f}^2/r^2)$) are neglected.

$$\vec{F}_{i\hat{0}} = -\frac{3k_2 G m_i^2 R_0^5}{r_i^8}\left(\vec{r}_i + \Delta t\left[\frac{2\vec{r}_i(\vec{r}_i\cdot\vec{v}_i)}{r_i^2} + (\vec{r}_i\times\vec{\Omega}_p + \vec{v}_i)\right]\right) \tag{3.8}$$

In this equation Δt is given by Equation 3.9 (e.g. Lainey et al. 2007; Lari 2018).

$$\Delta t = \frac{T\arcsin(1/Q)}{2\pi} \tag{3.9}$$

Where T, the period of the tidal cycle, is given below for the tidal dissipation within Jupiter (Lainey et al. 2009, Supplementary Information).

[1] A mathematical series which represents a function usually depending on the two angle on a sphere.
[2] Dr. D. Dirkx - Personal Communication.

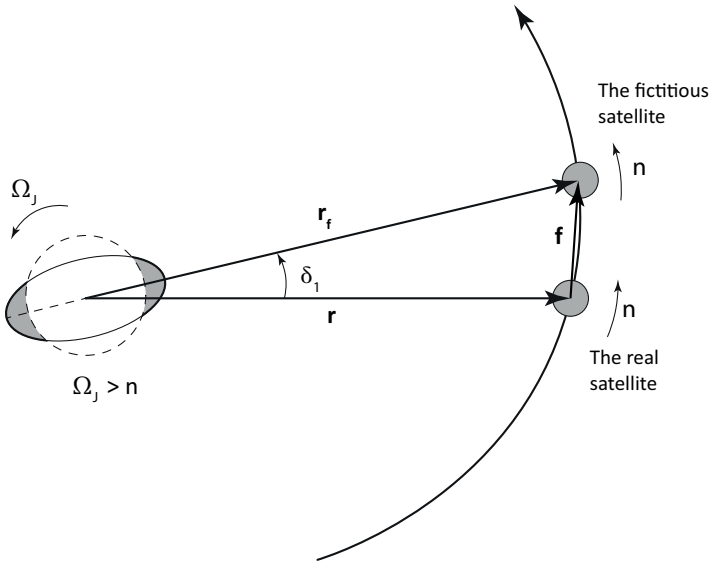

Figure 3.1: A planet together with a tide raising moon to visualize the tidal lag model.

$$T = \frac{2\pi}{2(|\vec{\Omega}_P - n_i|)} \tag{3.10}$$

For the satellites, the period of main tidal excitation is equal to $T = 2\pi/n_i \approx 2\pi/\vec{\Omega}_i$ (Lainey et al. 2009, supplementary information). For $\vec{F}_{i\hat{0}}$, which is the tidal force encountered by satellite i, as a result of the tidal distortion that this satellite i causes on Jupiter (body P_0), the period of the tidal cycle can be easily computed considering a constant rotation rate of Jupiter $\vec{\Omega}_P$. However, considering $\vec{F}_{\hat{0}i}$, computing the period of tidal distortion T is complicated as the rotation rate of the satellite $\vec{\Omega}_i$ is not constant as the satellite librates. Furthermore, not the absolute rotation but the rotation with respect to Jupiter is relevant. Lari (2018) has proposed a solution to mitigate this problem. First, the radial dissipation due to the tides needs to be evaluated considering $\vec{\Omega}_i = \vec{r}_i \times \vec{v}_i / r_i^2$. Only taking into account the secular effects (terms containing the tidal lag Δt) yields Equation 3.11 which represents the force experienced at Jupiter by the radial tide raised on satellite i.

$$\vec{F}_{\hat{0}i} = -3\frac{(k_2)_i G m_0^2 R_i^5}{r_0^8}\Delta t\left(3\frac{\vec{r}_0}{r_0}\frac{\vec{r}_0 \cdot \vec{v}_0}{r_0^2}\right) \tag{3.11}$$

As discussed in Section 2.5.2, the satellite tides are comprised of a radial and a librational tide. According to (Murray and Dermott 1999), the amplitude of a radial tide (as given in Equation 3.11) is $3/4$ of the amplitude of a librational tide. Thus by adding $4/3$ of the effect of the radial tide as given in Equation 3.11 to account for the effect of the librational tides yields Equation 3.12 which accounts for both radial and librational tides.

$$\vec{F}_{\hat{0}i} = -3\frac{(k_2)_i G m_0^2 R_i^5}{r_0^8}\Delta t\left(7\frac{\vec{r}_0}{r_0}\frac{\vec{r}_0 \cdot \vec{v}_0}{r_0^2}\right) \tag{3.12}$$

Note that Equation 3.12 should only be used to obtain the disturbing force experienced at Jupiter by the tidal bulge Jupiter has exerted on a satellite. For the opposing force (experienced at a satellite by the tidal bulge the satellite has exerted on Jupiter) Equation 3.8 should be used.

As previously discussed, the first right hand term in Equation 3.8 is only dependent on k_2 but not on Q. This term (in Equation 3.8) represents the perturbation in case no tidal dissipation is considered. Consequently, this term causes a perturbation to the orbital elements (especially the semi-major axis

and consequently the mean orbital motion) which is constant with time (Lainey et al. 2009, supplementary information). As a result, k_2 and Q are completely correlated and the determination of the individual variables is not possible. Therefore, in the estimation process, constant values of k_2 are usually assumed after which Q is fitted. Alternatively, as proposed by Efroimsky and Lainey (2007), the first term is usually neglected.

Computing the tidal accelerations requires, among others, the tidal Love number k_2, the tidal lag parameter Q as well as the rotational rate of Jupiter and the mean orbital motion of the Galilean satellites. The last two parameters are obtained by computing these parameters for the initial state using the physical parameters as discussed in both Section 3.2.1 and 3.2.2. Furthermore, the combination of both k_2 and Q for Jupiter and the Galilean moons is given in Table 3.1.

Table 3.1: The tidal Love number as well as the tidal Love number combined with the tidal lag parameter Q for both Jupiter and the Galilean moons. The combined parameter (k_2/Q) is given by Lainey et al. (2009). The tidal Love number k_2 for Jupiter is given by Lainey et al. (2009) and the tidal Love number for the Galilean moons is based on the assumption by Dirkx et al. (2016). Note that (k_2/Q) is determined using observations, where k_2 is inferred from models simulating the response of the material that comprises the planet or satellite.

	Jupiter	Galilean Moons
k_2 [-]	0.38	0.3
(k_2/Q) [-]	1.102×10^{-5}	0.015

Note that, altough the fraction (k_2/Q) is determined with reasonable accuracy by Lainey et al. (2009), the tidal Love numbers k_2 may be substantially different than their actual values as addressed by Dirkx et al. (2016). However, as their effect is small (approximately 1 km for the tidal dissipation of Io over a period of 5 years Dirkx et al. (2016)) and scales linearly with the corresponding value (see Equation 3.8) the result on the propagated dynamics is expected to be limited.

3.1.6. Complete Equation of Motion

As all individual terms of the equation of motion were given in the preceding sections, the complete equation of motion can thus be given by Equation 3.13.

$$\begin{aligned}\ddot{\vec{r}}_i = &-\frac{G(m_0+m_i)\vec{r}_i}{r_i^3} + \sum_{j=1,j\neq i}^{N} Gm_j\left(\frac{\vec{r}_j-\vec{r}_i}{r_{ij}^3} - \frac{\vec{r}_j}{r_j^3}\right) + G(m_0+m_i)\left(\nabla_i U_{\hat{i}\hat{0}} - \nabla_0 U_{\hat{0}\hat{i}}\right)\\ &+ \sum_{j=1,j\neq i}^{N} Gm_j\left(\nabla_j U_{\hat{j}\hat{0}} - \nabla_0 U_{\hat{0}\hat{j}} + \nabla_i U_{\hat{i}\hat{j}} - \nabla_j U_{\hat{j}\hat{i}}\right)\\ &+ \frac{(m_0+m_i)}{m_i m_0}\left(\vec{F}_{\hat{i}\hat{0}}^T - \vec{F}_{\hat{0}\hat{i}}^T\right) - \frac{1}{m_0}\sum_{j=1,j\neq i}^{N}\left(\vec{F}_{\hat{j}\hat{0}}^T - \vec{F}_{\hat{0}\hat{j}}^T\right)\\ &- \frac{Gm_0}{r_i^2}\left(\left(4\frac{Gm_0}{c^2 r_i} - \frac{\dot{r}_i}{c^2}\right)\vec{n}_i + 4\frac{\dot{r}_i^2}{c^2}(\vec{n}_i\cdot\dot{\vec{n}}_i)\dot{\vec{n}}_i\right)\end{aligned} \tag{3.13}$$

Note that the last term (on the last line) in this equation is subject to the assumptions made for the relativistic correction as discussed in Section 3.1.4. Furthermore, note that the figure-figure interactions (denoted by the subscript with two hat symbols) as discussed in Section 3.1.3 are neglected. Finally, depending on which tidal interaction is considered, different assumptions as listed in Section 3.1.5 are applicable.

For the propagation of the Galilean moons, the mutual spherical harmonic and tidal accelerations between Jupiter and the Galilean moons are modeled, keeping the state of Jupiter fixed with respect to the reference ephemerides. Furthermore, point mass third body perturbations are computed for the minor moons Amalthea, Thebe, and Himalia as well as for Saturn and the Sun.

3.2. Gravitational, Rotational and Tidal Models

The implementation of the equation of motion as given in Section 3.1.6 requires various physical constants which describe the gravitational and rotational models. These constants and their respective origin are discussed in Section 3.2.1 and 3.2.2.

3.2.1. Gravitational Models

Currently, the most accurate gravitational models of the Galilean moons are based on the flybys of the Galileo spacecraft during the years 1995 to 2003.[3] The used radius, gravitational parameter and the quadruple coefficients J_2 and C_{22} are given in Table 3.2 for the Galilean moons. Furthermore, the gravitational parameter is included for the three largest minor moons (moons that do not belong to the Galilean moons) Amalthea, Thebe, and Himalia as well as for the Sun and Saturn.

Table 3.2: Parameters representing the gravitational models for the Galilean and the three largest minor satellites. Parameters regarding the Galilean moons are from Schubert et al. (2004) except the radius of Europa. GM from Thebe and Himalia are from Dirkx et al. (2017) and GM from Amalthea, the Sun, and Saturn are from the DE431 ephemerides (Folkner et al. 2014).

	$R\ [km]$	$GM\ [km^3s^{-2}]$	$J_2\ [10^{-6}]$	$C_{22}\ [10^{-6}]$
Galilean Moons				
Io	1821.6 ± 0.5	5959.91	1859.5	558.8
Europa	1565.0 ± 0.5 [4]	3202.72	435.5	131.5
Ganymede	2631.2 ± 1.7	9887.83	127.53	38.26
Callisto	2410.3 ± 1.5	7179.29	32.7	10.2
Minor Moons				
Amalthea	n/a	0.138	n/a	n/a
Thebe	n/a	0.027	n/a	n/a
Himalia	n/a	0.280	n/a	n/a
Other				
Sun	n/a	132712440041.9	n/a	n/a
Saturn	n/a	37940585.20	n/a	n/a

Note that the coefficients (J_2 and C_{22}) given in Table 3.2 are the unnormalized. However, as they usually cover a range of multiple orders of magnitude, the coefficients are usually geodesy normalized (Montenbruck and Gill 2012). The normalization method as well as the resulting acceleration as a function of the normalized coefficients is shown in Appendix A.1. From Table 3.2, the influence of the tides in the Jovian system becomes immediately apparent. As can be seen both the rotational deformation (represented by J_2) as well as the tidal deformation (represented by C_{22}) are significantly higher for Io compared to Callisto. This difference between Io and Callisto is expected as the rotational deformation is larger for Io as a consequence of the higher orbital motions and thus rotation rate (as the Galilean satellites are tidally locked). Furthermore, the gravity potential of Jupiter at the location of Io is higher, such that the differential gravity field over Io gives rise to a higher tidal amplitude.

The constants defining the gravity field of Jupiter are given in Table 3.3. Note that this model provides the geo-potential coefficients up to degree 6 and order 2 (only for degree 2) and is, similar to the models for the Galilean moons, primarily based on data from the Galileo mission. A new more extensive model (up to degree 12 and up to order 2 for degree 2) is provided by Iess et al. (2018) using data provided by the Juno spacecraft. However, as both the JUICE CReMA 3.2 trajectory and the L2 ephemerides of the Galilean moons as provided by Lainey et al. (2009) use the gravity model as given by Jacobson (2001), the latter model is used for the propagation of the Galilean satellites in this study. For the propagation of the Galilean moons, the position of the Sun, Jupiter, Saturn, and the minor Jovian moons as well as the initial position of the Galilean moons are given by the SPICE (Space Planet

[3] NASA Science 'Timeline | Galileo - Solar System Exploration: NASA Science' solarsystem.nasa.gov `https://solarsystem.nasa.gov/missions/galileo/timeline/#launch` (accessed October 8, 2018)

[4] NASA Solar System Dynamics 'Planetary Satellite Physical Parameters' ssd.jpl.nasa.gov `https://ssd.jpl.nasa.gov/?sat_phys_par#ref10` (accessed October 5, 2018) - Internal reference: Thomas, P.C. 2002. private communication on limb fit results

Table 3.3: Parameters representing the gravitational model of Jupiter. All parameters except the GM are from Jacobson (2001). The GM is given by Folkner et al. (2017).

$R\ [km]$	$GM\ [km^3s^{-2}]$	$J_2\ [10^{-6}]$	$C_{22}\ [10^{-6}]$	$J_3\ [10^{-6}]$	$J_4\ [10^{-6}]$	$J_6\ [10^{-6}]$	$S_{22}\ [10^{-6}]$
71492	126686533	14735	-0.03	0.2	-588.8	27.8	-0.04

Instrument C-matrix Events) kernels. The specific kernels used for this simulation a given in Appendix A.2. Furthermore, the position of the Earth is also included to be able to generate the observations as will be further discussed in Chapter 4.

3.2.2. Rotational Models

As shown in Section 3.1.3, to compute the accelerations imposed by an extended body on a second body, both the longitude and latitude of the second body with respect to the first body are required. Therefore the rotational state of both Jupiter and the Galilean moons is required. To this end, the right ascension and declination (α_0 and δ_0) of the pole as well as the rotational angle W with respect to the prime meridian are given by Archinal et al. (2011) using analytic functions. Note that these angles appear in the Euler angles as discussed in Section 3.1.3. Furthermore, the analytic functions also include terms to account for the effects related to both precession and nutation. The rotation models as presented by Archinal et al. (2011) are included in the `pck00010.tpc` kernel as presented in Section A.2.

Note that the aforementioned rotation model does not include librations. A study on the sensitivity of including the once-per-orbit libration, as discussed in Section 2.5, was performed by Dirkx et al. (2016). It was found that the influence of including this once-per-orbit libration is most likely below the observable level for all the moons. Furthermore, Dirkx et al. (2016) state that by modeling the once-per-orbit libration, only information on the angle ψ_j can be unveiled while, among others, the thickness of the ice layer (as discussed in Section 2.6.1) is constrained by the libration amplitude γ_j for which $\gamma_j << \psi_j$. Nevertheless, Dirkx et al. (2016) conclude that the once-per-orbit libration should be included to avoid the signature of the libration to spill into for example the tidal Love numbers. However, this study aims to reduce the condition number by optimizing the observation schedule of the JANUS camera considering only initial states of the moons. Therefore, the once-per-orbit libration is not considered.

3.3. Numerical Propagation and Integration

In this section the most important aspects regarding the numerical propagation and integration will be discussed. First of all, the different types of time are discussed in Section 3.3.1. Furthermore, the required reference frames will be discussed in Section 3.3.2 after which the used propagator and integrator and their respective settings will be discussed in Section 3.3.3.

3.3.1. Time

Throughout the framework of this study different time types are used. To avoid confusion, all types that used are discussed in this section.

The numerical propagation is performed using Barycentric Dynamical Time (TDB). The unit of TDB is the SI (Système International) second as measured on the geoid (shape of the Earth considering only the self Gravitation and rotation). Note that TDB differs from Terrestrial Time (TT) by less than 0.002 seconds and can be used interchangeably with only negligible errors (Kaplan 2011). Note that TDB is zero at J2000. TT has its origin in the Ephemeris Time (ET) and TT is approximately equal to ET ($TT \approx ET$). ET is also the time used by the JPL SPICE toolkit[5] to retrieve the position of the planetary bodies.

TT and ET are related to Coordinated Universal Time (UTC) by the International Atomic Time (TAI). As UTC is the common civil time (e.g. Montenbruck and Gill 2012) and the time used by ESA to for example indicate the time of the flybys and other manoeuvres, it is used throughout this thesis in most of the time dependent figures. ET is related to TAI by Equation 3.14 (Montenbruck and Gill 2012).

[5]The Navigation and Ancillary Information Facility "SPICE Toolkit" naif.jlp.nasa.gov `https://naif.jpl.nasa.gov/naif/toolkit.html` (accessed September 18, 2018)

$$TT \approx ET = TAI + 32.184\,\text{s} \tag{3.14}$$

Subsequently, TAI differs from UTC by a integer number of leap seconds. Currently the number of leap seconds equals 37 [6]. Thus UTC can be related to TAI using Equation 3.15. In this equation N_{leap} is the number of leap seconds.

$$TAI = UTC + N_{leap} \tag{3.15}$$

The UTC time in seconds can be converted to a calendar date using the Modified Julian Date (MJD). MJD is related to the UTC_{J2000} by Equation 3.16.

$$MJD = \frac{UTC_{J2000}}{84600} + 51544.5 \tag{3.16}$$

The MJD can be converted to a calendrical date. The interested reader can find the necessary equations in Montenbruck and Gill (2012).

3.3.2. Reference Frames

To be able to propagate the Galilean satellites a careful definition of the used reference frames is required. This section discusses the inertial reference frame ,the local vertical local horizontal reference frame and the galactic reference frame.

Inertial Reference Frame

The Galilean moons will be propagated with respect to the center of Jupiter in a reference frame which has its orientation fixed to the Earth mean equator and equinox of J2000 (i.e. a quasi inertial or Newtonian reference system). This means that this reference system is free to move with respect to the Earth but does not rotate.

Local Vertical Local Horizontal Reference Frame

Whereas the ICRF is necessary for propagation of the solar system bodies it does not yield good insight into the motion of such bodies. Therefore a local vertical local horizontal (LVLH) reference frame can be adopted (Schäff and Wiegand 2015). Such a frame rotates with respect to an inertial frame and has its origin at the center of mass of the body of interest (for example one of the Galilean moons). Its x-axis is aligned with the radial orbit component (which is aligned with the position vector). Its y-axis is aligned with the velocity vector and indicates the along-track orbital component. Finally the z-axis is perpendicular to the orbital plane and denotes the cross-track orbital component. A position vector in the LVLH frame $\mathbf{r}_{LVLH}$ can be related to a position in an inertial reference frame $\mathbf{r}_i$ by Equation 3.17 (Schäff and Wiegand 2015).

$$\mathbf{r}_i = \left[\frac{\mathbf{r}_i}{||\mathbf{r}_i||} \quad \frac{(\mathbf{r}_i \times \mathbf{v}_i) \times \mathbf{r}_i}{||(\mathbf{r}_i \times \mathbf{v}_i) \times \mathbf{r}_i||} \quad \frac{\mathbf{r}_i \times \mathbf{v}_i}{||\mathbf{r}_i \times \mathbf{v}_i||}\right] \mathbf{r}_{LVLH} \tag{3.17}$$

In this Equation the position and velocity vectors are returned as row vector and are represented in an inertial reference frame with its axes aligned with the ICRF J2000. This transformation can subsequently be used to express (propagation) errors in terms of the orbital components. The latter enables more straightforward analysis of the resulting errors.

Galactic Coordinate System

The Galactic reference frame is a useful reference frame in the field of astronomy. As the optical astrometry using the JANUS camera requires background stars for calibration of the images (as discussed in Chapter 5), the Galactic reference frame is necessary to express the direction of the optical

[6] Current International Atomic Time, Time Standard (TAI) "Current International Atomic Time - TAI" timeanddate.com `https://www.timeanddate.com/worldclock/other/tai` (accessed September 18, 2018)

axis of the camera within the Milky Way. Note that with zero Galactic longitude and latitude the optical axis is pointing in the direction of Galactic center (which is located at the center of the Milky Way). Furthermore, a Galactic latitude of zero means the optical axis of a camera is pointing within the plane of the Milky Way. The necessary equations to transfer the equatorial right ascension and declination to the Galactic longitude and latitude are given in Appendix A.3.

3.3.3. Propagators and Integrators

There are different propagators (method to represent the dynamical state of a body) and integrators (numerical methods to integrate the dynamics of natural or artificial body) available for numerical integration of dynamical systems. An often used propagator is the Cowell propagator, which means the Cartesian position and velocity of the bodies under consideration are directly integrated (Wakker 2015). A large advantage of using such a propagation method is that it can be applied for any type of acceleration. However, the Cowell propagator does not differentiate between central body and perturbing accelerations. Therefore, usually small integration steps are required which imply a relatively large numerical error as well as substantial computation times (Wakker 2015). This problem can be alleviated by using for example, the method of Encke or the method of variation of the orbital elements. The latter can be applied using either Kepler elements or modified equinoctial elements. Contrary to the Cowell method, the Encke method makes use of a reference orbit such that only the perturbing accelerations are numerically integrated. As a result, the integration step can be larger compared to the Cowell method leading to a lower computation time. Finally, the method of variation of the orbital elements considers the perturbed orbit a a continuous sequence of Keplerian orbit.

The aforementioned numerical errors are especially important for a spacecraft that orbits close to the Earth or has a highly elliptical orbit. In this type of orbits, the perturbing accelerations (especially their direction) change relatively fast which is related to the short orbital period. However, the Galilean satellites are close to circular and have orbital periods on the order of days. Therefore, the propagation step can be relatively large for a reasonable accurate integrator (i.e. no Euler integration), even for a Cowell propagator, without the risk of large numerical errors. Therefore, as the implementation of the Cowell propagator is most straightforward for the acceleration models described in this chapter, this propagator is used for the numerical integration of the states of the Galilean satellites.

Next to propagators various types of integrators are available. These can be classified under Runge-Kutta methods, multi-step method, and extrapolation methods. A rigorous comparison between different types of integrators of the different types given by Montenbruck and Gill (2012) for both circular and highly eccentric orbits. In this comparison it was concluded that the DOPRI8 (RK8(7)13M), which was developed by Prince and Dormand (1981), was most efficient for acceleration models which involve velocity dependent terms. The RK8(7)13M is a 13-stage (which means that per integration step 13 function evaluations are required) Runge-Kutta method for an 8th-order approximation. The standard equation for a s-stage Runge-Kutta method is given in Equation 3.18. For a low eccentricity (for the Galilean moons e < 0.1), the difference between the considered types of integrators was relatively small. Note that this comparison was performed for the outer five planets in the Solar system (Hull et al. 1972). Therefore, this comparison is relatively well applicable to the propagation of the Galilean satellites (compared to the propagation of artificial spacecraft).

$$\boldsymbol{y}(t_0 + h) \approx \boldsymbol{y}_0 + h \cdot \boldsymbol{\Phi} = \boldsymbol{\eta}(t_0 + h) \tag{3.18}$$
$$\boldsymbol{\Phi} = \sum_{i=1}^{s} b_i \boldsymbol{k}_i$$

In which the vector $\boldsymbol{k}_i$ is defined by Equation 3.19.

$$\boldsymbol{k}_1 = \boldsymbol{f}(t_0 + c_1 h, \boldsymbol{y}_0) \tag{3.19}$$
$$\boldsymbol{k}_i = \boldsymbol{f}(t_0 + c_i h, \boldsymbol{y}_0) + h \sum_{j=1}^{i-1} a_{ij} \boldsymbol{k}_j \ (i = 2, \dots, s)$$

In these equations the coefficients a_{ij}, b_i, and c_i are defined for a specific Runge-Kutta method. The coefficients for the DOPRI8 integrator are given by Prince and Dormand (1981). Note that this discussion on the different types of integrators is not rigorous and more efficient (with respect to the required computation time) integrators are available such as the DE multi-step method and the FILG11 algorithms. However, Montenbruck and Gill (2012) show that for close to circular orbits the difference between the aforementioned methods is limited and becomes more pronounced for highly eccentric orbits.

For the study under consideration, however, two important factors need to be considered. First of all, a fixed time-step was used as this substantially simplifies the analysis of the propagated results. Moreover, as shown in Table 2.1, the orbits of the Galilean moons are close to circular, thereby reducing the impact of a variable time-step integrator. Both considerations advocate the use of the DOPRI8 integrator as its performance is sufficiently accurate for the intended purpose. The integration time-step is established at 1 hour. The performance of both the integrator and the integration step will be further assessed in Chapter 7.

4

Tracking Types

Estimating the ephemerides of the Galilean moons requires various tracking techniques. This chapter discusses the tracking types which are available within the context of JUICE. First of all, Section 4.1 gives the available tracking types and shows the observational geometry as relevant for the within this thesis. Secondly, Section 4.2 discusses how the orbit determination of JUICE is related to the generation of the Jovian system ephemerides. Thereafter, both the radiometric and space-based optical tracking techniques as listed in Section 4.1 are discussed in detail in respectively Section 4.3 and 4.4. Furthermore, Section 4.5 discusses how the different tracking techniques contribute to the generated system ephemerides. The tracking uncertainties and their origin and enhancements relevant within the JUICE mission are discussed in Section 4.6 after which Section 4.7 considers the operational constraints applicable to the various tracking types.

4.1. Available Observation Types

Dirkx et al. (2017) presents a list of five observation types which are available for tracking within the JUICE mission. This list is presented below. The specific geometry of the observations as related to the Jupiter-satellite-spacecraft geometry is visualized in Figure 4.1.

- The spacecraft range $|\vec{r}_{sc}|(= r_{sc})$ which is obtained by the 3GM instrument, indicating the distance between Earth-based tracking stations and the spacecraft. This data is only available during flybys or orbit phases around a satellite.
- Doppler range rate $|\dot{\vec{r}}_{sc}|(= \dot{r}_{sc})$ obtained primarily by the *3*GM instrument and supplemented by PRIDE data. As with the satellite range, only available during when the spacecraft is performing flybys or orbit phases around a satellite.
- Lateral positions (from VLBI data), observed from Earth, returning the declination δ_{sc} and right ascension α_{sc} of the center of the spacecraft (during flybys or orbits but at a more limited cadence than range or Doppler data due to need of a large number of resources).
- Optical (space-based) astrometry of the Galilean satellites from the JANUS instrument or navigation camera (NavCam) returning the spacecraft based declination and right ascension, respectively δ_i^{sc} and α_i^{sc}, of a Galilean satellite i.
- Optical (Earth-based) astrometry of the Galilean satellites from different Earth observatories returning the declination and right ascension of a Galilean satellite i (respectively δ_i and α_i).

In Figure 4.1, subscripts J, i and sc denote respectively Jupiter, the Galilean satellites i (Io = 1, Europa = 2, Ganymede = 3, and Callisto = 4 as discussed in Section 3.1.1), and the JUICE spacecraft. A superscript denotes the origin of the reference frame. Thus a subscript sc denotes that the measurement is relative to the center of the spacecraft. The five observation types can be divided amongst radiometric (The first three observation types aforementioned list) or optical tracking techniques (the

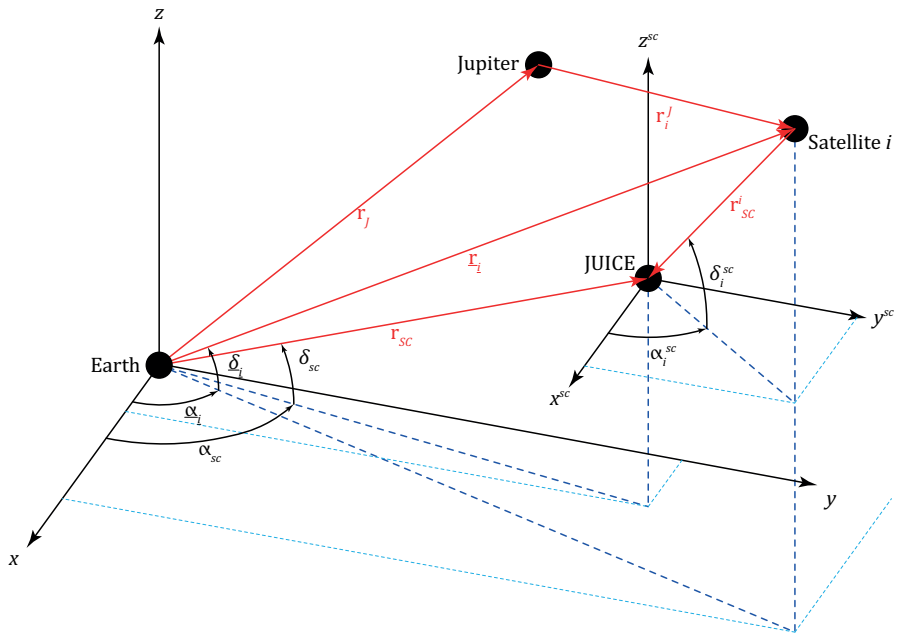

Figure 4.1: Relation of the observables available within the PRIDE experiment with the Jupiter-satellite-spacecraft geometry (based on Figure 2 of Dirkx et al. (2017)).

last two observation types in the aforementioned list). Both tracking techniques will be discussed in more detail in Section 4.3 and Section 4.4 respectively.

Note that in this study, Earth-based optical astrometry is not considered. This is justified by the observational uncertainty which is substantially lower compared to the radiometric tracking observables and space-based optical astrometry. According to Arlot et al. (2012) Earth-based astrometric observations are required over a time-span larger than 30 years for mutual event astrometry (in which the relative angular position between two satellites is measured) and larger than 50 years for direct optical astrometry to detect the effects associated to the tides in the Jovian system. Thus, as stressed by Dirkx et al. (2017), Earth-based astrometry might be especially important in providing a long-period set of observations, outside the interval in which JUICE is orbiting the Jovian system. However, within the duration of the JUICE mission, Earth-based astrometry has limited capability to reduce the instability of the normal equations. This is related to the low weight with which the astrometric observations are associated due to their large observational uncertainty (see Chapter 5 for a discussion on the relationship between the observational uncertainty and the weights). Furthermore, Earth-based astrometry can also be used to fill the gaps in between the Galileo orbiter, the JUICE spacecraft, and the Europa Clipper. In this way, the long-term astrometric data-set together with the high accuracy spacecraft tracking data will enable to constrain the signature of the tides.

4.2. Decoupling JUICE Orbit Determination

The purpose of the PRIDE experiment is to estimate the ephemerides of the Galilean moons with an improved accuracy. This is accomplished by means of a least-squares estimation (see Chapter 5) using the available observations. In the ideal situation, the dynamics of the spacecraft and the moons would be estimated concurrently over one arc. However, Dirkx et al. (2017) give two reasons to stress that such an approach is not desirable for an optimization study which uses a covariance analysis. First of all, concurrently estimating the dynamics of the spacecraft and the moons requires a constrained multi-arc solution as proposed by Alessi et al. (2012). Such a multi-arc approach is required as estimating the spacecraft dynamics in one arc is practically and fundamentally unfeasible (Dirkx et al. 2017). Practically, as the uncertainties in the dynamical modeling of the spacecraft over long times scales make the matrix inversion in the parameter estimation framework of the ephemerides impossible. This is a result of the limited accuracy with which the dynamics of the spacecraft can be modeled over longer time-scales. Fundamentally, as the motion of the spacecraft during its Jovian tour is chaotic

to such an extent that the ephemerides of the Galilean moons are ‘unobservable’, referring to the terminology which will be introduced in Chapter 5, such that inversion of the least-squares problem is not possible (e.g. Dirkx et al. 2017). Ephemerides are unobservable if their dynamics are not (accurately) constrained in the observations.

A constrained multi-arc solution copes with this problem by coupling the different arcs using boundary conditions as well as coupling the multiple arcs to the spacecraft under consideration (e.g. Alessi et al. 2012). However, implementation of such a multi-arc solution will significantly increase the computation time which is undesirable for an optimization study. Secondly, combining the determination of the dynamics of the spacecraft and the moons will complicate the analysis of the resulting covariance matrix. According to Dirkx et al. (2017), this is because the true-to-formal-error ratio[1] for spacecraft orbit determination is generally more optimistic than for the determination of planetary or satellite ephemerides.

For the previously mentioned reasons, the orbit determination is decoupled from the estimation of the ephemerides similar to the approach used by Dirkx et al. (2017). Therefore, the influence of the spacecraft orbit determination is included in a parametric fashion as will be discussed in more detail in Chapter 5. This also means that, referring to Figure 4.1, the observations r_{sc} as well as α_{sc} and δ_{sc} are replaced by respectively r_i, α_i, and δ_i. Note that observations with a subscript i denote synthetic observations while the observations with a subscript sc denote real observations. To account for the uncertainty in orbit determination of the spacecraft, the estimated uncertainty of the real observations is added to the observational uncertainty of the synthetic observations (for more details refer to Chapter 5). Moreover, the tracking stations are modeled to be in the center of the Earth. This assumption simplifies the generation of the tracking observations and and has insignificant influence as the distance between the surface of the Earth and its center is negligible with respect to the distance between the Earth and Jupiter.

4.3. Radiometric Tracking

Most planetary spacecraft are being tracked by either NASA’s Deep Space Network (DSN) or ESA’s tracking station network (Estrack) (e.g. Bocanegra-Bahamón et al. 2018). This tracking provides observations from which the precise state vector of the spacecraft can be determined. Tracking systems usually the Range, Doppler, and VLBI tracking types. First of all, the different types of spacecraft tracking will be discussed in Section 4.3.1. Thereafter, the aforementioned tracking types will be discussed in respectively Section 4.3.2, 4.3.3, and 4.3.4.

4.3.1. Types of Spacecraft Tracking

Radiometric tracking observations (ranging, Doppler tracking and VLBI (Very Long Baseline Interferometry) can be obtained either using one-way, two-way or three-way tracking. For one-way tracking a down- or up-link signal generated by the spacecraft is used to acquire the range or Doppler measurement. This method, however, introduces a large error in the observations as different clocks with different frequency standards are used and should be compared (e.g. Dirkx 2015; Thornton and Border 2003). Note that, for example, in GNSS observation the clock errors represent a dominant error source, which can , however, for GNSS receivers be corrected as generally a large number of range observations from different satellites is available. To avoid this problem for interplanetary tracking, radiometric tracking is usually performed in a two-way mode as the transmitting and receiving station are similar, removing the aforementioned error source (e.g. Dirkx 2015; Thornton and Border 2003). During a two-way measurement, the spacecraft receives the up-link signal as sent the ground station after which the signal is amplified, scaled and re-transmitted to the ground station.

Three-way tracking is only used for spacecraft in the outer Solar system. This is necessary as the very long light times between the ground station and the spacecraft combined with the rotation of the Earth make to-way tracking geometrically impossible (e.g. Thornton and Border 2003). However, as Jupiter is sufficiency close to the Earth, two-way tracking can be employed in the context of the JUICE-mission (JUICE Science Study Team 2014).

[1] The true error refers to the actual error between the computed and measured observations where the formal error refers to the error retrieved from a covariance analysis as will be discussed in Chapter 5.

4.3.2. Spacecraft Ranging

The spacecraft range, or distance from the spacecraft to a tracking station on Earth (or in the case of this study, the center of the Earth) as indicated in Figure 4.1, is usually obtained using the round-trip transfer time of a radiometric signal which is generated at a DSN or Estrack station (e.g. Thornton and Border 2003). Such a signal, which is a series of sinusoidal tones, is derived from a station frequency standard and consequently modulated using phase modulation on a carrier signal. The fundamentals of ranging as discussed by Thornton and Border (2003) are summarized below. First, the spacecraft receiver locks on the up-link carrier signal. As the spacecraft receiver is tracking the ranging signal, a reference signal which is consistent with the up-link carrier signal is produced by a phase-locked loop. Consequently, the ranging signal is demodulated from the carrier signal using the generated reference signal. The demodulated ranging signal, after it is passed through a low-pass filter, is modulated on a down-link carrier signal. This down-link signal is consistent with the up-link signal except for the fact that it is offset in frequency. A similar procedure is conducted on ground to demodulate the down-link signal. The received ranging signal is then compared with the transmitted ranging signal to acquire the round-trip transfer time.

Contrary to for example two-way Doppler observations, range observations are significantly effected by both random and systematic errors (Iess et al. 2014). Furthermore, the uncertainty is not completely white and uncorrelated (e.g. Dirkx et al. 2017). According to Dirkx et al. (2017), this should be considered in a covariance analysis to prevent too optimistic results. The latter may be included using consider parameters which estimate systematic errors. However, as this study focuses on the condition number rather than the formal errors, the systematic range errors are ignored. The current uncertainty in range measurements is on the meter level σ_{range} = 1-5 m. However, Iess et al. (2014) has proposed a number of improvements which will reduce the uncertainty of a range measurement to the centimeter level (σ_{range} = 20 cm), which is the uncertainty used by Dirkx et al. (2017) for a study on the relative contribution of the PRIDE experiment. An overview of the most important error sources and mitigation methods is provided in Section 4.6.

4.3.3. Spacecraft Doppler Tracking

As the ground station and the satellite are moving with respect to each other, the frequency of the received signal f_R is different compared to the frequency f_T of the transmitted signal. This difference is caused by the so called Doppler shift for which a rough approximation is given in Equation 4.1 (Thornton and Border 2003).

$$f_R = \left(1 - \frac{\dot{\rho}}{c}\right) f_t \tag{4.1}$$

As can be seen, the range rate $\dot{\rho}$ can be obtained by the Doppler measurement (Thornton and Border 2003) in which both f_T and f_R are available. The resulting Doppler range-rate measurement can be obtained either in closed-loop or open-loop (Bocanegra-Bahamón et al. 2018). Most often, in tracking of spacecraft for which the range-rate is required in real-time (for example to perform navigation measurements), the Doppler range-rate is acquired in closed loop.

For closed-loop Doppler tracking, as soon as the ground receiver is phase locked on the down-link signal as described in Section 4.3.2, the Doppler frequency or Doppler tone is extracted by comparing the difference between the down-link frequency and the up-link frequency (e.g. Bocanegra-Bahamón et al. 2018). Consequently, the resulting Doppler tone will be analyzed by a Doppler cycle counter which measures the total difference in phase of the Doppler tone over a predetermined count interval T_c. This counter interval is also referred as integration time and is usually around 60 s (e.g. Iess et al. 2014). However, both shorter and longer integration times are used (e.g. Dirkx et al. 2017). Finally, the total phase change obtained from the Doppler counter yields the change in range over the integration time.

A phase lock, as required for closed-loop Doppler tracking, is not always available. For example, during planetary atmospheric occultations, abrupt changes in the frequency and amplitude of the signal can result in the phase lock to be lost (Bocanegra-Bahamón et al. 2018). In such an event, open-loop Doppler tracking is necessary. The interested reader should refer to Bocanegra-Bahamón et al. (2018) for a fundamental description regarding open-loop Doppler tracking. A fundamental difference

between open- and close-loop Doppler tracking is that for open-loop Doppler tracking is performed in post-processing while closed-loop Doppler tracking is performed real-time.

The acquired slant range-rate $\dot{\rho}$ encodes both a slowly varying geocentric range-rate $\dot{r}$ as well as a rapid variation which is related to the rotation of the Earth (similar to range as discussed in Section 4.3.2) which is shown in Equation 4.2 (e.g. Thornton and Border 2003).

$$\dot{\rho}(t) = \dot{r}(t) + \underbrace{\omega_E r_s \cos\delta \sin\left(\omega_E t + \phi + \lambda_s - \alpha\right)}_{\text{Earth Rotation Related Term}} \tag{4.2}$$

In this equation $\dot{r}(t)$ is the geocentric range-rate, ω_E the rotation of the Earth. r_s and λ_s denote respectively the radius an latitude of the tracking station and α and δ represent respectively the right ascension and declination of the spacecraft. Furthermore t corresponds to Universal Time (UT) and ϕ is the instantaneous right ascension of the mean Sun (Thornton and Border 2003). In this equation the second term basically modulates a sinusoid on the geocentric range-rate function. The amplitude and phase of this sinusoid can provide the right ascension and declination of the spacecraft, given the station coordinates are sufficiently accurate. Doppler data recorded over a single pass can be used to determine the spacecraft range-rate, right ascension and declination. Data from multiple passes can consequently be used to obtain a geocentric range. However, note that the right ascension and declination provided by VLBI observations (as discussed in Section 4.3.4) are substantially more accurate (e.g. Thornton and Border 2003).

Contrary to range measurements, analysis by Iess et al. (2014) has shown that systematic errors are negligible for Doppler observables. An overview of the most important error sources and mitigation methods is provided in Section 4.6.

4.3.4. Very Long Baseline Interferometry

Very Long Baseline Interferometry (typically referred to as VLBI) is a radiometric tracking technique which acquires angular position measurements (typically the spacecraft right ascension α and declination δ). A typical VLBI observation geometry is indicated in Figure 4.2. During a VLBI measurement, two distant receivers (radio telescopes) will simultaneously track the spacecraft (e.g. Dirkx 2015; Lanyi et al. 2007). Due to the geometry the radio signal originating from the spacecraft arrives at one of the station with a slight propagation delay τ_g, typically referred to as the VLBI delay. Next to the spacecraft, both radio telescopes track an angular nearby reference source such as a quasar ("*the centre of a galaxy (= group of stars) that is very far away, producing large amounts of energy*" [2]) which represent an inertial reference frame (as discussed in Section 3.3.2). When both the propagation delay τ_g and the baseline vector $\vec{B}$ between both radio stations are known, the two-dimensional unit vector $\hat{s}$ can be determined. This vector is in the direction of the line-of-sight of the spacecraft and can be obtained using Equation 4.3 (Lanyi et al. 2007) in which c represents the speed of light.

$$\tau_g = \vec{B} \cdot \frac{\hat{s}}{c} \tag{4.3}$$

This procedure enables the determination of one angular component of the position of the spacecraft along the celestial sphere. When two independent VLBI measurements are available, using two independent baselines for both the spacecraft and the reference source, both angular components (right ascension and declination) of the spacecraft lateral position can be determined (e.g. Lanyi et al. 2007). The VLBI delay accuracy is, however, still influenced by the extent to which it can be calibrated to account for, among others, station clock offsets, baseline orientation errors and interplanetary plasma delays. By combining Equation 4.3 for both the spacecraft and the reference source, the aforementioned uncalibrated errors are typically removed (as the signals originating from the spacecraft and the reference source experience approximately the same propagation delay as their path through the interplanetary plasma is almost similar) and the angular position of the spacecraft can be determined in an inertial reference frame (e.g. Dirkx 2015; Lanyi et al. 2007; Thornton and Border 2003).

[2] Cambridge Dictionary "Quasar Meaning in the Cambridge English Dictionary" dictionary.cambridge.org `https://dictionary.cambridge.org/dictionary/english/quasar` (accessed May 15, 2018)

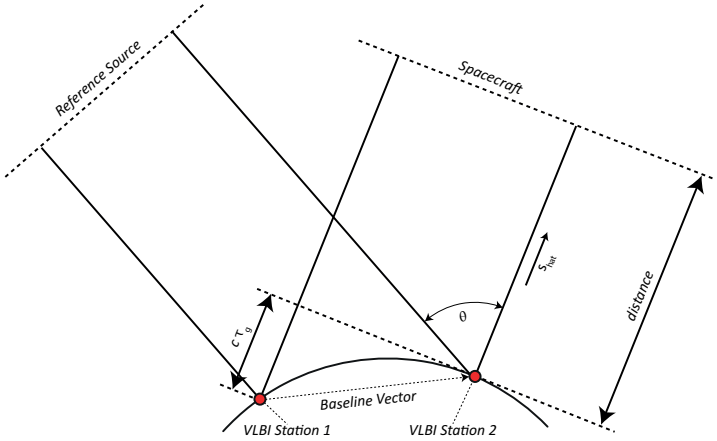

Figure 4.2: Illustration of the working principle of the generation of a VLBI directional observable.

The propagation delay τ_g is determined by cross-correlating the recorded signals of both tracking stations. When the measurements are obtained using a single frequency channel, the total delay is composed of a fraction of a cycle and an integer number of cycles (e.g. Lanyi et al. 2007; Thornton and Border 2003). Therefore the total delay contains a cycle ambiguity. Lanyi et al. (2007) discuss two demonstrated methods to resolve the cycle ambiguity. The first is Δ Differential One-way Ranging (typically referred to as Δ DOR which is an acronym for Delta-Differential One-way Ranging) for which the interested reader is referred to Lanyi et al. (2007).

The second method is Very Long Baseline Array (VLBA) and is relevant within the context of PRIDE-JUICE. In this case phase referencing is used to solve the cycle ambiguity (Lanyi et al. 2007). To this end, a large number of telescopes (usually around 10) are used to simultaneously track both the spacecraft and the reference source. The pairs of received signals are correlated and the respective correlation coefficients form so called images. In this images, the propagation delay is consequently represented by the phase delay of the correlation coefficients (between all the pairs of received signals). The phase-delay cycle ambiguity is determined by the image forming capacity of the ten-station telescope (containing 45 baselines) (Lanyi et al. 2007). Subsequently, a differential image is generated for the spacecraft which is referenced to the phases of the correlation coefficients of the reference source. Finally, the total phase delay of both the spacecraft and reference source (reconstructed using the differential image) for all receiver pairs is used to statistically estimate the spacecraft lateral position.

The advantage of VLBA with respect to ΔDOR is that no DOR tones are required and the reception of the telemetry does not have to be interrupted (something which is necessary for ΔDOR). Subsequently, VLBI measurements can be obtained as long as the spacecraft is transmitting signals towards Earth. Another advantage of VLBA with respect to ΔDOR is that the observations are less susceptible to for example bad weather condition or malfunction at individual tracking stations which is a result of the large number of tracking stations (e.g. Lanyi et al. 2007). However, this large network of tracking stations results in a more costly operation and therefore limits the number of possible tracking arcs. Finally, VLBA has a demonstrated angular accuracy which is higher than for ΔDOR, respectively 1 nrad and 2 nrad for X-band tracking signals (Lanyi et al. 2007).

An effective method of removing systematic errors such as tropospheric and ionospheric delays as well as error in Earth orientation parameters (e.g. polar motion) and station location is called in-beam phase referencing. This is achieved by observing the quasar, which has an angular distance close to the spacecraft, at the same time as the spacecraft (Border and Koukos 1993; Lanyi et al. 2007). The latter ensures the commonality of the signal originating from both the spacecraft and the quasar (Iess et al. 2014). Furthermore, the location of a quasar is known with a high accuracy. Thus, the small angular (such that the telescope remains stationary) and temporal separation (such that both signal experience similar troposperic and ionospheric path delays) enable an lateral position of the spacecraft which is almost unaffected by systematic errors (Majid and Bagri 2008). An overview of the most important error sources and mitigation methods is provided in Section 4.6.

4.4. Space-Based Optical Astrometry

Space-based astrometry has been extensively used for accurate orbit modeling of natural solar system bodies. For example, the narrow angle camera from the Cassini Image Science Subsystem (ISS) has been used to obtain lateral position observables of many different Saturnian moons (Tajeddine et al. 2015). Space-based astrometry is based on the principle of reduction of images provided by space-based camera systems (such as the JANUS camera on JUICE or the ISS (Imaging Science Subsystem) Narrow Angle Camera (NAC) on Cassini) to obtain a lateral position of planetary bodies.

A method to obtain a lateral position (i.e. the satellite right ascension α_s and declination δ_s) from images provided by space-based camera systems is described by, among others, Duxbury and Callahan (1981); Pasewaldt et al. (2012); Tajeddine et al. (2013). This method is roughly divided in three steps.

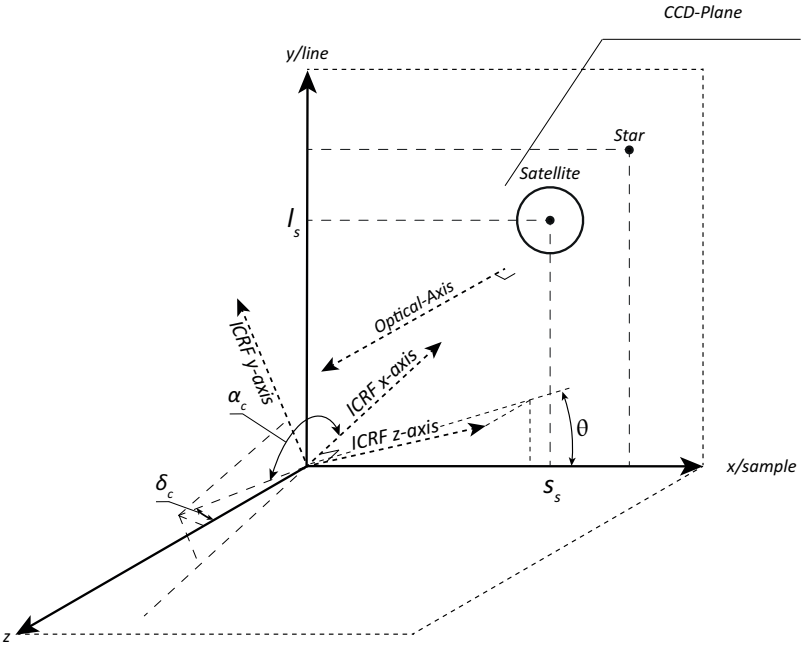

Figure 4.3: Geometry of a space based camera system with respect to an inertial reference frame.

1. Before determining the center of the observed moon, the image needs to be astrometrically calibrated. To this end, the right ascension and declination of the optical axis of the camera (axis perpendicular to the charge-coupled device (CCD) through the center of the camera's field-of-view) is determined using the spacecraft pointing history. Together with the field-of-view of the camera the available reference stars which are present on the image can be determined. The coordinates of the reference stars are subsequently projected (after correcting their position for, among others proper motion and aberation) on the plane of the CCD (perpendicular to the optical axis) of the camera using a sample and line (s, l) coordinate system which has its origin in the bottom left corner (Tajeddine et al. 2013). For the actual calibration, the sample and line scale factors ρ_s and ρ_l (which map angular resolution) as well as the right ascension α_c, the declination δ_c, and the twist angle θ have to be fitted for each image. This is accomplished using a least-squares algorithm in which the measured star positions are fitted to the respective cataloged positions. The twist angle θ is defined as the angle between the projected ICRF z-axis on the spacecraft xz-plane and the spacecraft z-axis (see Figure 4.3), and thus provides a measure of the rotation of the image with respect to an inertial reference frame around the optical axis. α_c, δ_c, and θ combined give the all the required rotations to indicate the current rotation of the spacecraft camera with respect to inertial space. The aforementioned parameters are visualized in Figure 4.3. As soon as the center of the satellite is determined in sample and line coordinates(s_s, l_s), the satellite right ascension and declination can be determined using the five aforementioned fitted variables.

2. After the astrometric calibration, the apparent limb (i.e. the part of the moon that is visible) is measured. Tajeddine et al. (2013) describe the limb measurement process in three steps. First the pixel intensity across a horizontal profile (all sample coordinates for a given line coordinate) a is measured. Typically, a large jump in the pixel intensity is found at the terminator (edge) of the limb in the direction of the Sun while a gradual decrease in pixel intensity is found at the terminator of the limb opposite to the direction of the Sun. The latter gives rise to systematic errors which are discussed in Chapter 5. Secondly, the absolute value of the derivative of the aforementioned pixel intensity is determined. The sample or line pixel with the highest absolute derivative of the pixel intensity corresponds to the sample or line position of the edge of the limb. This process is repeated for all sample and line combinations to determine the coordinates of the detectable limb in the third and final step.

3. Finally, the detected limb points must be fitted to the reference ellipse as described by Tajeddine et al. (2013). The JPL SPICE library delivers approximate ellipsoids which are parametrized by the center coordinates, the semi-major and semi-minor axis as well as the orientation of the ellipse ϕ. These parameters are fitted to the measured limb points using a least-squares algorithm yielding the sample and line coordinates of the center of the satellite. The fitted sample and line coordinates of the center of mass of the satellite can subsequently be used to obtain the right ascension and declination utilizing the five calibration parameters as discussed in the first step. An elaborate discussion on uncertainties associated with the astrometric reduction of the images is given in Chapter 5.

4.5. Comparison of Tracking Types

Contrary to range, VLBI, and optical astrometry which are absolute observations, Doppler tracking provides a relative observation. As a result the noise profile of Doppler observations is close to Gaussian (Dirkx et al. 2018). Consequently, Doppler observations are not affected by systematic errors. Therefore, a Doppler (range-rate) observation with a noise level of 0.01 mm/s and an integration time of 60 seconds is susceptible to observe signatures in the dynamics with a range difference of 0.6 mm. This is substantially lower than the observable signature of an absolute range observation with an accuracy of 20 cm (Dirkx 2015).

Therefore, in most planetary missions (in which the orbital period or flyby tracking arc is relatively short) the dynamics of the spacecraft is fully constrained by the Doppler observations (e.g. Cicalò et al. 2016). Moreover, during the flybys, Doppler data is also crucial in determining the ephemerides of the moons. This is related to the limited signature in the data (a tracking arc lasts only 8 hours) over the course of a flyby such that the dynamics of the moons are better constrained in the range-rate observations (for which the observability is much smaller compared to the absolute observations).

Nevertheless, the JUICE mission differs to most other missions due to orbital phase around Ganymede (Dirkx et al. 2017). During this phase, the dynamics of Ganymede can be observed over multiple orbits. Therefore allowing multiple signatures to build up in the observed dynamics. The most import being the orbit of Ganymede around Jupiter (with an orbital period of 172 hours) and the orbit of JUICE around Ganymede (with an orbital period of approximately 3 hours). Cicalò et al. (2016) conclude that for the tracking system of the Bepicolombo mission (which is similar to the tracking system that will be used on JUICE) range observations are better in constraining signatures with a period larger than 10^5 seconds (approximately 28 hours), compared to the Doppler data.

Thus, the Doppler data is especially useful in determining the orbit of the spacecraft (during both the Jovian and Ganymede tour) as well as the estimation of the ephemerides of the Galilean moons during the flybys (due to the low temporal signature of the dynamics of the Galilean moons in the observations). For the Ganymede tour, however, the range and VLBI observations are crucial in estimating the ephemerides of Ganymede.

4.6. Observation Uncertainties and Enhancements of Radiometric Tracking Techniques

The most important error sources for the tracking types discussed in Section 4.3 will be listed in Section 4.6.1. Subsequently, possible enhancements to reduce the impact of these errors are discussed in Section 4.6.2 and are particularly focused on the implementation of a multi-frequency radio system.

For other enhancements the interested reader is referred to Iess et al. (2014). The observational uncertainties as well as the enhanced uncertainties are discussed in Section 4.6.3. Note that this section only focuses on radiometric tracking. The uncertainties for optical space-based astrometry are discussed in more detail in Section 5.3.

4.6.1. Main Error Sources for Radiometric Tracking

Iess et al. (2014) defines four main error sources that are relevant for radiometric tracking of planetary spacecraft. These error types, and their corresponding magnitude, are listed below.

1. Interplanetary and ionospheric plasma noise. These error sources are relevant for range, range-rate, and VLBI. The corresponding magnitude of this error is 0.012 mm/s to 0.039 mm/s for Doppler observations and 350 m to 800 m for range observations depending on the Sun-Earth-Probe (SEP) angle (Iess et al. 2014). This angle indicates how close the signal is propagating to the solar corona.

2. The wet tropospheric noise (as a result of water vapor) which affects mostly range-rate and VLBI observations. The magnitude of the range-rate error ranges from 0.009 mm/s to 0.030 mm/s as a result of seasonal variations (Iess et al. 2014).

3. Numerical noise which only affects range-rate observations. This is a result of numerical and truncation errors in the generation of the computed observations from the number of counted Doppler cycles. This magnitude of the numerical noise ranges between 0.015 mm/s and 0.019 mm/s for respectively Cassini and Rosetta (Iess et al. 2014).

4. Multipath effects and time varying phase delays in the on-board and ground based antenna systems which only affect range. The magnitude of this error is approximately 150 m (Iess et al. 2014).

A large number of mitigation strategies were discussed by Iess et al. (2014) to reduce the magnitude of the aforementioned error sources. The largest improvement can be realized by adopting a multi-frequency radio system (which tracks at both the X- and Ka-band) such that the interplanetary and ionospheric plasma noise can be almost completely omitted. This system, and the consequences on the resulting errors will be further discussed in Section 4.6.2.

Furthermore, the wet tropospheric noise (which is non-dispersive and is thus not reduced by adopting a multi-frequency tracking system) can be largely reduced by a media calibration system (which comprises different meteorological instruments located in close proximity to the tracking station). Moreover, the numerical noise can be reduced by using quadruple precision in the generation of the Doppler observations from the counted Doppler cycles. In this way the machine epsilon is reduced thereby reducing the accompanying numerical noise.

4.6.2. Multi-Frequency Radio System using X-band and Ka-band

Different observation types are affected by different error types and the resulting standard deviations thus vary per observation type. However, one error type is dominant for all radiometric tracking types (see Section 4.6.1), which are interplanetary and ionospheric plasma errors (e.g. Dirkx 2015; Iess et al. 2014). This type of error shows a large variation with the Solar separation or Sun-Earth-Probe (SEP) angle. A low SEP angle causes the signal to pass close to the Sun, where the influence of the plasma is higher due to a higher plasma density (e.g. Dirkx 2015). Moderate SEP angles cause ranging errors on the meter level, whereas small SEP angles cause ranging errors up to tens of meters. Iess et al. (2014) show that for Doppler range-rate observations there is a noise floor near solar opposition (high SEP angle), and that the Allen deviation (which is a measure for frequency stability of the signal) is at least one order of magnitude smaller for higher SEP angles.

This error type can, however, be significantly reduced by measuring at the Ka-band instead of the X-band as the shorter wavelength of the Ka-band is less affected by the ionosphere and solar plasma (Thornton and Border 2003). Unfortunately, this is improvement is only present for sufficiently large SEP angles, as otherwise the signal has to propagate through the solar corona. Fortunately, the Cassini solar conjunction experiment has successfully demonstrated a multi-frequency system which is capable of nearly completely omitting interplanetary plasma noise (Iess et al. 2014). Such a system tracks the

spacecraft by simultaneously using multiple links at different wavelengths, which are the X-band up-link and X-band down-link (X/X), X-band up-link and Ka-band down-link (X/Ka) and Ka-band up-link and Ka-band down-link (Ka/Ka) (Iess et al. 2014). This multi-frequency tracking system makes radiometric observations nearly immune to interplanetary plasma, and thus less dependent on the SEP angle. This, however, means that all used ground stations must be equipped with hardware which supports simultaneous transmission of multiple wavelengths and reception of three coherent carriers (Iess et al. 2014). Furthermore, spacecraft should be equipped with a transponder that supports simultaneous transmission of the aforementioned radio links. This will be at the expense of a higher mass and power. The improved uncertainties for the different types of radiometric tracking observables after considering the multi-frequency tracking system and the improvements stated in Section 4.6.1 can be found in Section 4.6.3.

However, Majid and Bagri (2008) argue that the estimated performance of in-beam phase referencing (as discussed in Section 4.3.4 for VLBI) is not very good. This as the beam area is a factor 15 smaller at the Ka-band compared to the X-band. Furthermore, the number of currently available reference sources is substantially lower at Ka-band. Fortunately, progress in the development of the celestial reference frames at the Ka-band is made by, for example, adding new ground stations and consequently generating more baselines (Malkin et al. 2015).

4.6.3. Current and Improved Error Values

This section summarizes the standard deviations for the different tracking types relevant within JUICE mission. An overview of the current state-of-the-art as well as the improved standard deviations is given in Table 4.1. The improved standard deviations as listed in the second column can be attained using the multi-frequency radio tracking system as discussed in Section 4.6.2 as well as other enhancements presented by Iess et al. (2014). Furthermore, the third column gives a regular attainable observation cadence.

The standard deviations presented in this table will be used as input for the weighting matrix and scheduling of the observations as discussed in Chapter 6. As the standard deviation of some tracking techniques (especially VLBI) is dependent on improvements which are currently not realized, a range of standard deviations is used for analysis to observe the resulting behavior. Such an approach was used by Dirkx et al. (2017) and will be further discussed in Chapter 6.

Table 4.1: Current and improved accuracies for different tracking techniques

Observable	Current σ	Improved σ	Cadence	Reference
Ranging	1-5 m	0.2 m	5 min	(Iess et al. 2014)
Doppler	0.1 mm/s @ 60 s	0.01 mm/s @ 60 s	1 min	(Iess et al. 2014)
VLBI				
ΔDOR	6-15 nrad	1 nrad	1-2 times a year	(Curkendall and Border 2013; Iess et al. 2014)
VLBA	1 nrad	0.1 - 1 nrad	1-2 times a year	(Dirkx et al. 2017; Lanyi et al. 2007; Majid and Bagri 2008)

4.7. Observation Viability Conditions

Unfortunately, it is not always possible to acquire tracking observations because of operational restrictions. To this end the list of operational constrains considered within this thesis is presented in this section and is divided among constraints for radiometric tracking and constraints for optical tracking which are discussed in Section 4.7.1 and 4.7.2 respectively.

4.7.1. Operational Constraints for Radiometric Tracking Observables

As discussed in Section 4.6.2 interplanetary plasma is a significant error source for all radiometric tracking types. Even though multi-frequency tracking systems remove a large part of this error, Boutonnet

and Varga (2017) - CReMA 3.2 documentation - require a minimum SEP angle to avoid progressive degradation and interruption of the spacecraft link. This requirement is enforced by removing observations for which the SEP angle is smaller than 5 degrees. The SEP angle refers to the center of the Sun and the Earth. The latter is justifiable as the angular size of the Sun at the position of Jupiter is close to zero. In total the Earth will be occulted 7 times by the Sun during the complete JUICE mission. The duration of the occultations ranges from 12 to 19.5 days (Boutonnet and Varga 2017). Especially the fifth and sixth occultation are critical and might potentially conflict with flybys 10C2 and 24G10, which makes tracking during these flybys impossible.

In addition to the requirement of on the SEP angle, the spacecraft needs to be visible from the Earth to establish a radio link. In other words, the Earth, from the viewpoint of the spacecraft, should not be occulted by either Jupiter or the Galilean moons. The occultations by Europa and Callisto are only relevant during their respective flybys and are negligible according to Boutonnet and Varga (2017). Ganymede occultations, however, are especially important around Ganymede Orbit Injection (GOI) as the beta angle [3] is 20 degrees. A low beta angle represents an orbit which regularly experiences eclipses. As the Earth has a close angular proximity to the Sun, the epochs of Earth occultations are closely related to solar eclipses. Grasset et al. (2013) show that the beta angle gradually increases to 90 degrees over the time-line of the Ganymede orbital phase. This means that the solar eclipses and thus the Earth occultations by Ganymede gradually vanish. For Jupiter, the occultations are relevant throughout the complete mission time-line.

The Jupiter occulations on the other hand can be divided among two different phases (Boutonnet and Varga 2017), one before GOI and one after GOI. Before the Ganymede orbital phase the occultations by Jupiter are only dependent on the spacecraft trajectory. Most of the occultations which coincide with the visibility of a ground stations take place in mission phase 5 (transfer to Ganymede as discussed in Section 2.6.3). After GOI, the occultations by Jupiter are essentially a function of the orbital period of Ganymede around Jupiter and thus occur more frequently.

The aforementioned types of occultations are modeled using the shadow function as presented in Montenbruck and Gill (2012) and assuming the occulted body (Earth) to be a point rather than an extended body. This means that the penumbra does not exist and the spacecraft either is in umbra or sunlight (i.e. is visible from the Earth). For this thesis it is assumed that the Earth is visible (i.e. not being occulated) when the shadow function is larger than or equal to $1 \cdot 10^{-10}$.

4.7.2. Operational Constraints for Optical Tracking Observables

As discussed in Section 4.4 the astrometric reduction of the satellite images provided by a space-based camera system involves a large number of steps and its accuracy is highly dependent on, among others, the number of stars available for calibration or the accuracy to which the limb can be fitted. Boutonnet et al. (2018) - CReMA 4.0 documentation - give a list of requirements for the baseline navigation analysis applicable to the navigation camera (NavCam). The most important parameters are summarized in Table 4.2, in which the first column denotes the specific requirement and the second column its associated value. Although, these requirements are applicable to the NavCam, the same set of requirements is used for JANUS within the context of this thesis.

Table 4.2: Most relevant requirements for optical navigation (Boutonnet et al. 2018).

Parameter	Value
Covered time span	1G1 – 4 days up to GOI
Minimum pixels to be filled by the moon	5
Maximum fraction of FoV that is allowed to be filled by the moon	$1/\sqrt{5}$
Minimum Sun-spacecraft-Moon angle	$30°$
Minimum Jupiter-Limb-spacecraft-Moon angle	$5°$ for apparent Jupiter size $> 4°$
Maximum Sun-Moon-spacecraft angle	$130°$
Time around closest approach without optical navigation	± 12 hrs
Optical navigation default frequency	Once every 12 hrs
Optical navigation priority order	Ganymede, Europa, Callisto

[3] Angle between vector between the central body and the Sun and its projection onto the orbital plane.

From the table it can be seen that Boutonnet et al. (2018) only consider optical navigation observations during the Jovian tour but not in the period centered 24 hours around the closest approach of a flyby. These epochs are excluded as other science and instruments have a higher priority and require stringent pointing requirements which makes navigational observations impossible.

Boutonnet et al. (2018) furthermore consider a minimum and maximum size of the satellite within the field-of-view of the image. For all optical observations it is assumed that the optical axis (see Section 4.4) points directly to the satellite of interest. In this way, the size of the image at the position of the satellite can be computed using Equation 4.4 in which || || denotes the L2 norm.

$$d_{image} = 2\tan(FoV_{cam}/2)||\vec{r}^{i}_{sc}||_2 \tag{4.4}$$

The fraction of the image that is filled by the satellite can be calculated by dividing the diameter of the satellite by d_{image}. The spatial resolution can be calculated by dividing d_{image} by the number of pixels. Subsequently, the number of pixels filled by the moon can be calculated by dividing the diameter of the satellite by the spatial resolution and subsequently calculating the area represented by the satellite in pixels.

The limit on the maximum Sun-spacecraft-Moon angle ensures the angular separation between the satellite and the Sun such that the brightness of the Sun (which is significantly higher than the reference stars) does not complicate the astrometric reduction (e.g. by reducing the number of visible reference stars) and does not damage the CCD. The limit on the minimum Jupiter-Limb-spacecraft-Moon angle is introduced as the astrometric reduction is complicated when Jupiter is in field of view for two reasons. Jupiter might occult reference stars or its brightness might reduce the number of observable reference stars. Finally, the Sun-Moon-spacecraft angle (or phase angle) should be lower than 130 degrees to ensure the satellite's visible limb is large enough to fit accurately fit the reference ellipse. High phase angles will result in less accurate observations (Cooper et al. 2014).

Boutonnet et al. (2018) state a priority order of Ganymede, Europa, and Callisto but do not consider Io as Io is not especially relevant within the JUICE mission. However, in this thesis Io is included to analyze whether its inclusion might improve the attainable condition number.

5

Covariance Analysis

This chapter discusses the necessary theory to employ a covariance analysis. First of all the general theory of orbit determination using linear least-squares is discussed in Section 5.1 which also includes information regarding the formal errors and the condition number. Furthermore, the method used to determine the weights in the covariance analysis is discussed in Section 5.2 and 5.3 for respectively the radiometric and optical tracking types.

5.1. Orbit Determination

This section discusses the orbit determination theory which is required to employ a covariance analysis. First of all, Section 5.1.1 discusses the general principles of the weighted linear least-squares algorithm. Subsequently, Section 5.1.2 discusses how a covariance analysis can be used to determine the formal errors. Finally, the condition number (which is a measure of the stability of the normal equations matrix) is introduced in Section 5.1.3.

5.1.1. Linear Least-Squares

A method that is often used in precise orbit determination to estimate the initial conditions of both artificial and natural satellites as well as associated model parameters (e.g. body masses, coefficients of oblateness, etcetera) is the weighted least-squares estimation algorithm. In this section the most important aspects regarding this method are discussed. To this end, assume the state for N satellites is given by Equation 5.1, in which $\vec{p} = (p_1, \dots, p_M)^T$ are M physical model parameters.

$$\vec{x}(t) = \begin{pmatrix} \vec{r}_1(t) \\ \vdots \\ \vec{r}_N(t) \\ \vec{v}_1(t) \\ \vdots \\ \vec{v}_N(t) \\ \vec{p} \end{pmatrix} \tag{5.1}$$

Assume that the derivative of the state vector x is described by an ordinary differential equation as showed in Equation 5.2. Furthermore, the initial value of the state vector is given by $\vec{x}_0 = \vec{x}(t_0)$, in which t_0 is the initial epoch.

$$\dot{\vec{x}} = f(t, \vec{x}) \tag{5.2}$$

The goal of the least-squares estimation algorithm is to obtain the initial states of all N satellites as well as the relevant model parameters, which are included in $\vec{p}$. The vector $\vec{c} = \vec{x}(t_0)$ represents the state vector as presented in Equation 5.1 for $t = t_0$. The exact solution of $\vec{c}$ can be approached in an iterative manner using a weighted linear least-squares estimation for which the least-squares update is shown

in Equation 5.3. Note that the W matrix denotes the weighting matrix which accounts for the different uncertainties of the different observation types (as discussed in Section 4.6.3).

$$\Delta\vec{c}^{LSQ} = (H^T W H)^{-1}(H^T W \Delta\vec{z}) \tag{5.3}$$

In this equation $\Delta\vec{z}$ is the difference between the observed and computed observations and H denotes the Jocabian matrix which contains the partial derivatives of the computed observation equation with respect to the state vector $\vec{c}$. The entries (rows) of the H matrix are computed using Equation 5.4 (Dirkx 2015) for all associated observations. In this way, starting with a reference solution $\vec{c}^{ref}$ which is known beforehand. The exact value of $\vec{c}$ can be approached in an iterative manner by updating $\vec{c}^{ref}$ with $\Delta\vec{c}^{LSQ}$ to obtain $\vec{c}^{LSQ}$. In the next iteration, H and $\Delta\vec{z}$ can be recomputed using the updated value of $\vec{c}^{LSQ}$. This iteration continues until the difference of $\vec{c}^{LSQ}$ between two successive iteration is smaller than a predetermined tolerance.

$$\left(\frac{\partial h_l^k}{\partial \vec{c}}\right) = \sum_j \left(\frac{\partial h_l^k}{\partial \vec{x}}(t_j)\bigg|_{\vec{p}=\text{const}} \frac{\partial \vec{x}}{\partial \vec{c}}(t_j)\right) + \frac{\partial h_l^k}{\partial \vec{c}}\bigg|_{\vec{x}=\textbf{const}} \tag{5.4}$$

In this equation h_l^k models the observable of type l referring to body k at epoch t_j. The derivative of the state vector $\vec{x}$ at epoch t with respect to the state vector at the initial epoch $\vec{c}$ is given in Equation 5.5 (Dirkx 2015). In this equation N refers to the number of satellites which are included in the state vector, where M denotes the number of model parameters. Finally O and I refer to a matrix containing all zeros and the identity matrix respectively. The size of the particular matrices is denoted in the subscript in Equation 5.5.

$$\frac{\partial \vec{x}}{\partial \vec{c}} = \begin{pmatrix} \Phi(t, t_0) & S(t) \\ \mathbf{0}_{M\times 6N} & \mathbf{I}_{M\times M} \end{pmatrix} \tag{5.5}$$

In this equation $\phi(t, t_0)$ represents the state transition matrix relating the state $\vec{x}(t)$ to the initial state $\vec{c}$. Furthermore, $S(t)$ represents the sensitivity matrix which describes the dependence of the model parameters (which are included in $\vec{p}$) on the accelerations acting on the satellites. The W matrix in Equation 5.3 represents the weighting matrix and is given by Equation 5.6 in which R denotes the total number of observations.

$$W = \begin{pmatrix} \sigma_1^{-2} & & 0 \\ & \ddots & \\ 0 & & \sigma_R^{-2} \end{pmatrix} \tag{5.6}$$

The diagonal entries of the weighting matrix contain the inverse square of the mean measurement error or standard deviation σ_i of the corresponding observation (Montenbruck and Gill 2012). The standard deviation σ_i should contain the total measurement error, comprising both random noise and systematic errors. In the particular case that the measurement errors are correlated, the weighting matrix W becomes non-diagonal. More elaboration on the quality of the data and the weights is given in Section 5.2 and 5.3.

The iterative nature of the least-squares parameter estimation makes this process time-consuming. The latter is especially true compared to a covariance analysis which rquires only one function evaluation as will be discussed in Section 5.1.2. Therefore, in most studies in which the sensitivity of the observation uncertainties is assessed, a covariance analysis is performed (e.g. Dirkx et al. 2017). Such an analysis yields a formal error which can be related to the uncertainty in the estimated parameters that can be achieved. This is further discussed in Section 5.1.2.

5.1.2. Covariance Analysis

In the ideal case, when no measurement errors are present, the least-squares estimate $\vec{c}^{LSQ}$ will be equal to the actual state $\vec{c}$. However, when measurement errors are present, it is interesting to know

how these measurement errors influence the least squares solution $\vec{c}^{LSQ}$. An often used method to acquire information about the error of the least-squares solution is a covariance analysis. The covariance describes the squared mean standard deviation of the least-squares solution $\vec{c}^{LSQ}$ with respect to the actual state $\vec{c}$. Assuming the error vector $\vec{\epsilon}$ (denoting the error between the observed and computed observations) to be normally distributed as well as neglecting systematic errors, the following expression as given in Equation 5.7 can be used to obtain the covariance matrix P (Montenbruck and Gill 2012).

$$P = \text{Cov}(\vec{c}^{LSQ}, \vec{c}^{LSQ}) = (H^T W H)^{-1} \tag{5.7}$$

From its definition, it can be seen that the covariance matrix P should be a NxN square matrix (where N is the number of parameters, both initial states and model parameters that are estimated). Furthermore, P must be positive definite as long as it exists since it is computed by inverting the positive definite matrix $H^T W H$ (Schutz et al. 2004). The square root of the diagonal terms of the covariance matrix P yields the standard deviation of the state vector elements $\sigma_{q,k} = \sqrt{P_{kk}}$. These errors (or standard deviations) are usually referred to as formal errors, whereas the real difference between the actual and modeled observations is referred to as true errors. The ratio between those different error terms is called the true to formal error-ratio. Furthermore, the off-diagonal terms of the P matrix indicate the correlation between the errors of the different state vector elements.

Care should be taken using the covariance P, as both $\vec{c}$ and $\vec{\epsilon}$ are considered to be normally distributed. Therefore Montenbruck and Gill (2012) describe the resulting covariance P as how the least square estimate $\vec{c}^{LSQ}$ would be distributed around the actual state $\vec{c}$ in case of measurements with normally distributed noise. In case systematic errors $\bar{\vec{\epsilon}}$ are present, there will be an offset $\delta\vec{c}^{LSQ}(\bar{\vec{\epsilon}})$ which is a function of those systematic errors. As the estimation of the orbit of the spacecraft and the generation of the satellite ephemerides are decoupled, the observations (especially during the Jovian tour) are biased such that actual formal errors will include an offset $\delta\vec{c}^{LSQ}(\bar{\vec{\epsilon}})$. Another drawback of a covariance analysis is caused by the fact that the covariance matrix is only dependent on the a-priori estimated measurement errors. These are included in the weighting matrix W and are used to normalize the H matrix between 0 and 1. Consequently, the covariance matrix can only be used as an a-priori measure of the attainable accuracy as a function of the data quality and distribution (Montenbruck and Gill 2012). Thus, the interpretation of the formal errors is not strictly accurate in a statistical sense (Schutz et al. 2004). Finally, the rank of the covariance matrix gives an indication on the observability of the vector $\vec{c}$. The vector $\vec{c}$ will be observable only if it can be uniquely determined by the observations (Schutz et al. 2004).

Thus the resulting formal errors are not valid in a statistical sense and are generally optimistic (planetary ephemerides typically have a true-to-formal error ratio of 2-3 (Dirkx et al. 2017)) due to both the the a-priori estimation of the uncertainty and the fact that the real observations are biased (due to the decoupling of the estimation of the orbit of JUICE and the generation of the ephemerides which will be discussed in Section 5.2.1). Nevertheless, the goal of this thesis is to assess the relative contribution of the space-based optical astrometry to the improve the observability in the observations of especially Io and to a lesser extend Europa. Furthermore, optimization of the observation schedule for the optical astrometry requires a large number (>3,200,000) of function function evaluations which would be impossible for methods which estimate the true error more realistically (Dirkx et al. 2017).

5.1.3. Condition Number

As discussed in Section 5.1.2, to be able to solve for the initial state vector $\vec{c}$ this vector needs to be observable. In other words, the number of observations should at least be equal to the number of unknowns (N initial sates and M model parameters). However, in the presence of random measurement errors, more observations are required to reduce the effect of these errors. Furthermore, the tracking geometry and distribution have a significant impact on the normal equations matrix. In case many observations provide a similar temporal signature on the H matrix, the observables do not provide enough information to estimate the full state vector $\vec{c}$. This occurs, for example, in case of the Europa flybys which are closely separated in time such that the dynamical evolution can be hardly constrained using the observations from the respective flybys. In this case the normal equations matrix $H^T W H$ will be singular or close to singular and will give rise to numerical difficulties (Montenbruck and Gill 2012).

A singular or close to singular normal equations matrix $H^T W H$ will make the least squares solution $\vec{c}^{LSQ}$ extremely sensitive to small errors in the normal equations matrix. An often used figure to indicate the quality with which the solution is defined by the available measurements is the condition number κ (Montenbruck and Gill 2012). The condition number is mathematically defined by Equation 5.8 (Gratton 1996).

$$\kappa(H) = ||H||_2 ||H^+||_2 \tag{5.8}$$

In this equation H^+ is the Moore-Penrose inverse of H which is defined by $H^+ = (H^* H)^{-1} H^*$ in which H^* is the conjugate transpose which reduces to H^T in case the field over which the vector space is spanned is real (which is clearly the case for an orbit determination problem). Therefore, in case the rank of the matrix H is equal to the length of $\vec{c}$ (in other words the vector $\vec{c}$ is observable and H is a square matrix with full rank), the Moore-Penrose inverse H^+ reduces to H^{-1} (e.g. Golub and Van Loan 2012; Gratton 1996). Furthermore, $||H||_2$ denotes the 2-norm of the H matrix which is equal to the square root of the maximum eigenvalue or the maximum singular value of H as shown in Equation 5.9 (e.g. Meyer 2000).

$$||H||_2 = \sqrt{\lambda_{max}(H^T H)} = d_{max}(H) \tag{5.9}$$

In this equation $\lambda_{max}(H^T H)$ is the maximum eigenvalue of the matrix product $H^T H$ which is equal to the square root of the maximum singular value $d_{max}(H)$ of the normal equations matrix H (Montenbruck and Gill 2012). Subsequently, substituting Equation 5.9 into Equation 5.8 as well as employing that for a normal equations matrix with full rank $H^+ = H^{-1}$, the condition number is defined by Equation 5.10 (e.g. Montenbruck and Gill 2012).

$$\kappa(H) = \frac{d_{max}(H)}{d_{min}(H)} = \frac{\sqrt{\lambda_{max}(H^T H)}}{\sqrt{\lambda_{min}(H^T H)}} \tag{5.10}$$

A low condition number indicates that the least square solution $\vec{c}^{LSQ}$ is less sensitive to errors in the normal equations matrix H and thus corresponds to a well posed problem. This means that a large number of significant digits in the estimated solution can be retained. A high condition number corresponds to an ill posed problem in which the H matrix is close to singular. This means that the least squares solution is extremely sensitive to errors in the normal equations matrix and a limited number to no significant digits of the estimated solution can be retained. In their analysis on the relative contribution of PRIDE-JUICE Dirkx et al. (2017) have found condition numbers of $\mathcal{O}(10^{16})$ for the matrix inversion as given by Equation 5.7. In principle a condition number of ∞ indicates a singular H matrix. However, to ensure the least squares solution $\vec{c}^{LSQ}$ is not very sensitive to errors in the normal equations matrix, the inverse of the condition number should be higher than a predefined value. This value is usually related to the machine accuracy ϵ_{mach} to ensure the solution has enough significant digits (Montenbruck and Gill 2012). Cheney and Kincaid (2012) state that a condition number of the matrix A equal to $\kappa(A) = 10^k$ will result in the loss of at least k digits of precision in solving the system $Ax = b$.

Using double precision, in which 52 bits are allocated for the mantissa [1], the machine epsilon is equal to $\epsilon_{mach} = 10^{-52} \approx 2.2204 \times 10^{-16}$. The number of significant digits is determined by the 52 bits of the mantissa as well as one implicit integer bit. This means that for double precision approximately $53 \log_{10} 2 \approx 16$ digits are available. In other words, the number of digits by which the numerical solution of $Ax = b$ is correct can be determined by Equation 5.11 (Cheney and Kincaid 2012).

$$d = |\log_{10} \epsilon_{mach}| - \log_{10} \kappa(A) \tag{5.11}$$

This means that when one requires the solution to have at least one significant digit, the condition number should be lower than $4.50 \cdot 10^{14}$ in case double precision is used. Note that in further analysis, the condition number is computed for the matrix product $H^T W H$, as this is the matrix which should be inverted.

[1] The part of a floating point number which represents the fraction or significant digits.

5.2. Radiometric Weights - JUICE Orbit Uncertainty

As the orbit determination of JUICE is decoupled from the estimation of the ephemerides of the Galilean moons, the orbit determination errors are set as mission settings as discussed in Section 4.2. Section 5.2.1 discusses how the decoupling of the estimation of the JUICE dynamics from the generation of the ephemerides is realized. Subsequently, Section 5.2.2 discusses how the uncertainty of the synthetic observations as discussed in Section 4.2 can be estimated after which Section 5.2.3 discusses the realism of the adopted model as well as the consequences on the resulting formal errors.

5.2.1. Decoupling of JUICE Orbit Determination

A primary parameter in the generation of the ephemerides of the Galilean moons is the position of the satellite $\vec{r}_i^J$ with respect to Jupiter, as tracked by the spacecraft during a flyby (note that the same vector notation as introduced in Section 3.1.1 is adopted). The position of the satellite $\vec{r}_i^J$ can be related to the position of the spacecraft in a barycentric reference frame $\vec{r}_{sc}^I$ using Equation 5.12.

$$\vec{r}_{sc}^I = \vec{r}_{sc}^i + \vec{r}_i^J + \vec{r}_J^I \tag{5.12}$$

In this equation the position of the spacecraft is decomposed in the position of the spacecraft with respect to the satellite, the position of the satellite with respect to Jupiter, and the position of Jupiter with respect to the Solar System barycenter. As the spacecraft orbit determination is not considered here, only the last two terms are included in the estimation using simulated tracking data. The uncertainty of the first term is, as described before, considered in a parametric fashion (Dirkx et al. 2017). This is, however, complicated by the fact that the spacecraft orbit determination and the estimated Joviocentric satellite position are strongly coupled over the course of a flyby (Dirkx et al. 2017). Therefore, Dirkx et al. (2017) state that not considering the uncertainty in the dynamics of the moon will result in a conditional uncertainty of the spacecraft. Milani and Gronchi (2010) argue that replacing the marginal uncertainty (no dependency of spacecraft uncertainty on the satellite uncertainty) by the conditional uncertainty will yield an too optimistic assessment of the result (i.e. a high true-to-formal error ratio). The conditional uncertainty of the observed dynamics of the moon and Jupiter is given in Equation 5.13 (Dirkx et al. 2017).

$$\sigma\left(\vec{r}_i^J + \vec{r}_J^I\right)|_{\vec{r}_{sc}^i=\text{fixed}} = \sigma(\vec{r}_{sc}) + \sigma(\vec{r}_{sc}^i)|_{\vec{r}_{sc}^i=\text{fixed}} \tag{5.13}$$

In this equation $\vec{r}_{sc}$ is given by Equation 5.14 (Dirkx et al. 2017). As can be seen the conditional uncertainty in the measurement of the satellite with respect to the barycentric reference frame is a function of the measurement uncertainty $\sigma(\vec{r}_{sc})$ and the uncertainty in the orbit determination of the spacecraft with respect to the satellite considered $\sigma(\vec{r}_{sc}^i)|_{\vec{r}_{sc}^i=\text{fixed}}$.

$$\boldsymbol{r}_{sc} = \boldsymbol{r}_{sc}^I - \boldsymbol{r}_E^I \tag{5.14}$$

As stated above, assuming the conditional and marginal uncertainty to be similar leads to optimistic results. However, Dirkx et al. (2017) argue that this assumption is valid for the Ganymede orbit phase as the orbit of Ganymede around Jupiter can be easily decorrelated from the orbit of the JUICE spacecraft around Ganymede (as their orbital periods are fundamentally different). However, for the flybys this is not that case. Note that the flybys are very short with respect to the orbital period of the satellite. Therefore, Dirkx et al. (2017) argue that, during the flybys, the result of uncertainty of the dynamics of the satellite, when estimating the the dynamics of the JUICE spacecraft, is that the spacecraft dynamics are biased. To this end, these biases should be estimated per arc and per observation type and should subsequently be included in the model.

Estimating the biases, considering 29 flybys and a radiometric tracking arc every day during the Ganymede tour, yields a total number of $\approx$ 400 additional parameters (assuming the baseline VLBI cadence as discussed in Chapter 6). However, the numerical difficulty for a matrix inversion scales with $\mathcal{O}(n^3)$ where n is the dimension of the square matrix (assuming Gaussian elimination (Farebrother 1988)). Therefore, the computation time of the matrix inversion increases by approximately a factor 5000. As the optimization algorithm requires many (approximately 3,200,000 evaluations according to

the settings as discussed in Chapter 6), estimation of the biases within the optimization framework is impossible. This, however, as substantial implications on the resulting formal errors as discussed in Section 5.2.3.

5.2.2. Synthetic Observations

The uncertainty in the dynamics of JUICE is included by using synthetic direct satellite observations which measure the center of the satellite rather than spacecraft. The synthetic direct range, range-rate (Doppler), and VLBI declination and right ascension are denoted by $\tilde{r}_i$, $\tilde{\dot{r}}_i$, $\tilde{\delta}_i$ and $\tilde{\alpha}_i$ respectively. Dirkx et al. (2017) compute the uncertainty of the moon-centered synthetic measurements mentioned above by adding the uncertainty of the position and velocity of the spacecraft with respect to the moon to the uncertainty of the different observation types. This is accomplished by projecting the conditional uncertainty of the spacecraft position with respect to the satellite $\sigma_{\vec{r}^{i}_{sc}}$ into the unit vectors of the range, right ascension and declination denoted by $\hat{\vec{r}}_i$, $\hat{\vec{r}}_\alpha$ and $\hat{\vec{r}}_\delta$ respectively (Dirkx et al. 2017). The equation for these unit vectors is given in Appendix A.4. The result is given in Equations 5.15 to 5.18. Note that the conditional uncertainties are given in the LVLH frame and should be transferred to the inertial reference frame using Equation 3.17. Finally, $|\,|$ denotes the absolute value of the respective vector.

$$\sigma_{\tilde{r}} = \sigma_r + \sigma_{\mathbf{r}^{i}_{sc}} \cdot |\hat{\mathbf{r}}_i| \tag{5.15}$$

$$\sigma_{\tilde{\dot{r}}} = \dot{\sigma}_r + \sigma_{\dot{\mathbf{r}}^{i}_{sc}} \cdot |\hat{\mathbf{r}}_i| \tag{5.16}$$

$$\sigma_{\tilde{\alpha}} = \sigma_\alpha + \frac{\sigma_{\mathbf{r}^{i}_{sc}} \cdot |\hat{\mathbf{r}}_\alpha|}{r_i} \tag{5.17}$$

$$\sigma_{\tilde{\delta}} = \sigma_\delta + \frac{\sigma_{\mathbf{r}^{i}_{sc}} \cdot |\hat{\mathbf{r}}_\delta|}{r_i} \tag{5.18}$$

The measurement uncertainties σ_r, $\dot{\sigma}_r$, and σ_α and σ_δ can be found in Table 4.1. For range and Doppler observations the observational uncertainties are respectively 0.2 m and 0.01 m. For the VLBI uncertainty, different cases are considered. These cases are further discussed in Chapter 6. Typical values for the radial, along-track and cross-track direction uncertainties of $\sigma_{\vec{r}^{i}_{sc}}$ for the different JUICE mission phases are given in Dirkx et al. (2017) and will be further discussed as part of the optimization settings in Chapter 6. Dirkx et al. (2017) have assumed the uncertainties to be constant per mission phase (e.g. GCO500, GEO5000 and the flybys as discussed in Section 2.6.3). The uncertainty $\sigma_{\dot{\vec{r}}^{i}_{sc}}$, to compute $\sigma_{\tilde{\dot{r}}}$, is obtained by scaling $\sigma_{\vec{r}^{i}_{sc}}$ by the characteristic time ΔT. The characteristic time is equal to the tracking arc for the flyby phase and to the orbital period for the orbit phase. Dirkx et al. (2017) use a scaling factor of $\Delta T/4$ and $\Delta T/2$ for the flyby and orbit phase respectively. Subsequently, the position uncertainties are mapped to the velocity uncertainties.

For the flybys, the along- and cross-track position uncertainties $\sigma_{\vec{r}^{i}_{sc}}$ map directly to their corresponding velocities $\sigma_{\dot{\vec{r}}^{i}_{sc}}$ as they are related to the spacecraft orbit around Jupiter. However, the radial position uncertainty is not directly related to the uncertainty in radial velocity as the radial position accuracy is denoted with respect to the satellite of the current flyby, instead of with respect to its central body Jupiter. To this end, Dirkx et al. (2017) proposes to map the root-sum square of the radial and along-track position to the radial velocity uncertainty. This basically denotes how the radial velocity uncertainty is affected by an uncertainty in the along-track direction (i.e. how the uncertainty in the radial direction depends on the uncertainty in the corresponding Jovian orbit). For the orbital tour, the situation is the same except that the radial position uncertainty maps to the along-track velocity. This is a result of the direct coupling between the semi-major axis and the corresponding orbital (along-track) velocity.

The position of the JUICE spacecraft with respect to the body under consideration (a satellite during a flyby, Jupiter in between flybys and Ganymede during the orbital phase) is retrieved from the Consolidated Report on the Mission Analysis (acronym CReMA), version 3.2.[2] As mentioned before, the uncertainty of the orbit determination of the spacecraft is considered in the conditional uncertainty as shown in Equations 5.15 to 5.18.

5.2.3. Realism and Implications of the Adopted Model

As discussed in Section 5.1.2, the a-priori estimate of the observation uncertainties, which assumes the measurements are uncorrelated, as required in the W matrix causes the resulting formal errors of a covariance analysis to be optimistic. For the estimation of planetary ephemerides, the true-to-formal error ratio is typically 2-3 (Jones et al. 2015). Furthermore, as the observational biases (as discussed in Section 5.2.1) are not estimated, the conditional uncertainty (the spacecraft uncertainty given the uncertainty of the moon position) is assumed to be equal to the marginal uncertainty (considering the uncertainty of the position of the moon to which the position of the spacecraft determined). As the conditional uncertainty is generally much smaller than the marginal uncertainty, the resulting true-to-formal error will be higher than 2-3. This should be considered while analyzing the formal errors presented in Chapter 8.

The influence of the model described in Section 5.2.1 on the condition number can divided in two components. First, the projected spacecraft uncertainty (see Equations 5.15 to 5.18), has a substantial influence on the condition number (see also Chapter 8 for a sensitivity analysis). A low spacecraft uncertainty $\sigma_{r_{sc}^i}$ results in a low uncertainty of the synthetic observations. Subsequently, the radiometric tracking observations are assigned a higher weight in the weighting matrix W such that the relative contribution of the optical astrometry (which is necessary to improve the observability of the dynamics of especially Io and to a lesser extend Europa) is reduced. As a consequence, the resulting condition number for a low spacecraft uncertainty $\sigma_{r_{sc}^i}$ will be higher.

Secondly, the bias estimation (as a result of the uncertainty in the position of the moon to which the position of the spacecraft is determined) will have a negligible influence on the condition number of the normal equations matrix. This is related to the fact that the individual biases (per tracking arc and per observation type) are uncorrelated. Therefore, the all rows in the $H^T W H$ matrix associated with the biases will form linearly independent combinations (as the off diagonal entries associated with two biases are zero). Thus the rank (related to the condition number) of the $H^T W H$ matrix being smaller than the number of estimated states is only influenced by the rows associated with the estimated states (row in which the diagonal entry represents the estimated state). The linear dependency of these rows is primarily determined by the observation planning and geometry for the different observation types which directly relates to the observability of the estimated states in the observations. Therefore, the condition number is still primarely governed by the observability of the estimated initial states in the observations.

Note that the focus of this thesis is on the relative contribution of optical astrometry to the stability of the normal equations matrix. Thus, as the condition number is marginally affected by not including the observation biases, the resulting observation epochs will also improve the condition number in case the biases are estimated. Moreover, the improvement of the formal errors should only be interpreted in a relative manner (e.g. that the out-of-plane component of initial state of Io is improved more relative to its in-plane component). Furthermore, the fact that observation biases will be higher for the flyby phase (compared to the orbital phase) will complicate the analysis of the results, as observations related to different phases are affected differently by the observational biases. Therefore, in further studies the biases should be estimated using the optimized observation schedule for the optical astrometry such that a more realistic assessment of the formal errors can be performed.

5.3. Optical JUICE-based Astrometry Weights

The uncertainty of space-based astrometry is described by different models such as those developed by Pasewaldt et al. (2012), Tajeddine et al. (2013), and Duxbury and Callahan (1981). Usually three types of uncertainties are present after astrometric reduction of space-based imagery.

1. The pointing uncertainty σ_p which remains after astrometric calibration using reference stars.

[2] JUICE - Spice “JUICE - Cosmos” cosmos.esa.int `https://www.cosmos.esa.int/web/spice/spice-for-juice` (accessed April 11, 2018)

2. The uncertainty in the limb detection procedure σ_l as well as the uncertainty induced by the errors in the reference ellipsoid σ_m.

3. The spacecraft uncertainty σ_{sp} as a result in the uncertainty in the orbit determination of the spacecraft.

The total uncertainty σ_α and σ_δ can be subsequently determined using Equation 5.19.

$$\sigma_\alpha = \sqrt{\left(\sigma_p^2 + \sigma_l^2 + \sigma_m^2 + \sigma_{sp}^2\right)} / \cos\delta \qquad (5.19)$$
$$\sigma_\delta = \sqrt{\sigma_p^2 + \sigma_l^2 + \sigma_m^2 + \sigma_{sp}^2}$$

It can be noted that the uncertainty of in the right ascension is divided by by $\cos\delta$. This is required to map a uncertainty on a two-dimensional image plane to the celestial sphere, as the uncertainty on a rectangular image is more pronounced close to the celestial poles.

The contribution of the pointing, the limb-fitting, and the spacecraft uncertainty to the total uncertainty is discussed in respectively Section 5.3.1, Section 5.3.2, and Section 5.3.3. Furthermore, as the pointing uncertainty shows a large dependency on the number of background stars, Section 5.3.4 discusses how the number of stars is estimated.

Finally, the uncertainty models discussed in this section are applicable for the Narrow Angle Camera (NAC) of the Cassini spacecraft. Section 5.3.5 discusses the differences in performance of the navigational camera and the JANUS camera with respect to the Cassini Narrow Angle Camera (NAC) and the influence on the resulting uncertainties.

5.3.1. Pointing Uncertainty

As discussed in Section 4.4, each image provided by a space-based camera system is astrometrically calibrated to reduce the pointing uncertainty. In this procedure stars are detected by detecting Gaussian signals for a user-defined full with at half maximum (FWHM).[3] For the Cassini mission, Tajeddine et al. (2013) assumed FWHM = 1.3 pixels. Subsequently, the detected stars are used to fit the direction of the optical axis of the camera α_c and δ_c as well as the camera twist angle θ (see Section 4.4) using a least-squares algorithm. This algorithm reduces the error between the measured and cataloged star positions (after correction for proper motion, abberation, relativistic effects, and the different location of the observer compared to the solar system barycenter).

A realistic uncertainty model, would use the actual camera orientation and determine which stars are in field-of-view such that, among others, the uncertainties in the actual star positions ($\sigma\alpha*$,$\sigma_{\delta*}$) determine the uncertainty in the corresponding σ_p for both the right ascension and declination. However, as there are currently numerous uncertainties in the observation planning (as only the first five JUICE phases are currently segmented[4]) a simplified approach to determine the pointing uncertainty was considered. Nevertheless, such a realistic uncertainty model might be required in further studies in which the absolute uncertainty of the estimated parameters is desired.

The uncertainty in lateral position due to the pointing errors, as a function of the number of stars and the camera properties, is given by Liebe (1995) in Equation 5.20 for a star tracker.

$$\sigma_p = \frac{FOV \cdot \sigma_{extraction}}{N_{pixelsinFOV} \cdot \sqrt{N_{FOV}}} \qquad (5.20)$$

In this equation FOV is the circular field-of-view of the camera, $\sigma_{extraction}$ is the accuracy with which the positions of the stars can be determined in the image and is equal to $\sigma_{extraction} = FWHM/2.355 = 1.3/2.355 \approx 0.55$ pixels (Tajeddine et al. 2013). Furthermore $N_{pixelsinFOV}$ is the number of pixels on the CCD and finally N_{FOV} represents the number of stars that are in field-of-view. This number is a function of, among others, (1) the field-of-view of the camera, (2) the direction of the optical axis in space (i.e.

[3] The width measured along the x-axis between points on the y-axis which are halfway between zero and the maximum amplitude for a Gaussian curve

[4] Vidhya Pallichadath - personal communication

at a low galactic latitude b, which means that the optical axis has a low angle compared to the plane of the Milky Way, note that more stars will be observable than at higher galactic latitudes), (3) the relative size of the observed satellite in the images as the satellite might obstruct a number of stars, and (4) the exposure length of the camera which determines the minimum brightness which a star should have to appear in the image. Section 5.3.4 provides a more elaborate discussion on how the number of stars in field-of-view are estimated.

5.3.2. Fitting Uncertainty

The accuracy with which the center-of-figure of detected limb (as discussed in Section 4.4) can be determined is a function of (1) the phase angle, (2) the proximity of the camera with respect to the targeted moon, and (3) the uncertainty in the reference ellipsoid of the moon that needs to be fitted to the apparent limb. The hybrid limb-fitting uncertainty model, used throughout this thesis, is described at the end of this section.

Phase Angle

In the ideal case the uncertainty with which the center-of-figure of the detected limb is determined would be randomly distributed around zero mean. However, both Tajeddine et al. (2015) and Cooper et al. (2014) show that for the astrometric reduction of the Saturnian moons, using Cassini Narrow Angle Camera (NAC) images, the residuals are distributed in the direction of the Sun. This related to the phase angle which is never exactly zero. Therefore, the detected limbs are always one-sided, which means that the boundary on the dark side of the satellite becomes less sharp, thus increasing the observational uncertainty in the direction of the Sun.

This phenomenon was further investigated by Cooper et al. (2014) by generating artificial images for which the center-of-figure was known beforehand. For phase-angles of 180, 90, and 0 degrees the measured center-of-figure was shifted by respectively 0.75, 0.75, and 0.0 pixels in the direction of the Sun. Note that that for a phase angle of 180 degrees, contrary to the phase angle of 90 degrees, the shift of 0.75 pixels has a part in the the direction of the Sun as well as in the direction orthogonal to the Sun. Antreasian et al. (2008) used a model in which the bias as a result of the phase angle was estimated using $\phi_0 + \phi_1 \sin(\theta/2)$ as part of the orbit determination filter. In this function, θ corresponds to the phase angle and ϕ_0 and ϕ_1 denote the zeroth and first order coefficients.

The biases found in the synthetic images, however, were substantially higher than the actual biases found by Tajeddine et al. (2013) and Cooper et al. (2014), which might be related to the unrealistic representation of the artificial images. Furthermore, Tajeddine et al. (2015) did not show the obvious drift in the direction of the Sun. This can be related to the limb-detection algorithm which was set to a higher sensitivity in case the moon was observed at a high phase angle (and thus a small apparent limb), such that the effect of the phase-angle is considered in determining the center-of-figure of the satellite.

Proximity of the Observed Satellite

Furthermore, next to the phase angle, the uncertainty is a function of the range from which the images are taken. The limb finding error σ_l, as a function of the variable distance at which the moon is observed, is modeled by Antreasian et al. (2005) using Equation 5.21.

$$\sigma_l^2 = \sigma_{min}^2 + (C \cdot d_a)^2 \tag{5.21}$$

In this equation σ_{min} is the minimum weight used for all images which is equal to 0.25 pixels (which is lower compared to the 0.5 pixels used by Tajeddine et al. (2013)). Furthermore, C denotes the apparent diameter scale factor which accounts for the surface roughness in determining the center-of-figure of the limb. For example, for the heavily cratered moon Mimas $C = 0.02$ while for the smoother moons (like Enceladus) $C = 0.01$. Finally, d_a denotes the apparent diameter of the satellite in the image in pixels, which scales with the distance between the spacecraft and the observed satellite.

Uncertainty in the Reference Ellipsoid

Another important source of error in the determination of the center-of-figure is the uncertainty in the model of the reference ellipsoid which has to be fitted on the measured limb (e.g. Tajeddine et al. 2013).

Such a shape model is usually given by the three ellipsoidal radii a, b, and c (see Section 2.4.1). For this study, only the uncertainty in the mean radius was considered for the determination of the uncertainty of the astrometric observations. These uncertainties are presented in Table 3.2. The uncertainties are on the same order of magnitude as the uncertainties for the Saturnian moons as found by Thomas et al. (2007).

For a more accurate representation of the error in the shape model, the unit vector in the direction of the optical axis could be mapped on the vector of the for the three ellipsoidal radii given in an inertial reference frame. This ensures, the uncertainty corresponding the actual observation geometry is considered.

Hybrid Limb Finding Uncertainty Model

As discussed in more detail in Section 5.3.5, the larger field-of-view of the JANUS camera enables the detection of more background stars. Therefore, the pointing error is expected to be less important within the JUICE mission (see Equation 5.20) and consequently, the limb finding error becomes relatively more important. Therefore, assuming the limb detection algorithm to be independent of the phase angle will result in substantially lower uncertainties. This might result in too optimistic condition numbers as there is no dependency on the phase angle and consequently images with close to zero phase (phase angle of $180°$) would receive a too optimistic weight. However, assuming the limb fitting error to be fully dependent on the phase, which is in line with the results from Cooper et al. (2014) obtained using the artificial satellites, would give too much importance to the phase angle in the optimization of the JANUS epochs. More specifically, as the pointing error is less important for the JANUS camera system, a close to zero phase angle would lead to a substantially higher weight such that epochs with a phase angle close to zero will be preferred in the genetic algorithm even though the observability of the dynamics from the observation is not optimal.

Thus, to give more importance to images with a low phase angle (high visible limb) and at the same time gaining more insight into the observational geometry required to reduce the condition number a hybrid method was adopted. This method is based on the function used by Antreasian et al. (2008) to model the phase bias in the orbit determination algorithm. The results from Cooper et al. (2014) show that the observational residual to to the limb finding algorithm is 0.25 pixels in the direction of the Sun (positive line direction, referring to Figure 4.3 and 0.10 pixels in the direction orthogonal to the Sun (negative sample direction). These results are found by averaging the results found for the Saturnian moons Mimas, Enceladus, Dione, Tethys, and Rhea. Therefore, the limb uncertainty is approximated by Equation 5.22. Note that the norm of both components is considered as the actual orientation of the camera is not considered yet such that the sample and line directions cannot be determined yet.

$$\sigma_L = \sqrt{0.1^2 + (0.25\sin(\theta/2)} \tag{5.22}$$

A result of this hybrid approach is that the uncertainty is slightly higher especially for images with a large number of background stars in which the fitting uncertainty dominates the pointing uncertainty. Moreover, note that effect of the proximity of the satellite (considered using Equation 5.21) is not considered in this hybrid approach. This is related to high uncertainty found for close-by images which is substantially higher than the results found by, among others, Tajeddine et al. (2015). Therefore, the total uncertainty is slightly optimistic. In further studies, the apparent scale factor C should be determined based on more recent studies, such that the effect of the variable uncertainty at which the satellites are imaged is also considered. The hybrid approach formulated in this section is validated in Chapter 7.

5.3.3. Spacecraft Position Uncertainty

The final source of error in the lateral positions provided by space-based astrometry are the uncertainties in the spacecraft position. Most of the space-based images will be acquired during the Jovian tour, except for the periods centered 24 hours around the time of closest approach for each flyby. This means that the position of the spacecraft (JUICE) is determined with respect to Jupiter for which the orbit determination accuracy is significantly lower than for the flyby and orbital phases. Tajeddine et al. (2013) assume a position uncertainty of $\sigma_{S/C} = 100$ m for Cassini. This is in line with the results of Antreasian et al. (2008) which show the uncertainty in the radial, along-track, and cross-track direction for the Cassini mission. The upper and lower bounds on these uncertainties are shown in Table 5.1.

Table 5.1: Approximate Cassini spacecraft uncertainties obtained by a visual inspection of Figure 26 of Antreasian et al. (2008) in the radial (R), along-track (A), and cross-track (C) direction during a flyby and at maximum distance from Saturn (d_{max}).

Case	σ_R [m]	σ_A [m]	σ_C [m]
Flyby	1	10	10
d_{max}	20	100	200

These results show that the spacecraft uncertainty varies from its minimum value during a flyby to its maximum in between two flybys. Compared to the spacecraft uncertainties as discussed by Dirkx et al. (2017) for JUICE, the errors in orbit around Saturn are at least a factor 10 higher than the baseline case for the GEO5000 phase. Furthermore, contrary to the analysis by Dirkx et al. (2017), Antreasian et al. (2008) show cross-track errors which are substantially higher than the along-track errors. This difference can be associated to the different viewing geometry during the JUICE mission. As the Cassini spacecraft was equipped with more or less the same tracking system as will be installed on the JUICE mission (coherent multi-link tracking at X- and Ka-band as well as a navigation camera), the presented errors will give a good approximation to the errors which should be expected for JUICE orbit determination.

The influence of the spacecraft uncertainty to the uncertainty in the lateral position of the satellite can be computed using Equation 5.23.

$$\sigma_{sp} = \arcsin\left(\frac{\sigma_{S/C}}{D}\right) \tag{5.23}$$

In this equation D is the distance between the spacecraft and the observed satellite and $\sigma_{S/C}$ the norm of the uncertainty vector as given in Table 5.1.

5.3.4. Estimating the Number of Stars in Field-of-View

The pointing uncertainty as presented in Equation 5.20 is a function of, among others, the number of observed reference stars N_{FoV} which are available for astrometric calibration. As discussed in Section 5.3.1, the number of stars is a function of (1) the field-of-view of the camera, (2) the direction of the optical axis in space, (3) the relative size of the observed satellite in the image, and (4) the exposure length of the camera. The number of stars can be estimated using Equation 5.24, in which number under each term denote which contribution is considered by the respective term.

$$N_{FoV} = \underbrace{2\pi(1-\cos(FoV/2))}_{(1)} \cdot \underbrace{\bar{N}(\delta_c)}_{(2)} \cdot \underbrace{\left(\frac{1}{f_a - a} + b\right)}_{(3)} \cdot \underbrace{n_{visible}}_{(4)} \tag{5.24}$$

In this equation FoV is the field-of-view of the camera, $\bar{N}(\delta_c)$ is the normalized number of stars in a certain latitude band, f_a denotes the fraction of the image (in one dimension) that is filled by the satellite, and $n_{visbile}$ denotes the number of visible stars as a function of the exposure time of the camera.

The normalized number of stars in a certain latitude zone $\bar{N}(\delta_c)$ is given by a piecewise polynomial as a function of the latitude of the optical axis of the camera. This piecewise polynomial is acquired by interpolating the normalized number of stars. The normalized number of stars per latitude zone is calculated by dividing the number of stars in a certain latitude zone (provided in the supplementary information of the UCAC2 catalog[5]) by the projected area of the respective latitude band on the unit sphere. This scaling method accounts for the fact that bands close to the equatorial plane cover a much larger area on the celestial sphere compared to bands close to the celestial poles. In this way images for which the optical axis of the camera points within the Galactic plane, will observe a larger number of stars such that the resulting pointing uncertainty will be lower for these images. Note that a higher number of stars was also found low a low galactic latitude b in the images used by Tajeddine et al. (2015). The results of this analysis can be found in Appendix A.6.

[5]Vizier Database 'UCAC2 Catalogue: I/289' `http://cdsarc.u-strasbg.fr/viz-bin/cat/I/289` (accessed October 8, 2018)

Subsequently, the field-of-view FoV is used to relate the actual number of visible stars by multiplying the normalized number of stars $\bar{N}$ by the area covered by the camera on the unit sphere. Note that the part in Equation 5.24 indicated by (1) represents the area of a spherical cap on the unit sphere.

The influence of the exposure length of the camera is addressed by $n_{visible}(J_{mag-max})$ which denotes the fraction of the stars located in field-of-view that are visible for a given exposure time. The exposure time is related to $J_{mag-max}$ which denotes the apparent magnitude of the faintest star which will be visible in image. The apparent magnitude gives a measure of the brightness of a star as seen from an observer and is an inverse logarithmic relation, meaning that a brighter star has a lower apparent magnitude. The UCAC2 star catalog (Zacharias et al. 2004) gives the apparent magnitude of each star in the J, H, and K band. For this analysis, the J band is used as this band is centered around 1260 nm[6], which is closest to the visible light, in which both JANUS and NavCam operate.

For the images of Tethys and Rhea (which have the closest resemblance to the Galilean moons in terms of size and geometric Albedo as seen in Table A.1 in Appendix A.5), the visible (within field-of-view) reference stars and corresponding magnitude in the J band were determined using the UCAC2 star catalog binary data-files [7]. The binary files were processed using the WCS toolbox.[8] To account for stars which would not be visible due to the occulting target satellite, the stars which are in field-of-view of the camera but behind the satellite were omitted from the list of visible stars. As the number of stars, including relatively faint stars, far exceeds the number of stars found in the images by Tajeddine et al. (2015), the maximum apparent magnitude required to match the number of visible stars was determined for each image. The results of this analysis are shown in Figure 5.1.

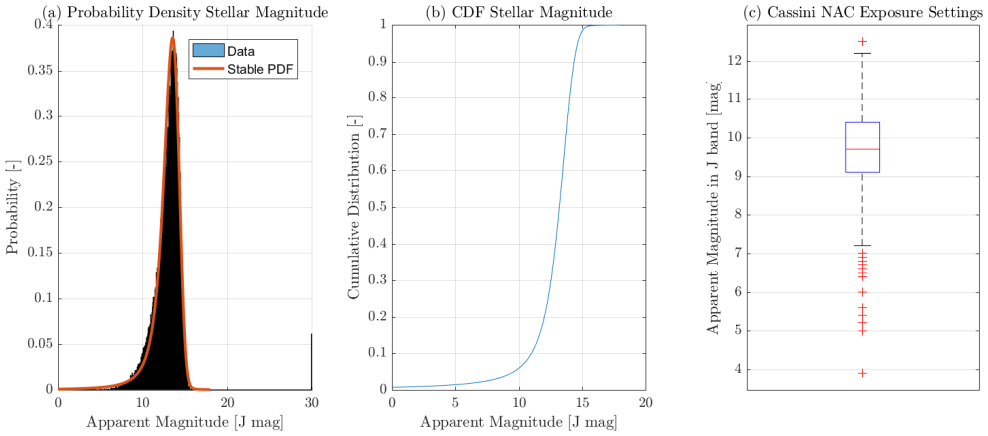

Figure 5.1: Distribution of the magnitude of the stars found on the images of Tajeddine et al. (2013) and Tajeddine et al. (2015) using the UCAC2 star catalog (Zacharias et al. 2004). Figure (a) shows the an histogram which is normalized to show the probability density as well as the probability density function of the fitted Stable distribution. Figure (b) shows the corresponding cumulative distribution function and finally the figure (c) shows the Whisker diagram of the distribution of the maximum apparent brightness per image to match the number of stars found by Tajeddine et al. (2015) with the available stars in the UCAC2 catalog.

Figure 5.1(c) denotes the Whisker diagram of $J_{mag-max}$ required to fit the number of observed stars found in the UCAC2 catalog to the number of stars found by Tajeddine et al. (2015). Furthermore, Figure 5.1(a) denotes the probability density of the apparent magnitude in the J band of all stars found in field-of-view of the images of Tajeddine et al. (2015) (not considering the exposure length) using the UCAC2 star catalog. Subsequently, the Stable distribution (which is suitable for modeling heavy skewness[9]) was fitted through the apparent magnitude of the found stars. Figure 5.1(b) shows the resulting cumulative distribution function (CDF). This CDF was interpolated using a piecewise polynomial providing $n_{visible}(J_{mag-max})$, the fraction of stars visible as function of the maximum apparent magnitude

[6] Astronomical Magnitude Systems 'Astronomical Magnitude Systems' cfa.harvard.edu `https://www.cfa.harvard.edu/~dfabricant/huchra/ay145/mags.html` (accessed October 8, 2018)

[7] Vizier Database 'UCAC2 Catalogue: I/289' `http://cdsarc.u-strasbg.fr/viz-bin/cat/I/289` (accessed October 8, 2018)

[8] WCSTools 'WCSTools: Image World Coordinate System Utilities' tdc-www.hardard.edu `http://tdc-www.harvard.edu/software/wcstools/index.html` (accessed October 8, 2018)

[9] Stable Distribution "Stable Distribution - MATLAB & Simulink - Mathworks Benelux" nl.mathworks.com `https://nl.mathworks.com/help/stats/stable-distribution.html` (accessed October 22, 2018)

of the faintest star visible in the image.

Finally, the number of estimated stars should account for the relative size of the satellite which obstructs a fraction of the image. Tajeddine et al. (2013) showed that the number of stars varied inversely with the relative size of the satellite within the image. Therefore, the last term in Equation 5.24 scales inversely with the fraction of the image which is covered by the satellite. Moreover, $a = 1/2 - \sqrt{5}/2$ and $b = 1 + 1/a$, such that the inverse function is scaled to be 1 when no satellite is present and to be 0 when the satellite is covering the complete image.

5.3.5. Performance Comparison Cassini NAC, JANUS, and NavCam

The performance of space based camera systems regarding the uncertainty in the generated space-based astrometry is determined by the combination of the camera field-of-view and the resolution (the number of pixels on the CCD). This is generally referred to as the angular resolution. Especially for the limb fitting procedure, a low angular resolution is preferred which means errors in the center-of-figure location will result in a smaller angular and thus positional uncertainty. For the pointing uncertainty, however, a large field-of-view in combination with a slightly lower angular resolution might still give a lower pointing uncertainty as the large field-of-view enables the detection of significantly more reference stars.

The Cassini Narrow Angle Camera (NAC) is quite different than both the JANUS and NavCam camera systems on-board the JUICE spacecraft, as its field-of-view is relatively small. The main characteristics for all three camera systems are summarized in Table 5.2.

Table 5.2: Field-of-view and resolution for the Cassini NAC (Tajeddine et al. 2013), JANUS (JUICE Science Study Team 2014), and NavCam (Boutonnet et al. 2018) camera systems.

Camera	Field-of-view [deg]	Resolution [pixels]
Cassini NAC	0.35×0.35	1024×1024
JANUS [10]	$1.72 \times 1.29 \approx 1.49$	$2000 \times 1504 \approx 1734$
NavCam	4×4	1024×1024

Observing Table 5.2, it can be noticed that whereas the resolution is similar for the Cassini NAC and the NavCam, the field-of-view is an order of magnitude larger for the NavCam. Moreover, note that the field-of-view and resolution of the JANUS camera are rectangular. However, for this study, the field-of-view and resolution are assumed to be squared (to ensure Equation 5.20 can be used which assumes a circular field of view). As discussed in Section 5.3.4, pointing errors represent a substantial part of the total uncertainty in the astrometric lateral positions. Therefore, the performance of the different cameras is compared on the attainable pointing uncertainties. To this end, the pointing uncertainty σ_p is plotted for all three cameras using Equation 5.20. The results, including the derivative of the pointing uncertainty $d\sigma_p/dn_{star}$ are presented in Figure 5.2.

The marks in this figure denote the expected number of stars. These are calculated by multiplying the average number of stars found by Tajeddine et al. (2013) and Tajeddine et al. (2015) with the ratio of the area of the projected field-of-view on the unit sphere. The latter can be computed using the equation for the area of a spherical cap for which the angle θ is equal to half the field-of-view as seen in Equation 5.25.

$$A = 2\pi(1 - \cos\theta) \tag{5.25}$$

The average number of stars expected as well as the accompanying pointing uncertainty and its derivative as well as the projected area of the camera on the unit sphere are given for the three camera systems in Table 5.3.

Observing Table 5.3, it can be noticed that the expected pointing uncertainty for the JANUS camera will be almost a factor two smaller compared to the NavCam and NAC camera systems. This is a result of the combination of the higher resolution and the larger field-of-view compared to the Cassini NAC. Furthermore, the sensitivity of the pointing uncertainty as a function of the number of stars is a factor

[10] To simplify the analysis a square field-of-view and resolution are assumed for JANUS. To this end, the field-of-view and resolution are determined by keeping a similar area covered.

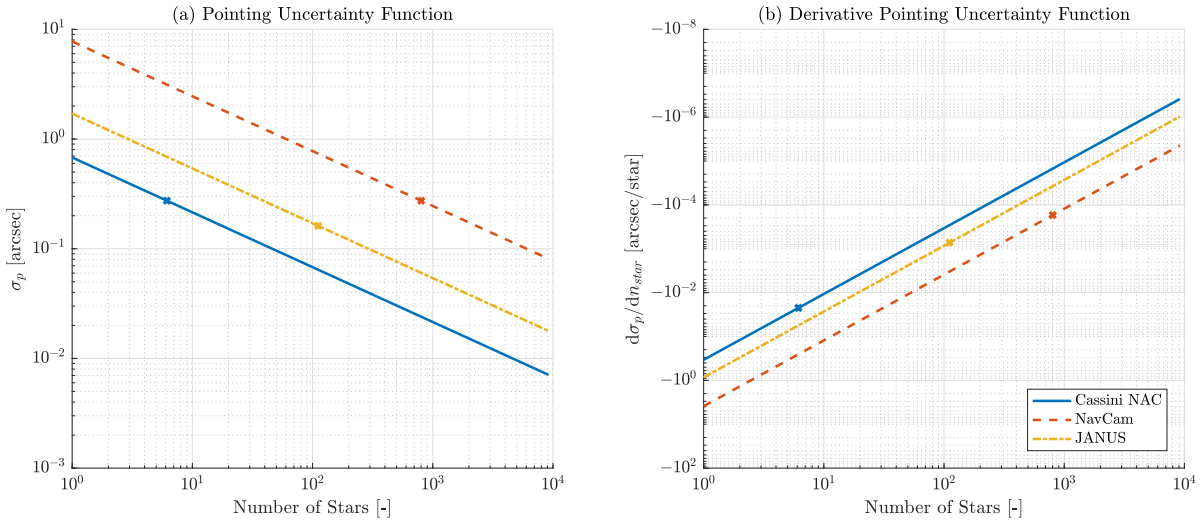

Figure 5.2: Pointing uncertainty (left) and derivative of the pointing uncertainty (right) for the Cassini NAC, JANUS, and NavCam camera systems. The **x**'s denote the expected average number of stars.

Table 5.3: The area on the unit sphere, average number of expected stars and accompanying pointing error and the derivative of the pointing error.

Camera	$A_{sphere-cap}$ $[-]$	N_{FOV} $[-]$	σ_p $[arcsec]$	$d\sigma_p/dn_{star}$ $[arcsec/star]$
Cassini NAC	$2.9308 \cdot 10^{-5}$	6.14	0.2741	$-2.232 \cdot 10^{-2}$
JANUS	$5.3083 \cdot 10^{-4}$	111.2	0.1618	$-7.275 \cdot 10^{-3}$
NavCam	$3.8 \cdot 10^{-3}$	802	0.2741	$-1.709 \cdot 10^{-3}$

three larger for JANUS as the number average stars is substantially larger for JANUS. Finally, NavCam has the same expected pointing error as the Cassini NAC. However, due to the large number of stars in field-of-view, the sensitivity of the pointing error is substantially (more than an order of magnitude) smaller than for the Cassini NavCam. However, besides the pointing errors, the effect of the uncertainty in the determination of the center-of-figure of the limb will be more pronounced for both NavCam and JANUS due to their lower angular resolution compared to Cassini NAC. Moreover, as the both the pointing uncertainty and sensitivity of the pointing uncertainty are substantially lower for the JANUS camera, the limb finding error might be more important for JANUS compared to Cassini NAC. This is pronounced by the fact that the expected pointing uncertainty for JANUS equals 0.05 pixels (by converting 0.1618 arcsec to pixels using the angular resolution) which is only half the minimum limb-finding uncertainty.

6

Optimization Method and Settings

As discussed in Chapter 1, using only radiometric tracking within the context of PRIDE-JUICE yields numerical difficulties as the condition number approaches 10^{16}, such that no significant digits are retained. The problem originates from the poor observability of the dynamics of both Io and Europa in the available observations. The latter is a consequence of the mission geometry and the strong dynamic coupling within the Jovian system. Optimizing the observation schedule for the JANUS camera to be used for optical astrometry was proposed by Dirkx et al. (2017) as a possible mitigation strategy. The definition of the resulting optimization problem is given in Section 6.1. Subsequently, in Section 6.2 different suitable optimization algorithms are discussed and compared after which an algorithm is selected and discussed in more detail. Section 6.3 discusses the implementation of the covariance analysis as discussed in Section 5.1.2 within the optimization framework. The different observational settings/cases to be used in the sensitivity analysis are discussed in Section 6.4. This sensitivity analysis is employed to provide an overview of the consequences of changing the observation settings on the condition number. Finally, the settings used for the optimization are discussed in Section 6.5.

6.1. Optimization Problem Outline

Referring to the research question posed in Chapter 1, the purpose of optimizing the observation schedule of JUICE-based astrometry is to improve the stability and the accuracy of the estimated initial states. Both the stability and the accuracy of the estimated initial states are a function of the observation schedule of the JANUS camera (which will be discussed in more detail in Section 6.3.1). Therefore, the epochs at which a JANUS optical astrometric tracking arc should be initiated are the parameters which are to be optimized.

The optimization of these objectives can be approached in various ways. First of all, a continuous interpretation of time can be used which implies that every epoch (except the epochs for which the operational constraints as discussed in Section 4.7.2 are violated) is available. Alternatively, a discrete time interpretation can be used which greatly reduces the number of available options and consequently reduces the complexity of the optimization problem. As the dynamics of the moons are relatively slow (compared for example to spacecraft in low Earth orbit), small discretization steps (minutes) are expected to have limited influence on the attainable stability and accuracy of the estimated states as the relative geometry does not change significantly in such a time step. This might not be the case during the flybys in which the relative dynamics of JUICE with respect to the targeted moon changes relatively fast. However, Boutonnet et al. (2018) state that optical astrometry within 12 hours of the closest approach is not possible due to operational constraints such that the aforementioned problem is mitigated.

The problem is discretized by evaluating the H matrix at a certain time step (referred to as the discretization step) such that a reduced number of possible options is available for the optimization problem. The discretization step can be adjusted to achieve an optimum between computational effort and the achievable optimum. The advantage of discretization is that the formulation of the operational constraints can be directly considered as part of discretization (i.e. discrete time steps on which the operational constraints are violated are not considered as options for the optimization problem) instead

of formulating them within the framework of the optimization algorithm. Finally, the discrete interpretation of time also has the advantage that the normal equations matrix only needs to be computed once (only at the discrete epochs instead of any epoch which is selected by the optimization algorithm). This significantly reduces the required computation time.

The optimization problem can be approached as a single variable or multivariate optimization problem. In case of the former, only the accuracy of the estimated initial states is optimized. In this approach, the the stability (assessed by the condition number as discussed in Section 5.1.3) should serve as a constraint, rejecting solutions with an condition number lower than a predefined number based on the requested number of significant digits. Alternatively, the problem can be approached as a multivariate optimization problem in which both the stability and accuracy of the estimated initial states are optimized. Such an approach is preferred as it shows the different combinations of both objective parameters located on a Pareto front. Such an approach improves the understanding of the optimized solution. A Pareto-optimal front is a set of solutions which are Pareto-efficient. This means that for each point located on this Pareto-optimal front superiority with respect to another point on the Pareto-optimal front cannot be established considering both objectives (Deb 2001). Translated to the problem at hand, the Pareto-front will be a distribution of points with with an combination of an optimal condition number (assessing the stability) and accuracy (low uncertainty of the estimated initial states), where no point is superior compared to the other points on the Pareto front. The optimization problem is now concisely formulated below.

$$\text{minimize } (\kappa(H^T W H), \sigma_{r_{Io}})$$
$$\text{where } H = f(t_{JANUS}),\ W = g(t_{JANUS}),\ P = (H^T W H)^{-1},\ \sigma_{r_{Io}} = \sqrt{P_{11} + P_{22} + P_{33}}$$
$$\text{where } t_{JANUS} = (t_{11}, t_{12}, ..., t_{mn})$$
$$\text{subject to}$$
$$1.\ t_{JANUS} \in T_{available}$$
$$2.\ m = m_{max}$$
$$3.\ n = n_{max}$$
$$4.\ t_{mn} - t_{m(n-1)} = T_{discretization}$$

In this formulation both the condition number $\kappa(H^T W H)$ and the root-sum-squared of the formal error of Io ($\sigma_{r_{Io}}$) are the objectives to improve the stability and the accuracy of the estimated initial conditions. The root-sum-squared of the formal error of Io (which is acquired by taking the square root of the sum of the first three entries of the covariance matrix P) is used to assess the fitness of the covariance matrix. This approach is supported by the (large) difference between the formal errors acquired for Io and Europa provided by Dirkx et al. (2017) in which the in-plane formal and out-of-plane formal error of Io are respectively 1.6 and 4.5 times as high compared to the formal errors of Europa. Note these ratios are acquired for the baseline case presented in Dirkx et al. (2017) and a VLBI measurement accuracy of $\sigma_{VBLI} = 0.5$ nrad (which is used as a baseline throughout this thesis which will be discussed in Section 6.4.5).

In this formulation the partial derivative matrix H and the weighting matrix W are related to the epochs at which a JANUS tracking arc it initiated by the functions f and g. These functions are visualized in Section 6.3.1 and 6.3.2. Furthermore, the epochs at which a JANUS tracking arc should be initiated should be in the domain of the discretized time intervals on which the operational constrains (as discussed in Section 4.7.2) are satisfied. Furthermore, the number of tracking arcs should be equal to m_{max} and the number of images per tracking arc should be equal to n_{max}. Finally the time-step between two adjacent images during a tracking arc is equal to the discretization step $T_{discretization}$.

6.2. Optimization Algorithm

Different optimization algorithms are available to solve the optimization problem as defined in the previous section. Section 6.2.1 discusses the considerations regarding the selection of the optimization algorithm as well as the actual selection. Furthermore, Section 6.2.2 discusses the working principle

of the considered optimization algorithm.

6.2.1. Classification of the Optimization Problem

The optimization problem as defined in Section 6.1 belongs to the class of multi-objective combinatorial optimization. Coello et al. (2010) defines a combinatorial optimization problem as " *a finite set of discrete solution $\mathcal{D}$ and an objective function f that associates each solution a value that represents its quality*". In this case t_{JANUS} is a possible discrete solution and the quality is represented by both $\kappa(H^T W H)$ and $\sigma_{r_{Io}}$ (the norm of the formal error of the position of Io) to which t_{JANUS} is mapped by the functions f and g. An overview of different available algorithms within the category of multi-objective combinatorial optimization is given by Coello et al. (2010).

These algorithms are limited to the category of meta-heuristics. Heuristics is a systematic method to find a good solution based on a relatively simple idea (Halim and Ismail 2017) where meta-heuristics are further developed heuristics which utilize a more abstract idea (e.g. Weise 2009). As most Multi-Objective Combinatorial Optimization Problems (MOCOP) are $\mathcal{NP}$ hard[1] approximate methods (such as meta-heuristics) are most commonly used. Furthermore, Coello et al. (2010) state that medium and large size MOCOP problems require meta-heuristics as exact methods (with a guaranteed quality) are limited to problems having only two objectives. For the problem as defined in Section 6.1, there is no analytic relation between the variable to be optimized and the optimization variables. This is the result of the discretization and the approach in which the information matrix is evaluated once to reduce the computation time significantly. Therefore, exact methods are not suitable and meta-heuristics are required to find an optimum for the posed optimization problem.

According to Coello et al. (2010) the Non Dominated Sorting Genetic Algorithm II (NSGA-II) is one of the most commonly used multi-objective evolutionary algorithms in current literature. Furthermore, a study by Deb et al. (2002) in which the simulation results of the NSGA-II on a few test problems were compared to other multi-objective optimization algorithms, showed that much better performance was observed for NSGA-II. The other algorithms included Pareto-archived evolution strategy (PEAS) and strength-Pareto Evolutionary Algorithm (SPEA). There are, however, studies in which the NSGA-II algorithm is outperformed by other algorithms. For example, Li and Zhang (2009) show that the NSGA-II is outperformed by the MOEA/D algorithm. However, as the NSGA-II algorithm is readily available in most programming languages and is commonly used for many multi-objective optimization problems, this algorithm is chosen to solve the posed optimization problem. Note that this trade-off between different meta-heuristic optimization algorithms is not exhaustive and further research into different optimization algorithms might be required. However, for the Pareto optimum solutions a clear physical signature was found in the resulting parameter space (which will be discussed in Chapter 8). Moreover, the optimization time using the number of generations and the population size as will be discussed in Section 6.5 is on the order of 1 day. Therefore, the performance (in terms of the optimal solution and computation time) of the NSGA-II algorithm is sufficient for the purpose of this thesis. Nevertheless, different optimization algorithms might reduce the required computation time and thus allow more different cases to be analyzed. This, however, is left as a recommendation for further studies.

During the course of this thesis the Pareto search algorithm was implemented in MATLAB. This algorithm uses a pattern search to find non dominated solutions. The Pareto search is compared to the NSGA-II algorithm for the design of a welded beam in the MATLAB documentation.[2] This test problem is used for various multi-objective algorithms, for example by Deb (2001). For a typical problem without non-linear constraints (which is the case for the optimization problem as posed in Section 6.1), the Pareto search algorithm is at least as accurate as the NSGA-II algorithm but requires many fewer function evaluations, thus reducing the computation time. This might be beneficial in case the observation biases are estimated. Nevertheless, the signature of the Pareto optimal parameter space is not expected to change substantially in case the observation biases are estimated, thus reducing the need for a substantially faster optimization algorithm.

[1] "*A problem is $\mathcal{NP}$ hard if an algorithm for solving it can be translated into one for solving any $\mathcal{NP}$ problem (nondeterministic polynomial time) problem. $\mathcal{NP}$-hard therefore means "at least as hard as any $\mathcal{NP}$," although it might, in fact, be harder.* - Wolfram MathWorld "NP-hard Problem – from Wolfram MathWorld" mathworld.wolfram.com `http://mathworld.wolfram.com/NP-HardProblem.html` (accessed October 10, 2018)

[2] Design Optimization of a Welded Beam - MATLAB & Simulink - Mathworks Benelux nl.mathworks.com `https://nl.mathworks.com/help/gads/multiobjective-optimization-welded-beam.html` (accessed November 7, 2018)

6.2.2. Multi-Objective Genetic Algorithm NSGA-II

The working principle of the Non-Dominated Sorting Genetic Algorithm (NSGA-II) is illustrated in Figure 6.1. Figure 6.1(a) is inspired on the work of Wang et al. (2015) and Figure 6.1(b) is inspired on the work of Deb (2001).

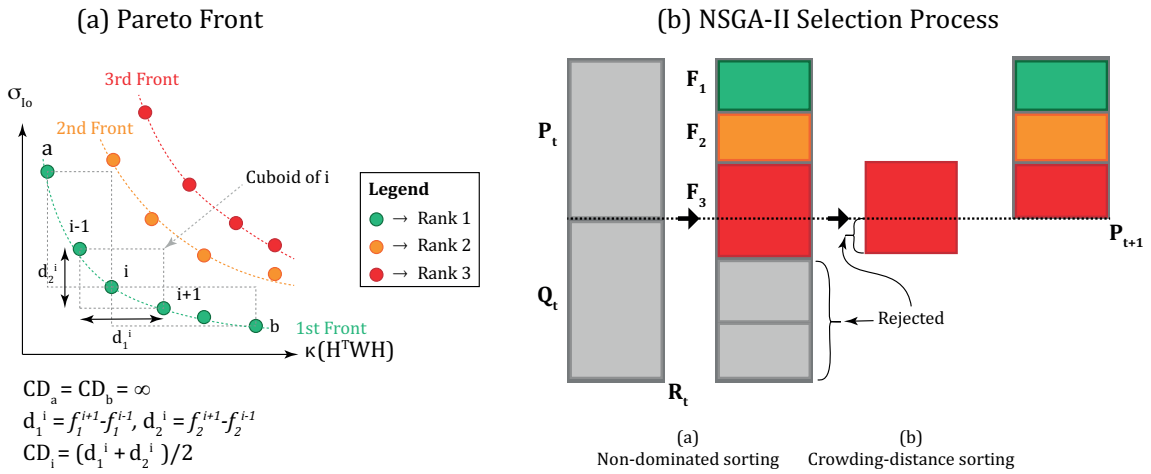

Figure 6.1: Schematic figure illustrating the working principle of the NSGA-II algorithm. Figure (a) shows the different fronts which are present within the population as well how the crowding distance is computed for a point located on the first front. Figure (b) shows the selection process within the NSGA-II algorithm.

The Non-Dominated Sorting Genetic Algorithm (NSGA-II) is a genetic algorithm that not only uses an elite-preservation approach (step (a) in Figure 6.1(b)) but also uses an explicit diversity-preserving algorithm (step (b) in Figure 6.1(b)). In an elitist genetic algorithm the individuals with the highest fitness or rank (among the parent P_t and offspring population Q_t as shown in Figure 6.1(b)) are selected for the next generation (e.g. Deb 2001).

In a controlled elitist genetic algorithm on the other hand, not only individuals with a high fitness value are favored, but also individuals which maintain the diversity of the population. This is accomplished by assigning each individual of the parent Q_t and offspring population Q_t with both a non-domination rank (i.e. the number on the front with non-dominated individuals on which the specific individual is located as shown in Figure 6.1(a)) and a crowing distance CD_i which is calculated as the average of the crowding distances d_j^i (where $j = 1 \ldots r$) of r objectives (as shown in Figure 6.1(a)). The latter is a measure of the search space surrounding individual i which is not populated by another individual in the parent or offspring population (Deb 2001). This search space is visualized in Figure 6.1(a) by the cuboid of i.

The total population (both P_t and Q_t) equals $2N$ while there are only N available places in the next generation P_{t+1}. Therefore, not all individuals can proceed to the next generation. To this end, the non-dominated fronts with the highest rank (F_1, F_2, and F_3 in Figure 6.1(b)) are selected until the next generation P_{t+1} is populated. On the last front F_3, however, there are more individuals (having a similar rank) than there are available slots on P_{t+1}. To this end, the individuals with the highest crowding distance CD_i (i.e. located in the least crowded region) are chosen for the next population. This principle is especially useful during later generations when many individuals (more than N) are on the first non-dominated front. The diversity-preserving algorithm thus ensures the solution will have a better spread among the solution when the entire population is located on the Pareto-optimal front (Deb 2001). The NSGA-II algorithm stops when the entire population has moved towards the Pareto optimal front and the movement of the Pareto-optimal front is small.

6.3. Implementation of Estimation Framework

This section discusses the implementation of the covariance analysis within the optimization framework. Therefore Section 6.3.1 shows how the information matrix and weight vector are processed and how both the condition number and the root-sum-squared position formal error of Io are a function of t_{JANUS}.

Subsequently, Section 6.3.2 discusses multiple methods that are used to select t_{JANUS} as defined in Section 6.3.1.

6.3.1. Computing Condition Number and Formal Error

As discussed in Section 6.1, both the condition number and the formal error of the position of Io (which are to be optimized) are a function of the JANUS epochs only within the optimization framework. This is illustrated in five steps in Figure 6.2 which are subsequently discussed. Note that Figure 6.2 and 6.3 show how the functions f and g that relate t_{JANUS} to both H and W.

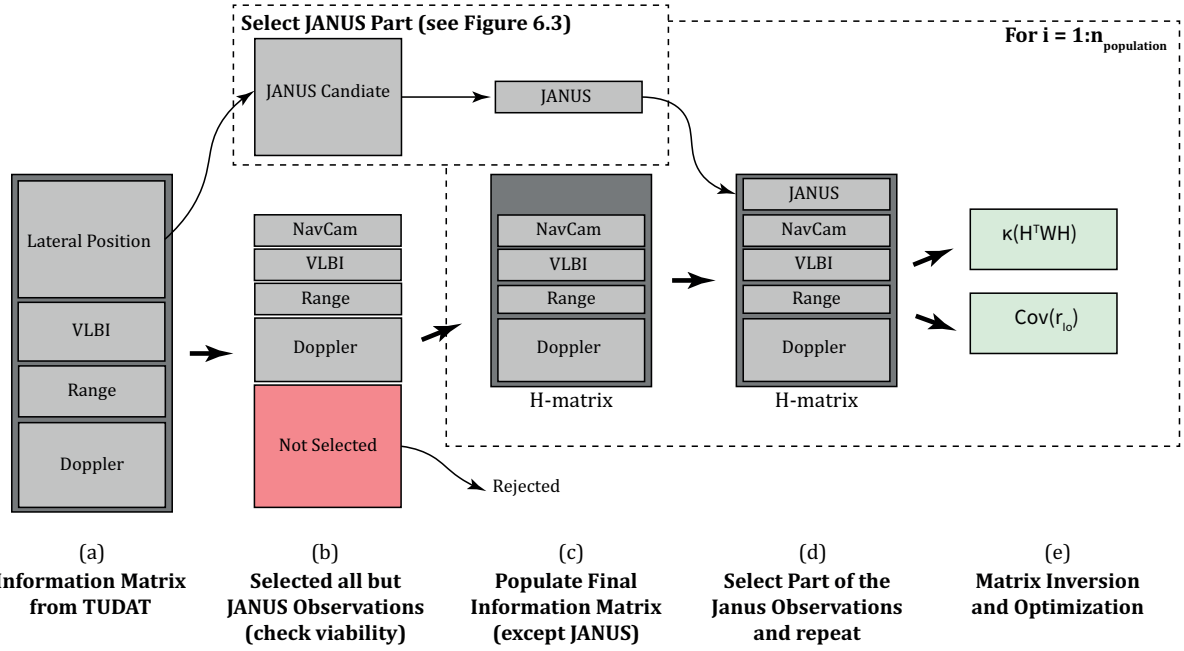

Figure 6.2: Schematic figure illustrating how the JANUS epochs are optimized. Note that the selection of the JANUS observations is discussed in more detail in Section 6.3.2.

(a) An information matrix containing 4 observation types is generated using the Tudat software toolkit.[3] Note that for all the observation types, more observations are generated than required (notice that the information matrix from TUDAT is larger than the selected observation matrix in Figure 6.2(d)), such that the observation settings regarding observation cadences can be applied afterwards. For the lateral position observable, an observation is generated with a discretization step of 120 seconds.[4] This is close to the average step between two adjacent observations found using the data from Tajeddine et al. (2013) and Tajeddine et al. (2015). The radiometric tracking observables (VLBI, range, and Doppler) are generated for a period of 8 hours centered at all the flybys with a cadence as given in Table 4.1. Furthermore, all radiometric tracking observables are generated for the complete orbital phase, with the same cadence as for the flyby phase. Note that the Tudat software already considers the viability of the observations as considered in Section 4.7.1 (occultations and Solar Corona avoidance) such that only viable observations are included in the observation matrix. This is, however, not true for the operational constraints as discussed in Section 4.7.2 (e.g. maximum fraction of image filled by the moon).

(b) The observation settings for the current case (see Section 6.4 for an overview of all cases which are considered) are used to determine which observations are selected to populate the actual

[3] TU Delft Astrodynamic Toolbox documentation `http://tudat.tudelft.nl/` available at `https://github.com/Tudat` (accessed October 13, 2018)

[4] Smaller steps were not possible on an 8 GB RAM virtual machine as the size of the total number of variables required per epoch (information matrix and state vectors to compute the conditional uncertainty is shown in Section 5.2) exceeded the amount of available memory. The allocation of memory could, however, be further optimized such that lower discretization steps are attainable. However, due to the slow dynamics as discussed in Section 6.1 the improvement is expected to be neglible.

information matrix. Note that the NavCam observations are generated from the same part of the original information matrix as the JANUS observations. However the different weights used in the final information matrix inversion ensures both observations are from a different type. Before the lateral position observations are used as either JANUS or NavCam observations their viability is considered using the operational requirements as discussed in Section 4.7.2. The NavCam observations are selected from the viable lateral position block and the options for the JANUS astrometry are kept separate in a JANUS candidate observation block. The observations which are not used for this particular observation settings are rejected.

(c) The final information matrix is constructed and populated with all observation types except the JANUS astrometry. This leaves an empty place in the final information matrix.

(d) The indices of the JANUS candidate matrix which will populate the final information matrix are determined by NSGA-II algorithm. The selection method will be discussed in Section 6.3.2.

(e) The weighting matrix W is constructed for the all possible observations considering the selected observation settings (such as the VBLI uncertainty σ_{VLBI}) and using the methods described in Chapter 5 to evaluate the measurement uncertainty per observation. The requested part of the W matrix is selected using a similar method used to select the H matrix. Subsequently, both the condition number $\kappa(H^T W H)$ and the root-sum-squared of the position of Io $\sigma_{r_{Io}}$ (via the covariance matrix $P = (H^T W H)^{-1}$) are evaluated.

The procedure described in this section is repeated for every individual in population R_T (see Figure 6.1). Subsequently, $\kappa(H^T W H)$ and $\sigma_{r_{Io}}$ are used to assess the fitness of each individual such that the individuals that will populate the next generation P_{t+1} are selected. This procedure is repeated until the predefined number of generations is reached. The latter will be discussed in Section 6.5.

6.3.2. Selecting the Indices of the JANUS Candidate Matrix

This section discusses the details of the selection procedure of the JANUS observations as required in Figure 6.2(d). The selection procedure is schematically illustrated in four steps (a) to (d) in Figure 6.3. First the general selection procedure (applicable to the optimization problem sketched in Section 6.1) after which a slightly different approach is discussed which is to be used within the sensitivity analysis.

General JANUS Selection Procedure

(a) The NSGA-II algorithm selects m epochs for which a JANUS tracking arc should be initiated. These m options can be selected out of a total of N options which are sorted per phase (Flyby, GEO5000, and GCO500) and target body (Io or Europa) such a certain distribution of observations among the different phases can be chosen. Thus, in fact, the NSGA-II algorithm optimizes the indices of the JANUS option vector shown in Figure 6.3(a). As the parameter to be optimized is an integer, an optimization algorithm should be used which can handle integer variables. Note that when using a regular genetic algorithm, using real coding after which the optimized parameters are rounded, has poor performance. Therefore, the NGPM algorithm[5] was used, which is an implementation of the NSGA-II algorithm which supports integer coding. Furthermore, for an integer algorithm the mutation rate should be reduced to increase the effectiveness of the algorithm. Therefore, the crossover fraction was set at 0.9.[6]

(b) Each entry in the $(N \times 1)$ JANUS option matrix corresponds to two entries in the JANUS candidate matrix $(2N \times 24)$ as one astrometric image provides both the right ascension α and declination δ of the moon under consideration. Therefore, each selected epoch is mapped to the corresponding entry of the JANUS candidate matrix by $i_{candidate} = 2i_{option} - 1$. The -1 is required to make sure the tracking arc is initiated with a right ascension observation.

[5] Mathworks File Exchange "NGPM – A NSGA-II Progam in Matlab v1.4 - File Exchange - MATLAB Central" nl.mathworks.com https://nl.mathworks.com/matlabcentral/fileexchange/31166-ngpm-a-nsga-ii-program-in-matlab-v1-4 (accessed September 9, 2018)

[6] Mixed Integer Optimization "Mixed Integer Optimization - MATLAB & Simulink - MathWorks Benelux" nl.mathworks.com https://nl.mathworks.com/help/gads/mixed-integer-optimization.html (accessed October 22, 2018)

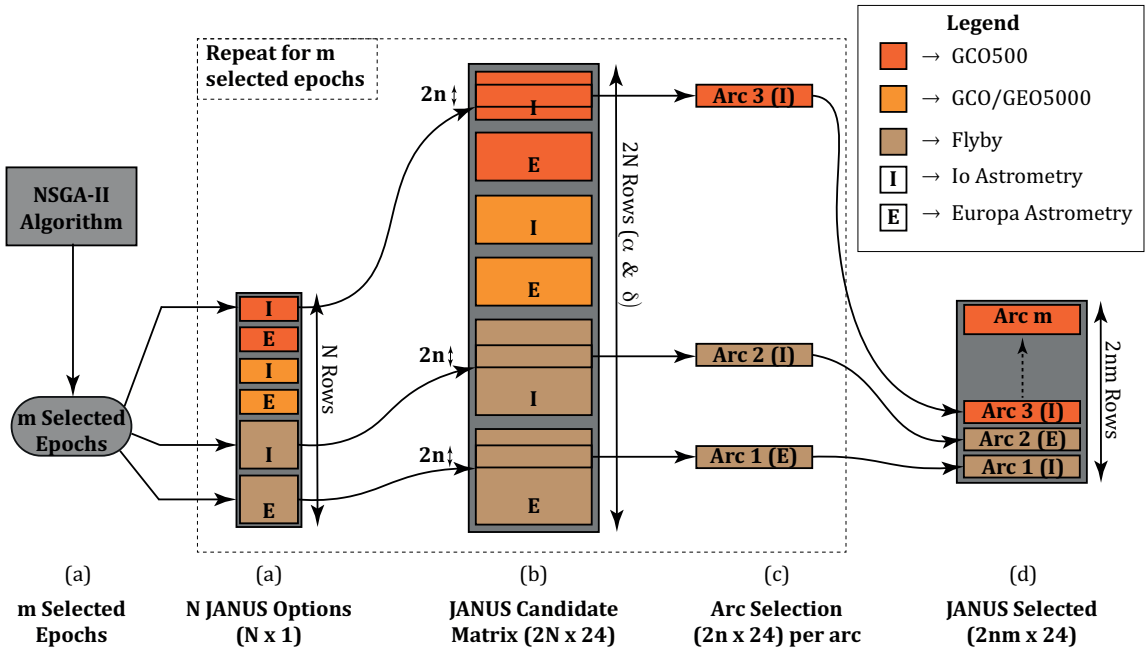

Figure 6.3: Schematic figure illustrating how the NSGA-II algorithm selects the JANUS observations for each individual in the population. Note that the number of estimated variables (the intial states of the four Galilean moons) is equal to 24.

(c) The $2n$ adjacent rows to $i_{candidate}$ in the direction of incremental time are selected to complete the tracking arc with length n for both the α and δ observations. In this way a total of m arcs containing $2n$ rows and 24 columns (representing the four initial states of the Galilean moons) are selected.

(d) The selected arcs will populate the empty selected JANUS matrix with a total of $2nm$ rows and 24 columns. This matrix will subsequently be used to populate the total information matrix (or partial derivative matrix) as shown in Figure 6.2(d).

Selection Procedure for the Sensitivity Analysis

For the sensitivity analysis (as described in Section 6.5) a slightly different method is used to select the JANUS observations compared to the method sketched in Figure 6.3. This is related to the large number of cases that needs to be evaluated for the sensitivity analysis. Determining the optimum observation settings t_{JANUS} for this large number of cases requires an enormous amount of computation time. Therefore, assumptions should be made to estimate suitable epochs for JANUS astrometry. As the instability of the estimation of the initial states is mostly related to the poor observability of the dynamics of Io in the observations, choosing epochs at which the root-sum-squared of the partial derivative of the observation vector which respect the position of Io are high would potentially increase the number of linear independent combination in the normal equations matrix H. However, due to the dynamic coupling through the Laplace resonance, it is difficult to decorrelate the dynamical behavior of Io from the dynamics of the other moons. Therefore, observing during a conjunction would be beneficial as such an observation will also have a higher partial derivive of either Europa or Ganymede (depending on the type of conjunction) and will therefore facilitate the decorrelation between the dynamics of the different moons. Thus, for the sensitivity analysis, m epochs are selected based on the aforementioned criteria replacing step (a) in Figure 6.3.

Note, however, an analysis of the optimized observation epochs showed that the distance between JUICE and the target moon is more important. Therefore, the approach of selecting the JANUS observations for the sensitivity analysis should be revisited in further studies. Nevertheless, the sensitivity provides relative trends on the stability of the solution as a result of varying observation settings. However, the sensitivity analysis should not be interpreted in an absolute manner.

6.4. Optimization Cases

There are various observation settings which may influence both the attainable condition number and the formal errors. The different settings for all assessed observation cases are discussed in this section. First of all, the JUICE orbit determination accuracy is discussed in Section 6.4.1, after which the both VLBI observation uncertainty and cadence are discussed in Section 6.4.2. The NavCam and JANUS settings are discussed in Section 6.4.3 and 6.4.4 respectively. To make sure only one independent variable at a time, a baseline case is defined in Section 6.4.5 such that the variables which are not assessed have a predefined value.

6.4.1. JUICE Orbit Determination Uncertainty

As discussed in Section 4.2 the orbit determination of JUICE is decoupled from the estimation of the ephemerides of the Galilean satellites. The uncertainty in the spacecraft orbit determination is thereby parametrically included by projecting the spacecraft uncertainty to the observation vector as discussed in Section 5.2. To assess the influence of the orbit determination errors on the condition number, different uncertainty cases were considered. Those cases are similar to the cases used in Dirkx et al. (2017) except that an additional phase is added with different uncertainty values. This is due to the fact that most of the JUICE-based astrometry is performed in between different flybys when the spacecraft is in orbit around Jupiter. As already discussed in Section 5.3.3, the accuracy with which the orbit of the spacecraft can be determined is substantially lower in between two flybys compared to the attainable uncertainty values during the flybys. Therefore this additional case is considered in studying the influence of space-based astrometry in optimizing the attainable condition number and formal errors. The different JUICE uncertainties per mission phase can be found in Table 6.1. Note that the cross-track uncertainty during a Jovian orbit is lower than the value presented in Table 5.1.

Table 6.1: Conditional (ephemerides of the moon are fixed) JUICE spacecraft position uncertainties in the Radial (R), along-track (A), and cross-track (C) direction during the different mission phases. Conditional uncertainties from the first three phases are from Dirkx et al. (2017). The conditional uncertainties of the Jovian orbit are a factor 10 higher than the uncertainties for the GCO/GEO5000 phase.

	GCO500 [m]			GCO/GEO5000 [m]			Flybys [m]			Jovian Orbit [m]		
Case	R	A	C	R	A	C	R	A	C	R	A	C
1	0.2	2	1	1	5	2	1	10	10	10	50	20
2	0.5	2	1	2	5	2	2	10	10	20	50	20
3	0.5	2	2	2	10	2	2	20	10	20	100	20
4	0.5	5	2	2	10	5	2	20	20	20	100	50
5	1	10	5	5	20	10	5	50	50	50	200	100

It can be seen in the table above that the uncertainty is minimal for the GCO500 phase and maximum for the Jovian tour (except the flybys). Furthermore, it can be seen that the uncertainties for the Jovian tour, rather than being compliant with the values as presented in Section 5.3.3, are a factor 10 higher than the uncertainties for the GCO/GEO5000 phase. For the case 4, both the radial and along-track component are compliant with the values as presented in Section 5.3.3. However, the cross-track uncertainty is substantially lower. This might be attributed to a different viewing geometry during the Cassini mission compared to the JUICE mission. Nevertheless, as the spacecraft position uncertainty is generally two orders of magnitude smaller than the limb-fitting uncertainty of the center-of-figure of the moon, this difference is expected to have a limited consequence.

The uncertainties as presented in Table 6.1 were validated by Dirkx et al. (2017) using the *Orbit14* software. They found that the uncertainties belonging to case 1 were a good approximation to the simulated position formal uncertainties for both the GCO500 and GCO/GEO5000 phases. It should, however, be noted that the true errors will be higher than the formal errors. For tracking of planetary spacecraft the true error is usually a factor 5-10 higher than the simulated formal errors (Dirkx et al. 2017). However, as discussed by Dirkx et al. (2017), the use of a dual-band tracking system (see Section 4.6.2) might limit the effect compared to current and previous missions. The uncertainties presented in Table 6.1 for case 5 were considered to be too pessimistic. For the flybys, different

results were found by Dirkx et al. (2017). Especially for the Europa flybys, the formal uncertainties were substantially better than the uncertainties presented in case 1. For the Callisto and Ganymede flybys, half of the flybys were accurately represented by the case 1 uncertainties while for the other half cross-track error were found which were substantially higher. The latter was attributed to the edge-on viewing geometry for these flybys. This limits the effectiveness of Doppler tracking in determining the cross-track dynamics. Finally, the ratio between position and velocity uncertainty as presented by Dirkx et al. (2017) and discussed in Section 5.2 was found to be within 10-20 % of the approximated spacecraft velocity uncertainties as found using the *Orbit14* software. It should, however, be noted that the validation results are relatively sensitive to precise JUICE trajectory. The results as presented in Dirkx et al. (2017) were found using the CReMA 2.0 trajectory, while this study uses the CReMA 3.2 trajectory.

The CReMA 2.0 trajectory represents study trajectory 140, while the CReMA 3.2 trajectory represents consolidated study trajectory 141a.[7] Both trajectories have similar mission phase (Boutonnet and Varga 2017; Grasset et al. 2013), however, the actual sequence of flybys is substantially different. For example, the CReMA 2.0 trajectory has a longer energy reduction phase (phase 2 in Table 2.2) such that the Europa science phase (phase 3 in Table 2.2) is approximately 5 months later. Furthermore, for the CReMA 2.0 trajectory, the Europa flybys are initiated and terminated by two Callisto flybys. For the CReMA 3.2 trajectory, however, the Europa flybys are initiated by a Ganymede flyby. The latter may have a substantial impact on the results presented in this thesis in Chapter 8 as this directly influences the proximity of Io during the flybys. Thus affecting the effectiveness of JANUS optical astrometry of Io during these flybys.

6.4.2. VLBI Measurement Uncertainty & Observation Schedule

As shown by Dirkx et al. (2017), the different VLBI measurement uncertainties had a clear signature on the attainable formal errors. This effect was especially pronounced for the out-of-plane formal errors, which can be explained by the fact that this component is only weakly constrained by the 3GM tracking data. Contrary to Europa and Ganymede the improvement of VLBI uncertainty also substantially improves the in-plane formal error of Callisto. Next to the variation of the VLBI uncertainty, the VLBI observation cadence has a substantial influence on the attainable errors. As a VLBI tracking campaign requires a considerable number of resources, the number of tracking arcs should be minimized. To this end, the different VLBI tracking cadence schemes are considered. The different VLBI tracking cadence schemes can be found in Table 6.2.

Table 6.2: List of VLBI observation settings (Dirkx et al. 2017).

Case	VLBI Cadence (Ganymede (orbit) phase)	VLBI cadence (flybys)	σ_{VLBI} [nrad]
1	Once per week	Every flyby	1.0
2	Once per month	Every 2nd flyby (per moon)	0.5
3	Once per 3 months	Every 3rd flyby (per moon)	0.1
4	None	Every 2nd flyby/ None (Callisto)	n/a
5	n/a	Every 2nd flyby/ None (Europa)	n/a
6	n/a	Every 2nd flyby/ None (Ganymede)	n/a

Note that the sensitivity of the VLBI uncertainty is assessed because potential improvement of the VLBI observational uncertainty by adopting a Ka-band tracking system as discussed in Section 4.6.2. Therefore, it is important to determine the relative contribution of an improved observation uncertainty such that different scenarios are evaluated and can be compared.

6.4.3. NavCam Operations

According to Boutonnet et al. (2018), the NavCam is not intended to be used for Io astrometry. This as Io astrometry is not functional in the orbit determination of JUICE. However, using the NavCam camera

[7] JUICE - Spice “JUICE - Cosmos” cosmos.esa.int `https://www.cosmos.esa.int/web/spice/spice-for-juice` (accessed April 11, 2018)

has some advantages with respect to the JANUS camera. First of all, its large field-of-view enables more stars to be detected which will reduce the uncertainties in the obtained lateral position. This advantage, however, might be might be canceled due to the low angular resolution (see Section 5.3.5 for a more detailed assesment of the performance of both JANUS and NavCam compared to the Cassini NAC). Nevertheless, its low resolution compared to JANUS (roughly 1 megapixels for NavCam compared to 3 megapixels for JANUS), will substantially reduce the required data volume, which increases the operational flexibility. To assess the relative influence of the NavCam, similar as for VLBI, different observation cases are considered.

First of all, to assess the influence of the number of images acquired, either three or six images are considered for every observation epoch, as Antreasian et al. (2005) state that for the Cassini mission, three to six optical navigation images were acquired every day by the Cassini NAC (Narrow Angle Camera). More images in one sequence may have the potential benefit that especially the dynamical behavior is better constrained compared to one individual image. A possible downside, however, is that the measurement uncertainty during a sequence of observations is biased (e.g. in the direction of the Sun). This is, however, especially true for the spacecraft uncertainty, which only has a limited contribution to the total error budget of the space-based optical astronomy. The different observation settings can be found in Table 6.3.

Table 6.3: Observation cases for NavCam astrometry.

Case	NavCam Cadence	Images per Observation Epoch
1	None	3
2	Every 12 hours	6
3	Every 2 days	n/a

Note that because of the operational constraints as discussed in Section 4.7.2, the considered baseline observation cadence (once every 12 hours) is not always attainable. This is especially true for Io with a limited distance to Jupiter. Therefore Jupiter will be in field-of-view of the image at relatively close distances with respect to Jupiter. The latter may complicate the astrometric reduction of the image both due to absence of background stars (due to the relatively bright Jupiter) and the presence of Jupiter. The observation cadences are chosen as Boutonnet et al. (2018) state that the NavCam will acquire images for optical navigation roughly every 12 hours. Furthermore, as the priority order for the three relevant moons is Ganymede, Callisto, Europa and multiple moons can be observed during one epoch, one Io observation epoch every 2 days (four times the nominal observation cadence) would be a realistic first order estimate. However, more cases are considered to assess the potential benefit of adding more NavCam observations of Io.

6.4.4. JANUS Operations

There are various parameters that may influence the performance of the JANUS camera in reducing the instability of the normal equations. As discussed in Section 5.3, the exposure length, the number of pixels as well as the uncertainty of the fitted limb in the direction of the Sun all determine the uncertainty of space-based astrometry. To this end, different cases are considered for JANUS which are summarized in Table 6.4.

For the resolution, 1/4 full resolution means that a resolution of 1024×1024 becomes 256×256. Furthermore, the exposure time is modeled by the maximum apparent stellar magnitude (note that the apparent magnitude has an inverse logarithmic scale). The five values correspond to five-number summary of the Whisker diagram as shown in Figure 5.1. This Whisker diagram uses the range of upper values for the stellar magnitude that is required to fit the available number of stars in the UCAC2 catalog to the number of stars found by Tajeddine et al. (2013) and Tajeddine et al. (2015) using the WCS toolbox (Zacharias et al. 2004) (see Section 5.3.4 for details regarding the star extraction method).

The total limb error which varies with the phase angle is either set to 0.25 pixels or to 0.50 pixels to model the influence of the effect observed by Cooper et al. (2014) for the astrometric reduction of the Saturnian moons Mimas, Enceladus, Tethys, Dione, and Rhea.

The total number of observations is varied between 200, 1000, and 2000 observations. 200 observations would represent a pessimistic case where 2000 observations would represent a similar number

Table 6.4: Observation cases for the JANUS Camera.

Case	Resolution	Exposure [J mag]	Limb error in Sun direction [pixels]	Total observations	Observations per epoch	Distribution
1	full resolution	7.2	0.25	200	5	70/20/10
2	1/4 full resolution	9.1	0.50	1000	20	100/0/0
3	1/2 full resolution	9.7	n/a	2000	50	n/a
4	n/a	10.4	n/a	n/a	n/a	n/a
5	n/a	12.2	n/a	n/a	n/a	n/a

of optical observations as performed by Cassini scaled by the duration of the mission (considering only the Jovian tour). Note that the case of 2000 observations is only used within the NSGA-II optimizer to show the maximal attainable result. In the sensitivity analysis, to limit the number of lines in one figure, only 200 and 1000 observations are used. The number of observation epochs is not adjusted directly, to observe the effect of clustering the images (high number of observations per epoch) instead of spreading the observations (low number of observations per epoch). The number of observations varies between 5 (average for the Cassini mission) and 50 (approximately the maximum of the Cassini mission).

To assess the realism of the comparison with Cassini, the number of flybys per year between the JUICE and Cassini mission is compared (as the number of flybys per year gives an indication of the amount of data which is acquired). The Cassini mission performed a number of 53 targeted and 29 non-targeted (in which only imaging was performed of the icy moons) over its nominal mission duration of 3.9 years yielding an average of 13.6 targeted flybys per year and an average of 21 total flybys per year (Strange et al. 2002). JUICE on the contrary performs only 29 flybys over the duration of the Jovian tour of approximately 3 years, yielding an average of 9.8 flybys per year (Boutonnet and Varga 2017). Thus the operational flexibility of JUICE with respect to Cassini is expected to be higher such that the estimated amount of optical astormetric observations as proposed for JUICE is deemed realistic. Nevertheless, as discussed in Section 2.6.3, the Europa science phase (as there are relatively many flybys in a short period of time) and the GCO500 phase are sizing with respect to the required datavolume and power requirements such that the operational flexibility in these mission phases is lower.

To account for the distribution of the JANUS epochs among the different phases two cases are considered. One case in which 70 %, 20 %, and 10 % of the images are acquired in respectively the flyby, GEO5000, and GCO500 phase. The other case considers all images acquired in the flyby phase (outside a period centered 24 hours around closest approach). The latter case is most realistic as the operational flexibility during the Ganymede tour is limited.

6.4.5. Baseline Case

To compare the influence of the different independent variables as discussed above, it is important to define a baseline case such that only the effect of the one observation settings is observed instead of the effect of another (hidden) observation setting. The baseline values of the independent variables as discussed above can be found in Table 6.5.

The baseline cases for the JUICE uncertainty, VLBI orbit cadence, and VLBI flyby cadence are chosen in line with Dirkx et al. (2017). The baseline VLBI uncertainty is established at $\sigma_{VLBI} = 0.5$ nrad. This uncertainty is considered for the baseline because the VLBI uncertainty of $\sigma_{VLBI} = 1.0$ nrad the current state of the art and $\sigma_{VLBI} = 0.1$ nrad might be difficult to achieve given the small number of extra-galactic reference sources available at the Ka-band as discussed in Section 4.6.2.

For the NavCam, the observation schedule for Io astrometry is chosen with a cadence of 2 days at 3 images per epoch as the baseline case, regarding to the proposed operations in Section 6.4.3,

Table 6.5: Baseline cases used for assessing the influence of different independent variables.

Observation Setting	Baseline	Observation Setting	Baseline
JUICE Uncertainty	Case 4	NavCam Observations per Epoch	3
VLBI Orbit Cadence	Case 2	JANUS Resolution	Full
VLBI Flyby Cadence	Case 2	Exposure	9.7 J mag
σ_{VLBI}	0.5 nrad	Lim error in Sun direction	0.25 pixels
NavCam Cadence	Every 2 days	Distribution	100/0/0

this case is more realistic and relaxes the required data volume. This might seem unrealistic given the preference for NavCam astrometry of Ganymede and Callisto. However, due to operational constraints, a large number of the proposed NavCam astrometry epochs are not possible for Io (note that this effect is less pronounced for Ganymede and Callisto as they are further away from Jupiter). Considering the operational constraints, a NavCam tracking arc of Io is performed on average every 4.7 days in the actual simulation for a NavCam cadence setting of 2 days. Thus after considering the operational constraints, the NavCam cadence of 2 days is deemed more realistic.

For the JANUS camera, full resolution is assumed. Furthermore, the maximum brightness (representing the faintest star which will be visible in the image) for the baseline case is 9.7 which coincides with the median of the magnitude of all stars found in the images from Tajeddine et al. (2013) and Tajeddine et al. (2015) using the UCAC2 star catalog. The fitting error of the satellite limb in the direction of the Sun is assumed to be 0.25 for the baseline in accordance with the results of Cooper et al. (2014) and Tajeddine et al. (2015) and make sure images with higher phase angles are preferred.

6.5. Optimization Settings

This section discusses the settings applied within the optimization framework. First of all for the observation settings, the baseline settings as proposed in Section 6.4.5 are used, except the conditional uncertainty of the JUICE spacecraft. This was decided because validation by Dirkx et al. (2017) showed that case 1 did most accurately describe the modeled JUICE orbit determination uncertainties. Furthermore, case 1 would be the most difficult to stabilize, as low conditional uncertainties result in high weights for the radiometric tracking observations. This means that the relative contribution of JANUS optical astrometry is reduced compared to the radiometric tracking observations. It is therefore expected, that the optimized solutions for the higher conditional uncertainties of the JUICE spacecraft will have lower condition numbers. However, the resulting formal errors will be larger.

Furthermore, a total number of 2000 observations is considered. A total number of 200 and 1000 observations are not considered within the optimization framework, because the full potential of JANUS astrometry needs to be assessed and running too many different cases would require too many computational resources. Therefore, as 2000 observations represent the maximum realistic number of observations, it is used to show the minimum attainable condition number considering the baseline observation settings.

Finally, the population size p and number of generations g for the NSGA-II algorithm are determined using Equation 6.1 which can be found on the documentation page of the NSGA-II implementation in MATLAB.[8]

$$\begin{aligned} p &= \min(\max(10n_{max}, 40), 100) \\ g &= 200n_{max} \end{aligned} \tag{6.1}$$

This means that for a total of 2000 observations at a cadence of 50 observations per epoch, the population size is 8000 and each generation contains 400 individuals. In Section 7.6 it is assessed whether the population p and the number of generations g as provides by Equation 6.1 are sufficient for the optimization problem posed in Section 6.1.

[8] "Find Pareto front of multiple fitness functions using genetic algorithm - MATLAB & Simulink - MathWorks Benelux - nl.mathworks.com `https://nl.mathworks.com/help/gads/gamultiobj.html?s_tid=doc_ta#bvf79ug-options` (accessed October 22, 2018)

7

Verification & Validation

This chapter presents the results for the required verification and validation steps that were performed. First of all, the dynamical model used to generate the normal equations matrix is validated using the L2 ephemerides in Section 7.1. As the observational weights have a strong influence on the attainable condition number, verification of those weights is essential. As discussed in Section 5.2 and 5.3, the determination of the weights can be divided among the radiometric weights and the optical weights. The radiometric and optical weights will be verified in respectively Section 7.3 and 7.4. Note that in these sections the observational uncertainty will be validated. The corresponding weights for the covariance analysis are acquired by the inverse of the observational uncertainty squared as discussed in Section 5.1.1. Subsequently, implementation of the covariance analysis without the inclusion of optical space-based astrometry is validated using data from a similar study in Section 7.5. Finally, Section 7.6 verifies whether the selected population size and number of generations, as used within the NSGA-II algorithm (see Section 6.2.2), are sufficient to acquire the optimum solution.

7.1. Validation of the Dynamical Model

The correct implementation of the dynamical model is validated in two steps. Firstly, the integrated state history is compared to the reference states provided by the L2 ephemerides in Section 7.1.1. Secondly, the orbital resonance in the integrated dynamics is validated in Section 7.1.2 by comparing, among others, the propagated Laplace angle ϕ_L to the Laplace angle calculated using the L2 ephemerides. The orbital resonance is validated as the Laplace resonance is crucial in estimating the dynamics of especially Io and Europa.

7.1.1. Validation of the Dynamical Model

For accurate interpretation of the results, the dynamical model should be correctly implemented. Therefore, the propagated states of the Galilean moons acquired by numerical integration of the model as described in Section 3.1 is compared to the states of the moons given by the L2 ephemerides provided by IMMCE.[1] The L2 ephemerides were used to define the JUICE trajectory (Boutonnet and Varga 2017) and are therefore used to validate the dynamical model. The L2 ephemerides are generated by Lainey, Arlot and Vienne (2004) using Earth-based radiometric observations over a period of more than 100 years. The reference states are acquired using the SPICE kernels (as discussed in Section 3.2). The norm of the position difference between the propagated states and the L2 ephemerides, the difference in inclination, the difference in mean longitude $\Delta\lambda_i$, and the difference in mean orbital motion Δn_i as well as the difference in right ascension of the ascending node Ω and mean anomaly M are given for the Galilean moons in Figure 7.1.

Figure 7.1(a) shows that the difference in position of Io and Europa is larger in magnitude than the position difference of Ganymede and Callisto. Furthermore, the position difference of Io and Europa shows periodic behavior, whereas the position difference of Ganymede and Callisto shows more linear behavior over time. The difference between Io and Europa on one hand and Ganymede and Callisto

[1] Available under `NOE-5-2010-GAL-a.bsp` at `ftp://spiftp.esac.esa.int/data/SPICE/JUICE/kernels` (accessed October 1, 2018)

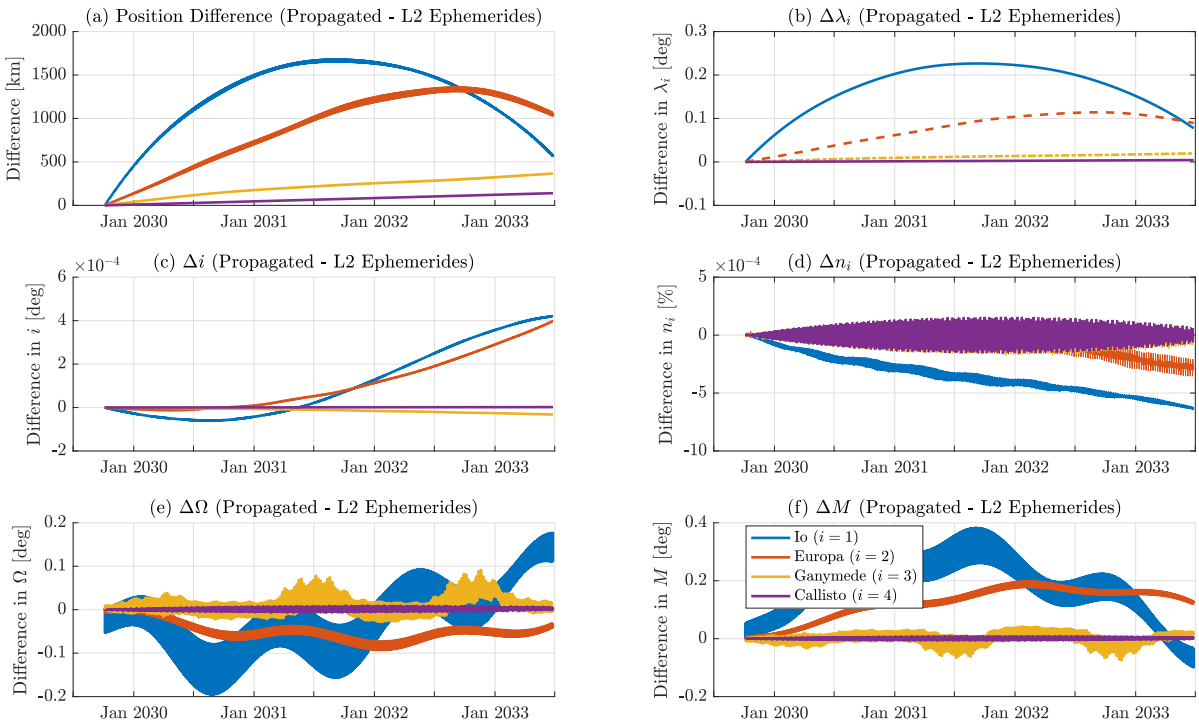

Figure 7.1: (a) Norm of the difference in position of the moons in kilometers, (b) difference in the mean longitude in degrees, (c) difference in inclination as a percentage of the inclination of the reference state (L2 ephemerides), (d) difference in mean orbital motion as a percentage of the mean orbital motion of the reference state (L2 ephemerides), (e) the difference in the right ascension of the ascending node (Ω) in degrees, and (f) difference in the mean anomaly M in degrees. Differences are computed between the integrated and reference states which are acquired from the L2 ephemerides using the SPICE interface. On the x-axes of all figure the date is presented in UTC.

on the other hand can be related to their respective distance to Jupiter. Ganymede and Callisto are respectively 2.5 and 4.5 times as far from Jupiter compared to Io. Therefore, the spherical harmonic accelerations of Jupiter have a larger impact on Io and Europa than on Ganymede and Callisto. A slightly different gravity model (compared to the model used for the L2 ephemerides) will thus have a more pronounced effect on the orbit of Io compared to the orbit of Callisto, which is indeed observed in Figure 7.1(a).

Figure 7.1(b) and (c) show that whereas the difference in inclination Δi is small, the difference in the mean longitude $\Delta\lambda_i$ is substantial, especially for Io and Europa, such that difference is almost completely related to the in-plane dynamics. Furthermore, a similar periodic trend can be observed for the mean longitude of Io and Europa compared to the trend observable for the position difference of Io and Europa (Figure 7.1(a)). This confirms that the difference between both models is primary in the in-plane dynamics.

Considering Figure 7.1(b) which shows the difference in mean longitude, it can be concluded that especially the integrated dynamics of Io and Europa are advancing the reference states of Io and Europa (in the direction of the orbital motion). This, however, is not consistent with the relative reduction in of the mean orbital motion as observed for Io and Europa in Figure 7.1(d). It can thus be concluded that other relative perturbations (accelerations which are different between both models) have more impact on the progression of the mean anomaly as seen in Figure 7.1(f). Nevertheless, from Figure 7.1(d) a secular change in the mean motion can be observed for both Io and Europa, such that the effect of the declining mean orbital motion starts to become more apparent in the second part of the integrated dynamics. This is confirmed by the decreasing difference in the mean anomaly as observed in the second part of Figure 7.1(f).

Comparing Figure 7.1(b), (e), and (f) it can be seen that the right ascension of the ascending node (Figure 7.1(e)) has an opposing trend to the mean orbital motion (Figure 7.1(f)) such that the resulting shift in mean longitude is smaller (Figure 7.1(b)).

The resulting magnitude of the position error ($\approx$ 1600 km) is substantial for especially Io and Europa

and will have a considerable effect on the resulting covariance analysis in case the JUICE spacecraft is tracked directly. This is related to the fact that the relative position of the JUICE spacecraft with respect to the moons is substantially different during the flybys (as a result of the integration error) which will have a substantial impact on the normal equations matrix. However, for this thesis, the moons are tracked directly such that the effect of the difference between both models is less pronounced (e.g. the tracking geometry does not change substantially). The difference will be on the same order of magnitude as the assumption that the tracking station on Earth is located at the geocenter instead of at the surface of the Earth (note that the difference is approximately equal to the radii of both Io and Europa). Finally, as this thesis is more concerned with the relative performance of space-based astrometry, the exact geometry is less important and the difference between both models is expected to have negligible influence on the results of this thesis as the interpretation will be mostly qualitative. Note that position of JUICE, as required for the transformation of $\sigma_{\mathbf{r}_{sc}^{i}}$ from the LVLH frame to an inertial frame as required in Equation 5.15 to 5.18, is directly retrieved with respect to the reference ephemerides such that the integration error does not affect the position of JUICE.

The origin of the substantial differences between the propagated and reference dynamics is most likely related to the use of slightly different values for the various physical constants compared to the values used to generate the L2 ephemerides which are listed in the supplementary document of Lainey et al. (2009). Moreover, inconsistencies between the rotation model with the reference ephemerides might induce a secular effect on the dynamics as the C_{22} effect will be consistently different throughout an orbit. Ideally, this difference would have been further reduced. However, due to time constraints this is left as an recommendation for future research.

7.1.2. Validation of the Laplace Resonance within the Simulated Dynamical Model

As discussed in Chapter 1, the dynamics of Europa and especially Io need to be estimated from the dynamics of Ganymede which are dynamically coupled to the dynamics of Io and Europa through the Laplace resonance. Therefore, it is important that the inner three Galilean moons remain in resonance for the integrated trajectories for the duration of the JUICE mission. Otherwise the dynamics of Io and Europa are no longer (or to a lesser extend) observable in the motion of Ganymede. The dynamical coupling can be assessed by monitoring the resonant argument Φ_L as given in Equation 2.5. Furthermore the angle between the longitude of conjunction and pericenter θ_{ij} (as given in Equation 2.6 and 2.7) is evaluated to assess the individual pairs of resonating satellites. The differences between both the propagated and reference Laplace angles can be found Figure 7.2.

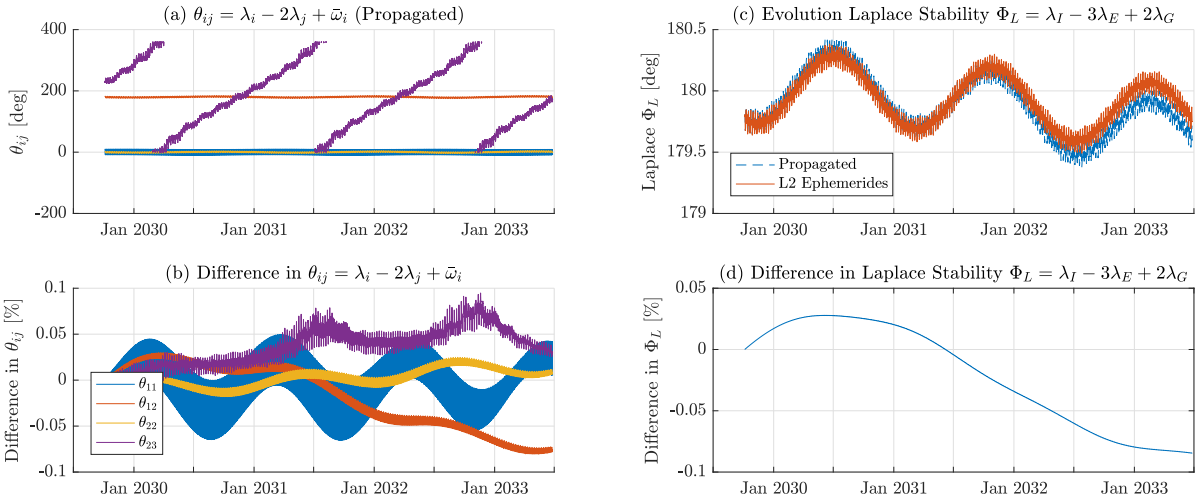

Figure 7.2: (a) The angle between the longitude of conjunction and the argument of pericenter θ_{ij} in degrees for the inner Galilean moons for the two resonant pairs within the Laplace resonance, (b) the difference of the angles θ_{ij} between the propagated and reference L2 ephemerides as a percentage of 180°, (c) both the propagated and reference Laplace resonant argument Φ_L in degrees, and (d) the difference between the propagated and reference Laplace resonant argument Φ_L as a percentage of the reference Φ_L. On the x-axes of all figures the date presented in UTC.

Figure 7.2(a) shows that (as discussed in Equation 2.6 and 2.7) θ_{11} and θ_{22} are indeed librating around pericenter (0°), θ_{12} is indeed librating around apocenter (180°) while θ_{23} circulates through 360°. Fur-

thermore, Figure 7.2(b) shows that the difference between the propagated and reference longitude of conjunction stays within 0.1 % of the reference angles. Note that difference is calculated as a percentage of 180° as the reference of θ_{11}, θ_{22}, and θ_{23} regularly pass zero resulting in large percentual differences. Moreover, it can be noticed that θ_{11} and θ_{22} oscillate around the reference value, where θ_{12} and θ_{23} show a oscillation around a slightly diverging trend. However, over the duration of the JUICE mission this diverging trend is only slightly higher than the oscillating difference observed for θ_{11} and θ_{22}. Thus as no substantial diverging behavior is observed it can be concluded that the inner three moons remain in resonance for the duration of the JUICE mission.

The resonance of the inner three moons is again confirmed by observing Figure 7.2(c) in which the resonant argument Φ_L is given for both the propagated and reference (L2 ephemerides) dynamics. It can be observed that the resonant argument is indeed librating around 180° as discussed in Section 2.3. However, the libration period is not consistent with the period of 2056.9 days as given by Hussmann et al. (2010). Nevertheless, this is true for both the propagated and reference resonant argument Φ_L. This might be related to physical constants which are slightly different compared to the actual physics imposing additional oscillations around the actual resonant argument. Nonetheless, the difference between the propagated and reference Laplace resonant argument Φ_L as observed in Figure 7.2(d) shows no diverging behavior within the duration of the JUICE mission and stays (similarly as the angle θ_{ij}) within the 0.1 % of the reference value. Thus, the behavior of both the propagated angles θ_{ij} and Φ_L confirms that the inner three Galilean moons remain in resonance for the duration of the JUICE mission and are thus sufficiently accurate for the qualitative assessment of the JUICE-based optical astrometry. However, for a quantitative assessment of the contribution of JUICE-based optical astrometry as well as when the inclusion of Earth-based astrometry is required over longer timescales the dynamical model needs to be improved. Due to time constraints this is left as an recommendation for further studies.

7.2. Verification of the Numerical Integration

Next to validation of considered dynamical model, the propagation and integration settings should be verified. Therefore, the residual-mean-squared (RMS) of the norm of the difference in position between the propagated and reference trajectory is computed per moon. The result is plotted versus the integration time-step in Figure 7.3.

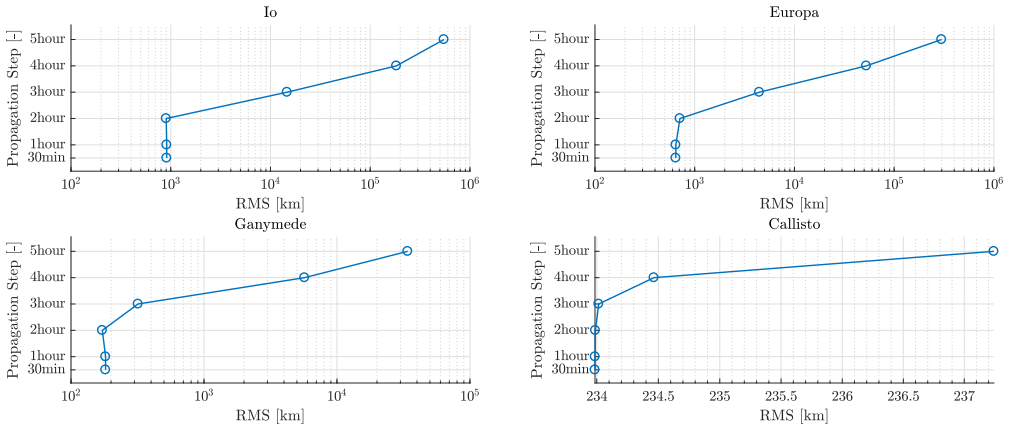

Figure 7.3: On the x-axis the residual-mean-squared (RMS) of norm of the difference between the propagated and L2 ephemerides of the Galilean moons in kilometers for the DOPRI8 integrator. On the y-axis the integration time-step. Note that the x-scale is different for the different Galilean moons. Note that the independent variable, the integration time-step, is found on the y-axis to be consistent with literature.

Figure 7.3 shows that the range of propagation steps considered here is hardly affecting the propagated results for Callisto (note the scale of the x-axis compared to the scale of the other moons) compared to the observed range of values of the RMS of the other moons. This can be related to the fact that Callisto is not affected by the Laplace resonance. Furthermore, because its relatively large distance from Jupiter, the dynamics are relatively slow compared the dynamics of the inner Galilean moons. This effect is also visible while comparing the difference between the propagated and reference trajectory of Ganymede on one hand to the difference of Io and Europa on the other hand. These results are in line

with the results found while validating the correct implementation of the acceleration model (see Figure 7.1). This figure showed that the difference between the propagated dynamics was substantially lower for Ganymede compared to Io. Note that the remaining difference for a propagation step of 30 minutes is (most likely) related to the use of a slightly different gravity model (see Section 7.1).

Furthermore, it can be seen in Figure 7.3 for especially Io (and to a lesser extend for Europa and Ganymede) that there is a large difference, on the order of 10^4 kilometer, between a propagation step of 3 hours and 2 hours and that there is almost no difference when the propagation step is reduced from 1 hour to 30 minutes. The substantial difference for integration steps larger than 2 hours is a result of truncation errors resulting form large numerical integration steps. After reducing the integration time-step below 2 hours, the remaining difference is a result of (most likely) physical constants being slightly different between both the propagated and reference model (as discussed in Section 7.1.1). When the integration time-step would be further reduced an increase in the difference between both models is likely to be observed as a result of round-off errors.

It can thus be concluded that a propagation step of 1 hour is sufficiently accurate for modeling the dynamics of the Galilean moons, as for smaller integration steps the error is not further reduced. The remaining, still relatively large error (on the order of 1600 km for Io as can be seen in Figure 7.1(a)), is as previously discussed, most likely attributed to physical constants with a slightly different value. Due to the fact that the moons are directly observed and the qualitative assessment of the results the magnitude of these errors is acceptable. However, as discussed in both Section 7.1.1 and 7.1.2, the remaining difference would ideally be further reduced to enable a quantitative assessment of the results.

7.3. Verification of the Radiometric Weights

As the uncertainty of the radiometric tracking observables is primarily determined by the conditional uncertainty of JUICE, its implementation should be verified. Figure 7.4 shows the observation uncertainty for the radiometric tracking observations. Consequently the most important features confirming the correct implementation of the conditional uncertainty of JUICE are discussed per radiometric tracking type.

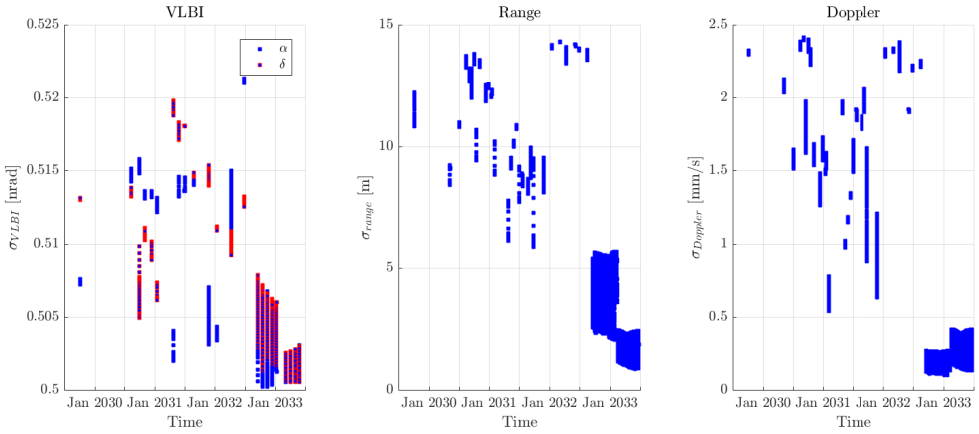

Figure 7.4: The observation uncertainties of the radiometric tracking observables including the conditional uncertainty of JUICE. From left to right the VLBI, range and range-rate (Doppler) uncertainties. For the VLBI observations, the right ascension α is indicated in blue, while the declination δ is indicated in red. Note that the weights are generated using the conditional JUICE uncertainty case 1 and an VLBI observation uncertainty of $\sigma_{VLBI} = 0.5$ nrad. On the x-axes of all figures the date presented in UTC.

7.3.1. VLBI Weights

- Observing Figure 7.4 (left figure) shows that for the VLBI uncertainty the observation uncertainty (σ_{VLBI} = 0.5 nrad) dominates and the JUICE conditional uncertainty only marginally affects the total observation uncertainty.

- Figure 7.4 (left figure) shows that the maximum VLBI uncertainty gradually increases over the du-

ration of the JUICE mission. This is the result of the mapped conditional uncertainty of JUICE being inversely proportional to the range vector between the Earth and the observed moon. Thus as the range between the Earth and Jupiter decreases during the JUICE mission (see Appendix A.7) as Jupiter moves from its apocenter towards its pericenter, the mapped conditional uncertainty increases. Other effects (such as the rotation of the Earth around the Sun) impose a variation on this trend.

- Assuming the norm of the different JUICE components of the JUICE conditional spacecraft uncertainty (for JUICE uncertainty case 1 during the flyby phase as given in Table 6.1), the mapped VLBI uncertainty ranges from 0.015 to 0.023 nrad (depending on the range between the Earth and Jupiter). As expected, no mapped uncertainties higher than 0.023 nrad are found in Figure 7.4.

- Figure 7.4 distinguishes between the uncertainty in right ascension (blue) and declination (red). Where the declination unit vector maps mostly to the cross track direction while the right ascension vector maps mostly to the radial and along-track direction. Thus as the spacecraft uncertainty in the radial direction is substantially lower than the uncertainty in the along-track and cross-track direction, the mapped uncertainty is expected to be higher for the declination compared to the right ascension. This is indeed conformed by observing Figure 7.4 where the declination uncertainty (in red) is higher than the uncertainty in right ascension for a large number of cases. This is especially pronounced during the first flyby and the orbit phase. However, this effect is limited during the high latitude phase (see Table 2.2) and in case the right ascension unit vector maps fully onto the along-track conditional uncertainty which is higher than the cross-track conditional uncertainty. In that case the uncertainty in right ascension should be higher than the uncertainty in declination. More importantly, Figure 7.4 shows that the variation of the uncertainty in the right ascension is substantially larger during a tracking arc compared to the variation of the uncertainty in declination. This is related to the large difference between the radial and along-track conditional uncertainties to which the right ascension vector primarily maps.

Range Weights

- Observing Figure 7.4 it can be seen that for the range uncertainty the mapped condition uncertainty of the JUICE spacecraft dominates.

- Assuming the norm of the different JUICE components of the JUICE conditional spacecraft uncertainty (for JUICE uncertainty case 1 during the flyby phase as given in Table 6.1), the mapped range uncertainty equals 14.18 m. Indeed no mapped range uncertainties higher than 14.18 m are observed in Figure 7.4.

- It can be noted that in the period after January 2031 (the Jupiter high latitude phase) the total uncertainty is substantially lower. This can related to the high inclination of the JUICE spacecraft during this phase (see Table 2.2) such that the viewing geometry (geometry between the line-of-sight and the orbital normal vector of the satellite) changes from edge-on to face-on. Therefore, the range vector will partially map more onto the cross-track uncertainty which is smaller than the along-track uncertainty, resulting in a lower total uncertainty.

Doppler Weights

- Observing Figure 7.4 it can be observed that the Doppler uncertainty (similarly to the range uncertainty) is dominated by the conditional uncertainty of the JUICE spacecraft.

- Assuming the norm of the different JUICE components of the JUICE conditional spacecraft uncertainty (for JUICE uncertainty case 1 during the flyby phase as given in Table 6.1) as well as a tracking arc length of 8 hours, the mapped Doppler uncertainty equals 2.4 mm/s. Indeed no mapped range uncertainties higher than 2.4 mm/s are observed in Figure 7.4.

- Similarly to the range uncertainty, it can be observed from Figure 7.4 that the Doppler uncertainty is lower for the Jupiter high latitude phase.

- Figure 7.4 shows that the total observation uncertainty is higher during the GCO500 phase compared to the GCO/GEO5000 phase. This is related to the scaling term ΔT which is equal to the orbital period such that a shorter orbital period yields a higher JUICE conditional velocity uncertainty. As discussed in Section 5.2 this represents the fact that for orbits closer to the central body, the corresponding velocity uncertainty has a higher sensitivity with respect to the position uncertainty.

Conclusion

All the radiometric uncertainties (VLBI, range, and Doppler) show behavior that is expected both in terms of both the observed signatures and the corresponding magnitudes. Therefore, it can be concluded that the uncertainty model as discussed in Section 5.2 is implemented correctly.

7.4. Validation & Verification of the Optical Weights

The verification and validation of the uncertainty model for the optical astrometry is accomplished in two steps. First of all, the uncertainty model is validated using the uncertainties of Cassini Optical astrometry using the data provided by Tajeddine et al. (2015) (with a focus on the pointing uncertainty) and Antreasian et al. (2005) (with a focus on the limb-finding uncertainty) in Section 7.4.1. In the second step, the JANUS uncertainty is verified by checking the corresponding behavior and order of magnitude. This is important as the differences in camera designs between JANUS and the Cassini NAC result in different behavior of the uncertainties. The results from this verification can be found in Section 7.4.2.

7.4.1. Validation using the Cassini NAC

The validation of the uncertainty model will be accomplished in four steps. First of all, the modeled uncertainty will be compared to the results of Tajeddine et al. (2015) with a focus on the pointing uncertainty. Secondly, the modeled uncertainty will be compared to the uncertainty model of Antreasian et al. (2005) focusing on the limb-fitting uncertainty varying as a function of the proximity of the moon that is imaged. Thirdly, conclusions will be drawn regarding the validity of the used model and finally recommendations will be given how to improve the uncertainty model in future studies.

Pointing Uncertainty

Note that the uncertainty model for the optical astrometry is primarily based on the model presented by Tajeddine et al. (2013). Thus, the modeled uncertainties should match the uncertainties given in the supplementary information of Tajeddine et al. (2015) (which uses a similar weight model). The uncertainty model is not directly implemented (as this requires, among others, the exact pointing of the camera and actual limb-finding process) but only considers the same error sources and how they relate to the observation uncertainty. Therefore validation using the results as found by Tajeddine et al. (2015) does indicate how well the adopted model (which is an approximation of the model by Tajeddine et al. (2013)) represents the actual uncertainty.

Figure 7.5(a) gives the total observational uncertainty as function of the number of stars. The number of stars is chosen as the independent variable since the pointing uncertainty is dominant for the Cassini NAC. This is is a consequence of its limited field-of-view such that less reference stars available. Furthermore, the pointing uncertainty is a function of the number of stars which are in field of view (see Equation 5.20). Note that the modeled uncertainty is evaluated based on the number of stars found by Tajeddine et al. (2015), such that only the performance of the uncertainty model is assessed. As the maximum pointing uncertainty (for one star in field-of-view) of approximately 0.7 arcseconds scales with the inverse of the square-root of the number of stars, it can be observed that the pointing uncertainty is indeed dominating for the Cassini optical astrometry.

Figure 7.5(a) shows that between 1-30 stars the modeled uncertainty and the uncertainty given by Tajeddine et al. (2015) are quite similar. However, for a higher number stars there is a larger difference. This is related to the limb-fitting uncertainty which only partially scales with the phase angle θ is seen in Equation 5.22. In case of a phase angle of 90° (which is the phase angle of most images as a consequence of the Cassini trajectory design (Cooper et al. 2014)) this yields an uncertainty of 0.25 arcseconds which is already higher than the total uncertainty of the results provided by Tajeddine et al. (2015). Thus, although the pointing uncertainty is accurately estimated, the limb-fitting uncertainty is

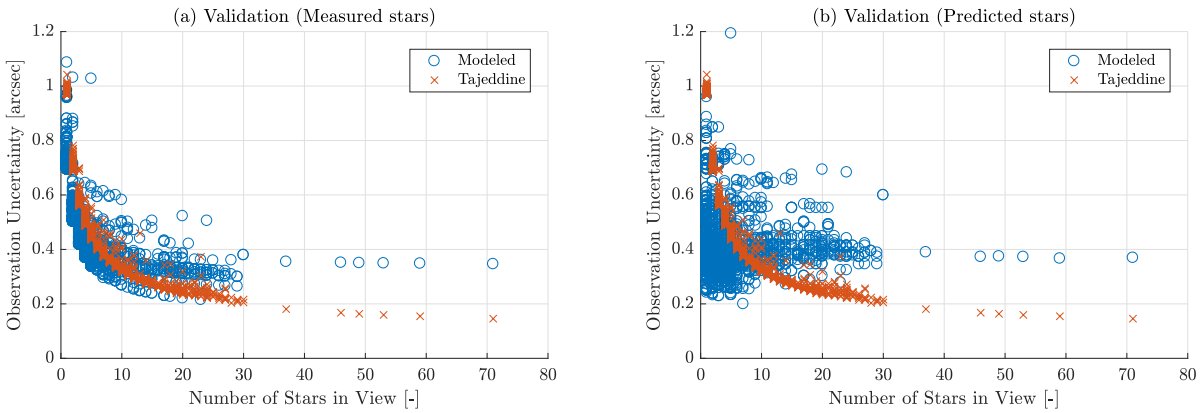

Figure 7.5: Modeled observation uncertainty (this thesis) in arcseconds compared to the observation uncertainty of Tajeddine et al. (2015) of Tethys and Rhea (combined in both figures). On the left (a) the measured number of stars from the data from Tajeddine et al. (2015) is used to compute the pointing uncertainty (using Equation 5.20) where on the right (b) the estimated number of stars (using the method described in Section 5.3.4) is used to compute the pointing uncertainty. Note, however, that for the right figure (b) the stars found by Tajeddine et al. (2015) are used to plot the results. This enables a better comparison between both the modeled and actual uncertainties (which differ mostly as a result of an error in the number of estimated stars that are in field-of-view).

overestimated for images with a large number of stars (which mostly corresponds to images in which a small part of the image is filled by the moon).

In Figure 7.5(b) the pointing uncertainty is determined using an estimated number of stars (as discussed in Section 5.3.4). However, the modeled uncertainty is plotted using the number of stars as found by Tajeddine et al. (2015) to emphasize on the difference between both models. Contrary to Figure 7.5(a), the behavior of both models is quite different between 1-30 stars. Nevertheless, the general trend is still observable. This large spread is fully related to the number of stars that is generally overestimated using the method discussed in Section 5.3.4. Nevertheless, the results for more than 30 stars are quite similar between Figure 7.5(a) and (b).

As discussed in Section 5.3.5, the number of stars in field-of-view will be generally higher for JANUS compared to the Cassini NavCam which is related to its larger field-of-view. Even in case a large part of the image is covered by a moon, the remainder of the background covers a larger part of the celestial sphere compared to the Cassini NAC. Therefore, more background stars will be observable which means the pointing uncertainty will be less dominant for JANUS and an overestimation of the number of stars has thus less impact on the total observational uncertainty. The reduced influence for JANUS is related to the low estimated pointing uncertainty of 0.16 arcseconds (see Section 5.3.5), which is substantially lower than the values observed in both Figure 7.5(a) and (b), as well as to the sensitivity of the pointing error as a function of the number of stars that is three times as low for JANUS compared to the Cassini NAC (see Section 5.3.5).

Limb-finding Uncertainty

Antreasian et al. (2005) introduces a variable limb-finding error which is a function of the apparent diameter of the moon under consideration (see Section 5.3.2). As a result, the fitting uncertainty is higher for images which are made at closer distances to the satellite. Figure 7.6 compares such a model with the model used in this thesis (which only scales with the phase angle). Note that all differences observed in Figure 7.6 are only related to the fitting uncertainties, as the pointing and spacecraft uncertainties are modeled similarly in both models.

Comparing Figure 7.6(a) and (c) it can be seen that, although the baseline values (uncertainty floor) of the uncertainty in pixels are (quite) similar between both models. The largest difference (up to 3.5 pixels), however, occurs when the distance between the target satellite and the spacecraft is small. This difference can be directly related to the limb fitting error which is a function of the apparent diameter in the model presented by Antreasian et al. (2005) (see Figure 7.5(a)). Thus, the model adopted in this thesis is substantially more optimistic compared to the model proposed by Antreasian et al. (2005) for images in which a large part of filled by the observed moon. This is evident by comparing Figure 7.6(b) and (d).

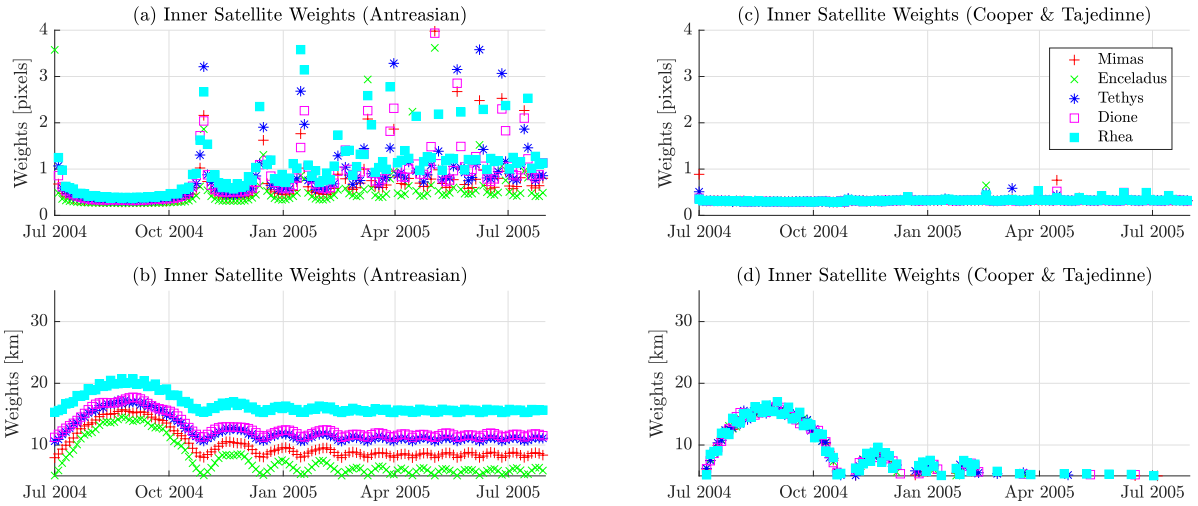

Figure 7.6: Modeled observation uncertainty (figure (c) and (d)) compared to the observation uncertainty of Antreasian et al. (2005) ((a) and (c)) for the inner Saturnian moons. The measurement uncertainty is shown both in pixels and kilometers. On the x-axis the date is given in UTC.

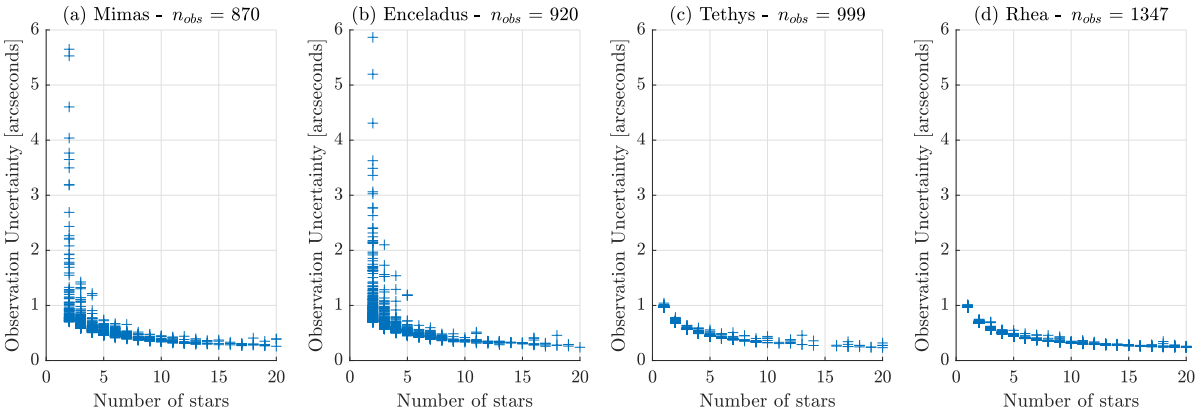

Figure 7.7: Comparison of the total uncertainties of the astrometric observations in arcseconds of Mimas (a) and Enceladus (b) (Tajeddine et al. 2013) on one hand and Tethys (c) and Rhea (d) (Tajeddine et al. 2015) on the other hand. Note that the positions of Tethys and Rhea (figure (c) and (d)) are determined using a limb-finding algorithm which has a higher sensitivity for images with a large phase angle. The independent variable is the number of stars in field-of-view. The date on the x-axis refers to UTC-time.

As discussed in Section 5.3.2, Tajeddine et al. (2015) did use a refined limb finding algorithm in which the fitting error in the direction of the Sun was no longer visible. Moreover, comparing the observational uncertainty as given in Figure 7.7(a) and (b) which represent the results of Tajeddine et al. (2013) with the observational uncertainty as given in Figure 7.7(c) and (d) which represent the results of Tajeddine et al. (2015) in which the refined (higher sensitivity) limb finding algorithm was used, it can be concluded that the refined limb-finding algorithm not only reduces the effect of the phase angle, but also substantially reduces the effect of the variable distance at which the moons are observed. This is pronounced by the fact that in both Figure 7.7(a) and (b) between 1-5 stars uncertainties up to 6 arcseconds can be observed (which equals approximately 4.9 pixels for the Cassini NAC). These uncertainties are (more or less) consistent with the results from Figure 7.6(a). In Figure 7.7(c) and (d), however, between 1-5 stars the highest uncertainty is found to be approximately 1 arcsecond (which equals approximately 0.8 pixels for the Cassini NAC). Note that the difference between the observed uncertainties between Mimas and Enceladus on one hand and Tethys and Rhea on the other hand cannot be attributed to the flyby geometry as Saturn tour includes flybys for Enceladus, Tethys, and Rhea but lacks flybys for Mimas.[2] Furthermore, Figure A.6 in Appendix A.10 shows that both moons are observed at close dis-

[2]Cassini Mission Saturn Tour “Flybys | Saturn Tour - Solar System Exploration: NASA Science” solarsytem.nasa.gov https://solarsystem.nasa.gov/missions/cassini/mission/tour/flybys/?page=4&per_page=40&order=

tances (for which a large part of the image is filled by the moon). Thus the refined limb-finding algorithm not only reduces the signature in the direction of the Sun, but also reduces the effect of the variable range at which the images are taken.

Conclusion

From the previous analysis it can be concluded that the the pointing uncertainty is accurately implemented (see Figure 7.5(a)). However, the number of stars is currently overestimated. Nevertheless, the estimation of the number of stars (which serves as an input to determine the pointing uncertainty) has a less pronounced effect on JANUS compared to the Cassini NAC due to its relatively large field-of-view combined with the improved resolution. For a more accurate estimation of the pointing uncertainty, the actual number of stars in field-of-view should be determined.

Regarding the limb-fitting uncertainty, assuming the refined limb-finding algorithm used by Tajeddine et al. (2015), the current model used in this thesis quite accurately represents uncertainty for close-by images. However, for images that are further away the limb-finding uncertainty is overestimated. Nevertheless, as the focus of this study is primarily qualitative, the actual magnitude of the uncertainty is less important as long as the relative behavior is modeled correctly. This behavior is found to be present in a limited fashion (see Figure 7.6(a) and (c)). Nonetheless, actual pointing of the camera as well as the actual camera settings are required for a more accurate estimation of the uncertainty of the optical astrometry.

Recommendations for Improvements

An improvement of the estimation of the pointing uncertainty can be accomplished by further investigating the relation between the exposure time and the number of available stars together with the relative satellite size. The data as provided in the supplementary information of Cooper et al. (2014) would provide a good starting point for this analysis. The data-set contains the combination of the exposure time per image in milliseconds as well as the star ID's (from the UCAC2 catalog) for the stars that are visible in the image together with their apparent magnitude. Moreover, using the Saturn ephemerides (see Tajeddine et al. (2013) for the required meta-kernel) the apparent diameter of the Saturnian satellite can be computed (such that the fraction of the image filled by the moon can be computed). The synthesis of the aforementioned data would yield a more advanced model between the exposure time, fraction of the image which is filled by the satellite and the number of available background stars.

As Figure 7.5(a) and (b) showed that the limb-fitting uncertainty was not very well modeled for images in which only a small part of the moon is in field-of-view (in which a large number of background stars is observed). Therefore, a limb-finding uncertainty which scales with the distance to the target moon is desirable. However, the model as proposed by Antreasian et al. (2005) is too pessimistic regarding the uncertainties found by Tajeddine et al. (2015). Therefore, the scaling factor C (see Equation 5.21) should be fitted using the data provided in the supplementary information of Tajeddine et al. (2015). Finally, as the improved limb-finding algorithm gives quite optimistic results. More studies should be used to confirm the performance of such an algorithm.

7.4.2. Verification of the JANUS Modeled Uncertainty

Now that the optical uncertainties are validated for the Cassini NAC, the correct implementation of the JUICE uncertainties should be verified Therefore, the different variables associated to the uncertainty of the optical astrometry are visualized over the duration of the JUICE mission in this Section to assess the corresponding signatures and order of magnitude.

Figure 7.8(a) shows that the number of stars is larger than the expected number of stars (which equals 111 stars as given in Section 5.3.5). As discussed above, this advocates the need for a more refined method of estimating the number of stars (especially related to the number of stars as a function of exposure time). It can therefore be noted (from Figure 7.8(b) and (c)) that the pointing uncertainty is optimistic (maximum pointing uncertainty is approximately 0.048 pixels) and inferior to the standard limb-fitting uncertainty (which is equal to 0.1 pixels). However, note that even for the expected number of stars, the pointing uncertainty is approximately 0.17 arcseconds (approximately 0.05 pixels for JANUS) which is still substantially smaller than the expected limb-finding error (as a function of the phase angle).

publish_date+desc%2Ccreated_at+desc&search=&tags=cassini&category=264 (accessed October 15, 2018)

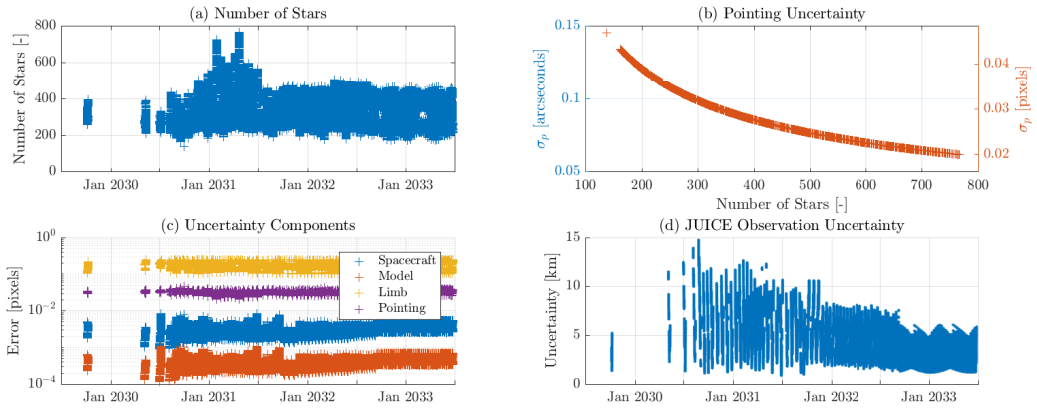

Figure 7.8: Number of stars(a) , pointing uncertainty (b) (both in arcseconds and pixels), total uncertainty (c) in pixels per contributing component and the JUICE observation uncertainty in kilometers (d). Note that the pointing error has two y-axes which both refer to the same data-set (although the color is different). The date on the x-axis refers to UTC-time.

Furthermore, Figure 7.8(b) shows that the limb-finding uncertainty dominates the total uncertainty and that the spacecraft and shape model uncertainties are respectively two and three orders of magnitude smaller than the limb-finding uncertainty. Finally, by observing the JUICE total observation uncertainty in kilometers (Figure 7.8(d)) it can be seen that the range of uncertainties is more or less consistent with the uncertainties adopted by Dirkx et al. (2017) which ranges from 5 to 20 kilometers, except for the lowest uncertainties which are approximately 5 kilometer lower. This difference can be related to the fact that the uncertainties used for this study assumed the refined limb-finding algorithm as used by Tajeddine et al. (2015). Nonetheless, to improve the realism of the uncertainties presented in Figure 7.8, the influence of the apparent diameter of the moon (thus the variable distance at which the image is acquired) should be further investigated using the data from Tajeddine et al. (2015). Furthermore, it should be validated if the number of visible stars increases indeed proportionally to the area covered by a camera on a unit sphere.

7.5. Verification of the Covariance Analysis

To ensure the results found by this study are valid, the framework used to generate the results should be validated. As the covariance analysis considered in this thesis does not estimate biases, the computed errors are compared to the formal errors found by Dirkx et al. (2017) in case no biases were estimated[3]. The results of this comparison can be found in Table 7.1.

From Table 7.1(e) it can be seen that the formal errors provided by this study are substantially lower than the formal error of Dirkx et al. (2017) in case the observation biases are estimated (see Table 7.1(a)). These results are in line with the Section 5.2.3 which states that assuming the conditional uncertainty to be equal to the marginal uncertainty (which is equivalent to not estimating the observation biases) results in optimistic results.

Comparing Table 7.1(c) and (e) (in which no biases are estimated) it can be seen that the formal errors provided by this thesis are more in line with the validation results (without bias case of Dirkx et al. (2017)). Nevertheless, some difference remains. This difference can be related to the high condition numbers which makes the resulting formal errors prone to numerical noise. Furthermore, the different reference trajectory (see Section 6.4.1) may result in different tracking geometry and different conditional uncertainties for the synthetic observations (see Section 5.2.2). As result the resulting formal errors may be different.

Note that although, the percentual difference (see Table 7.1(d)) is relatively large for both Ganymede and Callisto, the absolute difference (compare Table 7.1(c) and (e)) is relatively small, much smaller than the absolute differences for Io and Europa. This can be related to the fact that Ganymede and Callisto are observed directly.

[3]Not published - Dr.ir.D.Dirkx - Personal communication
[4]Dr.ir.D.Dirkx - Personal communication

Table 7.1: Upper row (a) gives the formal errors as found by Dirkx et al. (2017) for JUICE uncertainty case 4 and a VLBI uncertainty of σ_{VLBI} = 0.5 nrad in case the observation biases as discussed in Section 5.2.1 are estimated. The second row (b) gives the improvement in case the biases are not estimated.[4] The third row (c) gives corresponding formal errors as a result of the improvement showed in (b). Moreover, (d) gives the difference between the formal errors found in literature and the baseline as discussed in Section 6.4.5 is given as a percentage of the literature values. Finally, the baseline formal errors are given in the last row (e).

	Io		Europa		Ganymede		Callisto	
	IP	OP	IP	OP	IP	OP	IP	OP
Literature								
(a) With Bias [m]	582	613	335	145	24.4	27.2	28.9	71.8
(b) Without Bias [%]	−45.1	–	−73.6	−60.4	−59.6	−77.9	−88.4	−54.2
(c) Without Bias [m]	319.5	613.0	88.4	57.4	9.9	6.0	3.4	32.9
Baseline								
(d) Without Bias [%]	−35.3	45.9	−75.2	15.1	52.0	81.4	−64.5	−39.2
(e) Without Bias [m]	206.6	894.3	21.9	66.1	15.0	10.9	1.2	20.0

For the out-of-plane component of both Io, Europa, and Ganymede (see 7.1(d)), higher results are found compared to the results performed by Dirkx et al. (2017). This is especially pronounced for Io, for which the out-of-plane dynamics are only observed indirectly. However, as the out-of-plane coupling in the Laplace resonance is rather weak, the signature of Io in the dynamics of Europa and Ganymede is very small, thus a small change in the actual trajectory or the moons state can result in substantially different results.

The relative behavior of the formal errors of this thesis is comparable to the results found by Dirkx et al. (2017) (compare Table 7.1(a) and (e)), except for the in-plane formal error of Europa which is substantially smaller compared to the out-of-plane formal error. This might be related to the fact that the JUICE trajectory used by Dirkx et al. (2017) compared trajectory used in this study is especially different relating to the flybys of Europa (see Section 6.4.1). Nevertheless, the results found here indicate that the covariance analysis implemented in this thesis is sufficiently accurate to assess the relative contribution of JANUS optical astrometry.

7.6. Verification of Optimizer Settings

For the interpretation of the optimized JANUS observation schedule, it is important that the optimization algorithm has converged such that the presented results represent the attainable optimum. A measure for convergence (as discussed in Section 6.2.2) is the total number of fronts (and thus number of ranks the individuals can be assigned to) on which the individuals are located together with the number of individuals on the first front. The algorithm has converged when there is only one front and all individuals are located on that front. Furthermore, the relative improvement of the objective of the next generation with respect to the previous generation also gives a measure for the convergence of the algorithm. The convergence properties for the optimization of the JANUS epochs as discussed in Chapter 8 can be found in Figure 7.9.

Figure 7.9 shows that largest improvements are realized in approximately the first 800 generations. It can be seen that after 800 generations there are numerous occasions where the all the individuals are located on the first front. However, in many cases the number of fronts increases temporarily. It can be seen that this corresponds directly to improvement on the condition number (shown in Figure 7.9(b)). Interestingly, this behavior occurs even after 4000 generations, although all individuals have migrated to the first front for more than 2000 generations. Nevertheless, it can be seen that after 4000 generations only small improvements occur which have a high temporal distribution (i.e. improvements are realized only once every 100 generations). Therefore, the actual improvement on the condition number is small (compare this to the initial 800 generations where larger improvements are realized every generation). Note that this trend is also visible in the absolute change of both the condition number and the formal error which can be found in Appendix A.8. As the difference over the past 6000 generations is not

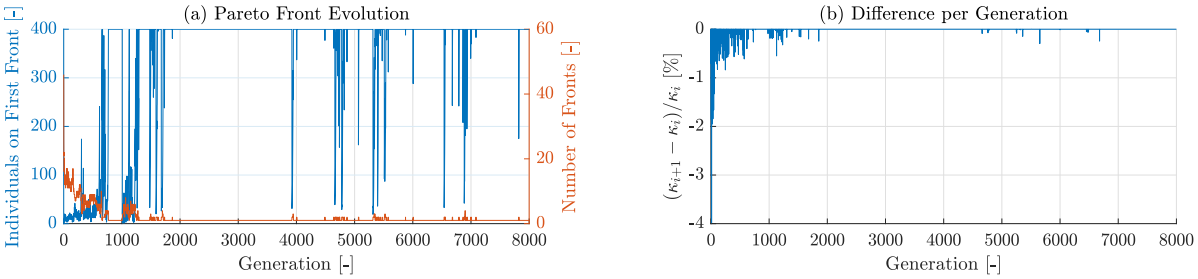

Figure 7.9: Left figure shows the number of individuals on the first front as well as the total number of fronts as a function of the number of generations. The right figure shows the percentage of improvement of the condition number with respect to the previous generation calculated as $(\kappa_{i+1} - \kappa_i)/\kappa_i)$. The improvement is given as a percentage of the previous condition number as a function of the number of generations. Note that the total number of generations is equal to 8000 as discussed in Section 6.5.

substantial, the optimization algorithm is clearly converged to an optimal solution. Moreover, it can be concluded that for this particular problem 2000 generations would have been sufficient.

8

Sensitivity and Optimization Results and Discussion

This chapter presents the primary results of this thesis. First of all, the results of the sensitivity analysis are presented in Section 8.1. The results of the optimized Pareto front are discussed in Section 8.2 after which the distribution of the optimized observation schedule is discussed in Section 8.3. The improvement of the formal errors as a result of the optimized observation schedule will be discussed in Section 8.4. Finally, a discussion on the results is provided in Section 8.5.

8.1. Sensitivity Analysis

Before analyzing the results of the optimization of the JANUS observation schedule it is important to understand how the observation settings influence the condition number. Therefore, in this section the results of a sensitivity study are analyzed for the range of observation settings as presented in Section 6.4. Furthermore, as discussed in Section 6.4.5 only the variable under consideration is changed, the other independent variables are set to their corresponding baseline values. Note that the JANUS astrometry is chosen during the conjunctions which have the highest norm of the partial derivative of Io. In this way, the interpretation of the different JANUS settings is more straightforward as the observational geometry is not changed between different settings. However, adding more observations, means adding more observations that are inferior to the observations that are already considered, such that the stabilizing effect of the additional observations is limited. Finally, the results presented in this section should not be evaluated in an absolute sense but only to observe relative changes as a effect of different observational settings.

8.1.1. JUICE Orbit Determination Uncertainty and NavCam Settings

The conditional JUICE uncertainty determines to a large extend the uncertainties of the radiometric tracking observations (as discussed in Section 5.2 and shown in Figure 7.4) and to a lesser extend the uncertainties in the optical astrometry (where pointing errors dominate). In Figure 7.8(c) it was shown that limb-finding errors are at least two orders of magnitude larger than the spacecraft position uncertainty for space-based optical astrometry. Therefore it is expected that the chosen uncertainty case will have a substantial impact on the attainable condition numbers. Figure 8.1 shows the variation of the attainable condition numbers for the different JANUS and NavCam observation settings.

In Figure 8.1(a) it can be observed that improving the JUICE orbit determination conditional uncertainty (from case 5 to case 1) will increase the condition number of the normal equations (for all different JANUS observation settings). Furthermore, it can be noticed that as the spacecraft uncertainty deteriorates (moving from case 1 to case 5), the JANUS observations are more effective in reducing the condition number and that this improvement is more pronounced for higher number of JANUS observations. Both phenomena can be explained by the same principle. Improving the conditional orbit determination uncertainty of JUICE inherently improves the uncertainty of the radiometric tracking observations. Note that the instability originates from the chaotic distribution of the observations and the fact that the dynamics of Io and to a lesser extend Europa are observed through their signature on

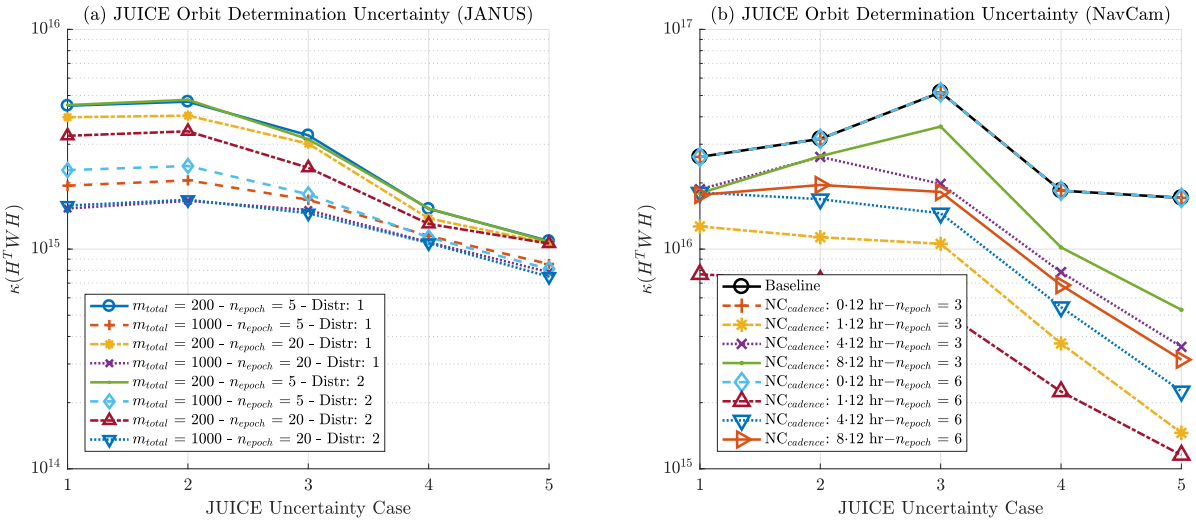

Figure 8.1: Sensitivity analysis of the condition number $\kappa(H^tWH)$ for the conditional uncertainty of the JUICE spacecraft. In the legend the m_{total} represents the total number of observations, n_{epoch} the number of observations per epoch, and the Distr the observation distribution case as discussed in Section 6.5. Note that distribution 1 has respectively 70 %, 20 %, and 10 % of the astrometric observations are acquired during the flyby, GCO/GEO5000, and GCO phase. Distribution 2 acquires all the astrometric observations during the flyby phase. The JUICE uncertainty cases are given in Section 6.4.1. Figure (a) does include JANUS astrometry at different observation settings (cadences and distributions), while the figure (b) represents the baseline scenario (radiometric tracking only) with and without the inclusion of NavCam observations at various cadences. The first entry of the legend denotes the number of NavCam tracking arcs every $n \cdot 12$ hr where the second entry denotes the number of NavCam observations per tracking arc. If $n = 0$ no NavCam astrometry is considered. Note that the baseline in figure (b) refers to the case in which only radiometric observations are considered.

the dynamics of Ganymede. Therefore, when the weights of the radiometric observations increase relative to the weights of the optical astrometry, the contribution of the optical astrometry in stabilizing the normal equations is reduced.

Observing the condition number representing only the radiometric tracking observables (baseline case as seen in Figure 8.1(b)) yields a remarkable conclusion. Improving the JUICE orbit determination uncertainty (moving from case 5 to case 1) first increases the condition number after which the condition number decreases. This behavior can be related to the method by which condition numbers are calculated, which becomes less accurate for close to singular matrices. Thus, for unstable systems (for which the matrix inversion is close to singular) the resulting condition number might also be inaccurate. This is confirmed by the fact that this behavior gradually reduces and vanishes in case more NavCam astrometry is added (more NavCam astrometry is used for the lines that are located lower in Figure 8.1(b)) and thus directly illustrates the stabilizing effect of adding optical astrometry. Moreover, the baseline case only considers radiometric tracking. Changing the JUICE uncertainty case does not affect the uncertainty of each observation similarly. Therefore, observations during certain weights (which are less suitable for constraining the dynamics of Io and Europa) are assigned a higher weight such that the condition number increases.

The behavior of the observation settings of the NavCam are quite similar to the observation settings for JANUS (comparing the different lines in Figure 8.1(a) and (b)), except that the effects are more pronounced for the NavCam (i.e. larger differences between the different lines can be observed). This is related to the fact the the NavCam is compared to the baseline solution (only radiometric tracking) where the JANUS solutions already consider NavCam astrometry such that the line representing the $4 \cdot 12$ hr - $n_{epoch} = 3$ case in Figure 8.1(b) is the baseline for the JANUS sensitivity analysis. The assessment of this behavior should be decoupled in further analyses. Nevertheless, the lower angular resolution limits the stabilizing effect of the NavCam with respect to JANUS. Finally, note that the NavCam astrometry epochs are randomly picked every $n \cdot 12$ hours such that the total stabilizing effect is not optimal.

For JANUS it can be seen that in case the total number observations m_{total} is constant, a higher number of observations per epoch n_{epoch} (i.e. clustering the observations around a smaller number of epochs) results in a slightly lower condition number. Therefore, it can be concluded that sequential imaging is more effective for JANUS which is further discussed in Section 8.1.4. For NavCam, however,

the total number of images is not kept constant while increasing the number of images per epoch such that the total number of observations increases while increasing the number of observations per epoch n_{epoch}. Therefore, it cannot be concluded that sequential imaging is beneficial for the NavCam.

8.1.2. VLBI Measurement Uncertainty & Observation Schedule

As shown by Dirkx et al. (2017), both the VLBI uncertainty and cadence have a substantial effect on the attainable formal errors of the initial states of the Galilean moons. This effect is especially important for the out-of-plane formal errors as this component is only weakly constrained in the Doppler observations. Similar as for the formal errors, the VLBI observation schedule is also expected to have some influence on the condition number. However, as the VLBI observations are all considered during the existing radiometric tracking arcs and lack Io tracking arcs, adding more VLBI data does not solve the underlying problem of the ill-conditioned normal equations matrix. Nevertheless, contrary to the other radiometric observations the VLBI data captures both the in- and out-of-plane dynamics. Therefore, adding more VLBI observations may improve the stability of the normal equations matrix as the out-of-plane dynamics of Especially Europa are better constrained.

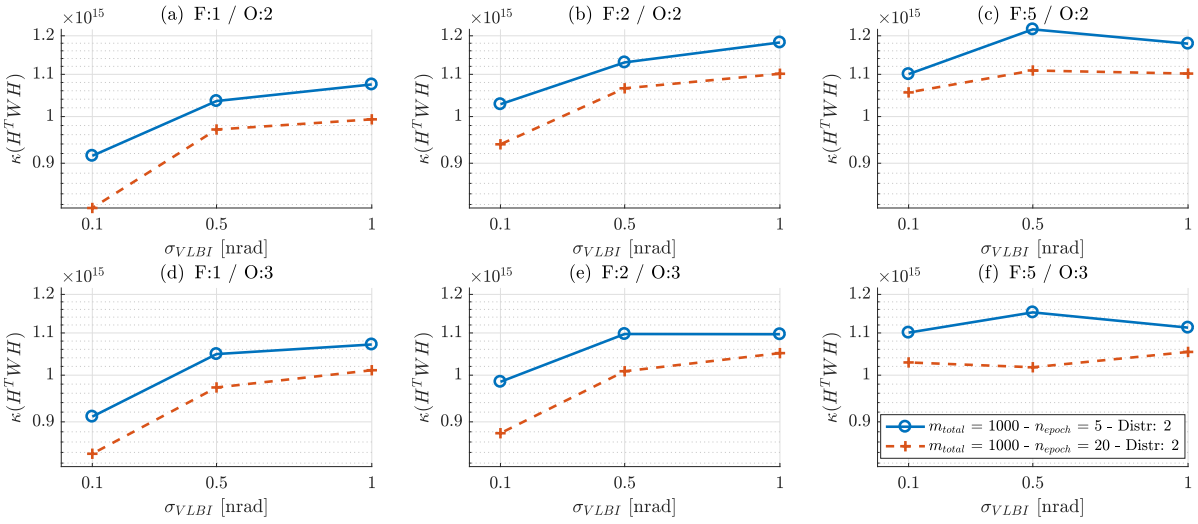

Figure 8.2: Sensitivity analysis of the condition number for the VLBI observation uncertainty and the VLBI observation schedule. The different lines represent different JANUS observation settings. m_{total} denotes the total number of observations, the n_{epoch} the number of observations per epoch, and Distr the distribution of the observation distribution case as discussed in Section 6.4.4. Note that here only case 2 is considered in which all JANUS astrometry is considered during the Jovian tour. The F and O denote the flyby and orbit VLBI cadence cases as discussed in Section 6.4.2. From left to right the VLBI flyby cadence is changed. From top to bottom the VLBI orbit cadence is changed.

At first, it should be noted that the differences between the different VLBI cases in Figure 8.2 are small compared to differences in Figure 8.1. Nevertheless, two types of trends can be observed in the data. First of all, Figure 8.2 (comparing the upper row of sub-figures with the lower row of sub-figures) shows that the effect of densifying the observation schedule during the Ganymede orbital phase has a limited effect on the condition number. This can be related to the underlying problem of the instability of the normal equations, which is related to, among others, the dense observation schedule during the Ganymede orbit phase and the fact that Europa and especially Io are observed only indirectly. Therefore, adding more observations referring to Ganymede in a phase which contains a large number of tracking arcs does not directly improve the observability of Europa and Io. This is explained by referring to Equation 5.4, in which the partial derivatives $\partial h_l^k / \partial \vec{x}(t_j)$ of the VLBI observations h_l^k are small for the states of Io and Europa in case the observation is related to Ganymede. Furthermore, the added observations will be most likely a close to linear combination of the existing rows in the observation matrix. This is worsened by the fact that during the Ganymede phase, the orbit geometry of JUICE changes from face-on to edge on such that the Doppler observations also constrain the out-of-plane dynamics of Ganymede. These results are in line with Dirkx et al. (2017) which do not show any improvements of the formal errors for Io and Europa in case the observation cadence during the Ganymede orbital tour is changed.

For a densified flyby observation schedule (Figure 8.2(a) and (d) in which a VLBI tracking arc is available every flyby) an improvement in the condition number is observed while increasing the measurement accuracy from $\sigma_{VLBI} = 1$ nrad to $\sigma_{VLBI} = 0.1$ nrad. This effect is less pronounced in case every second flyby has a VLBI tracking arc (Figure 8.2(d) and (e)) and almost absent in case no VLBI tracking arcs are available for Europa (Figure 8.2(c) and (f)). This behavior is related to the presence of the Europa tracking arcs which are crucial in improving the signature of the dynamics of Europa in the observations. Thus, these results do stress the need to retain VLBI tracking arcs for both Europa flybys. Moreover, the results presented in Figure 8.2 are in line with the results of Dirkx et al. (2017) which show that the formal error of Europa is improved in case the every flyby has a VLBI tracking arc and deteriorates in case no VLBI tracking arcs are available for Europa. More specifically, Dirkx et al. (2017) shows that the effect is also substantially more pronounced assuming a VLBI measurement uncertainty of $\sigma_{VLBI} = 0.1$ nrad compared to the VLBI measurement uncertainty of $\sigma_{VLBI} = 0.5$ nrad. Finally, no effect (an effect smaller than 5 %) is observable in case the VLBI measurement uncertainty is $\sigma_{VLBI} = 1.0$ nrad in the results of Dirkx et al. (2017) similar to the results presented here.

8.1.3. JANUS Operations

As discussed in Section 5.3, the uncertainty of the optical astrometry is governed by most importantly the pointing and fitting errors and marginally by the spacecraft conditional uncertainty. Therefore, the sensitivity of the condition number as a function of both associated independent variables is assessed in this section. The varied observation settings are the exposure length (influencing the pointing error), the upper limit for the limb fitting error which scales with the phase angle, and the resolution of the JANUS camera.

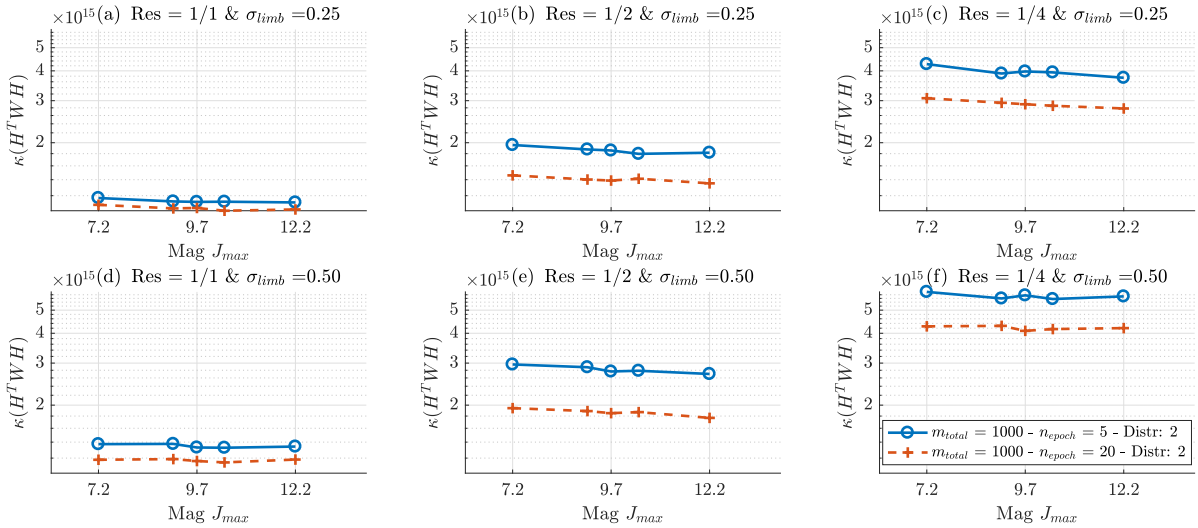

Figure 8.3: Sensitivity analysis of the JANUS instrument settings on the condition number. On the x-axis the apparent magnitude of the faintest visible star in the J band can be found. The values corresponds to the cases as presented in Section 6.4.3. From left to right the resolution of the JANUS camera is varied were Res gives the fraction of the total resolution (in one dimension). From top to bottom the limb-fitting error is increased from 0.25 pixels to 0.50 pixels. The first entry in the legend denotes the total number of observations, the second entry the number of observations per epoch, and the third entry the distribution of the observation distribution case.

Three conclusions can be drawn from Figure 8.3. First of all, it can be seen that the exposure time (related to the apparent magnitude which is visible in all figures) hardly influences the condition number. This is related to the number of stars which is currently overestimated. Consequently, the pointing error (as seen in Figure 7.8(c)) is an order of magnitude smaller than the fitting uncertainty. Therefore, the influence of the exposure setting is marginal in Figure 8.3 (note that a similar trend can be observed for all the lines). However, even when the number of stars would be accurately estimated, this effect is expected to be minor as the large field-of-view combined with the high resolution of JANUS makes this camera system less prone to pointing errors.

Secondly, it can be observed that increasing the maximum fitting uncertainty, which is a function of the phase angle, from 0.25 to 0.50 pixels (comparing the upper row of figures with the lower row

figures in Figure 8.3) will increase the attainable condition number. This is expected as increasing the limb fitting uncertainty will increase the total uncertainty, thereby reducing the weight for the optical astrometry and its effectiveness in reducing the condition number. However, note that this effect will be minor in case the images are acquired at low phase angles. This is because σ_{limb} scales with $\sin(\theta/2)$ where θ is the phase angle.

Finally, it can be seen that the attainable condition number increases substantially in case the resolution is deteriorated (comparing the different columns of Figure 8.3). This is expected as lower resolution makes the effect of the limb finding error more pronounced and also increases the pointing uncertainty.

8.1.4. JANUS Observation Schedule

Next to the JANUS observation settings, the sensitivity of the JANUS observation schedule is assessed in this section. Its behavior can be found in Figure 8.1 for a large number of settings and in Figure 8.2 and 8.3 in which only the number of the observations per epoch (clustering of the observations) is varied. From all these these figures a similar behavior can be observed and three conclusions can be drawn.

First of all, given a total number of observations (images), lower condition numbers can be found for clustered data (20 images per epoch) compared to data which is more widespread (5 images per epoch) which can be observed in Figure 8.1, 8.2, and 8.3. This can be related to the fact that a sequence of multiple observations is able to better capture the dynamical behavior compared to a set with limited observations. Alternatively (and more likely), it could be related to the fact that certain epochs are superior in reducing the condition number. In case more observations are clustered around such an epoch, the overall effectiveness of the space-based astrometric observations increases.

Secondly, it can be noted by comparing the different lines in Figure 8.1(a) that the influence of the distribution of the observations (considering type 1 and 2 as discussed 2.6.3) is minor in case of a total number of 200 observations to (almost) absent for 1000 observations. This is beneficial as the operational schedule during the orbital phase is tight and the implementation of optical space-based astrometry using JANUS is not desired as the JANUS camera is required for the mapping of the terrain of Ganymede.

Finally, from Figure 8.1(a) it can be concluded that increasing the number of optical astrometric observations reduces the condition number. This is expected as more observations increase the observability of the dynamics of especially Io and thus stabilize the system of normal equations more effectively and consequently reduce the condition number.

8.2. Optimization Results

This section shows the Pareto front (distribution of solutions with the optimal combination of both the condition number and the formal error as discussed in Section 6.1) for the optimization case as discussed in Section 6.5. Note that the resulting parameter space (optimized epochs for JANUS optical astrometry) will be further discussed in Section 8.3.

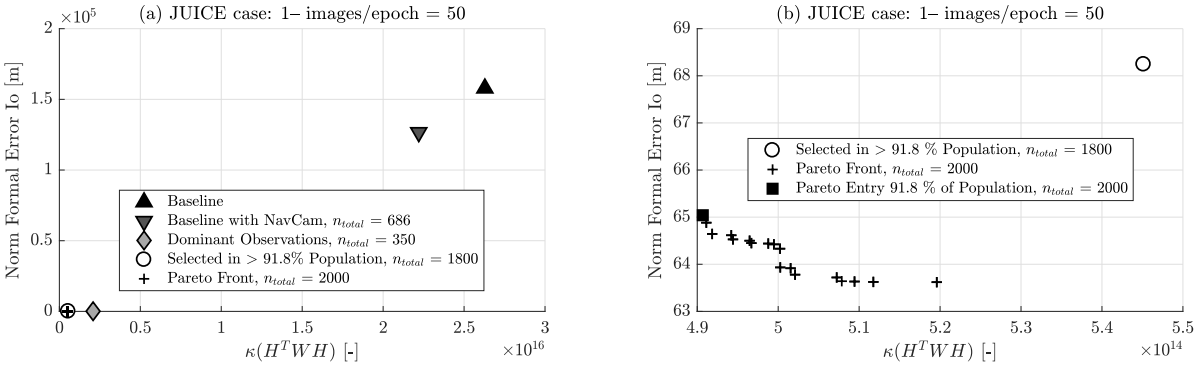

Figure 8.4: Pareto front with on the x-axis the condition number $\kappa(H^TWH)$ and on the y-axis the norm of the formal error of the position of Io. Figure (a) shows how the Pareto front is approached starting with the baseline case (using no optical astrometry). n_{total} denotes the number of astrometric observations. Note that all data points except the baseline case include 686 NavCam observations. Figure (b) shows the resulting Pareto front. The white circle represents the same point in both figure (a) and (b). Finally, the black square denotes the entry on the Pareto front to which 91.8 % of the population is converged.

Figure 8.4(a) shows how the Pareto front is approached starting with the baseline case (upper black triangle) in which no optical astrometry is included. Including NavCam optical astrometry (lower grey triangle) only marginally reduces the condition number. This is related to the fact that the NavCam epochs are randomly picked as well as to the lower resolution of the NavCam which reduces its capability in reducing the condition number. The grey diamond represents the case in which only the dominant JANUS observations (only 350 observations) as established by the NSGA-II algorithm are included. Dominant observations are observation epochs that are selected by the NSGA-II algorithm more than once in a single individual of the total population. Figure 8.4(a) shows that the dominant observations substantially reduce both the condition number and norm of the formal error of Io. Finally, the white circle in Figure 8.4(a) and (b) represents the epochs (1800 observations) to which 91.8 % of the population is converged. This point almost coincides with the Pareto front. The remaining offset is reduced in case the dominant observations are considered twice.

Note that in reality observation cannot be selected more than once. Note, however, that the time between two adjacent images is currently 120 seconds, while for the Cassini mission the smallest time between two adjacent optical observations is only 18 seconds. Therefore, an tracking arc can be considered twice in reality by reducing the time between two adjacent observations.

Figure 8.4(b) shows the complete Pareto front as well as the entry on the Pareto front to which 91.8 % of the population is converged. Note that the points on the resulting Pareto front are extremely clustered. This is related to the fact that 91.8 % of the observations is clustered to the black square. Furthermore, the remainder of the individuals (which are not converged) on the Pareto front contain a minimum of 67.5 % of the observations from the converged 91.8 %. Therefore, the remainder of the individuals on the Pareto front include the dominant observations. Thus changing the remaining 32.5 % of the observations for the individuals which are not converged to the black square will only marginally affect both the condition number and the norm of the formal error of Io. Thus the resulting Pareto front will be extremely clustered.

Figure 8.4(b) shows that in case a large number of observations is used (around 2000, which represents an equal number of images compared to the Cassini mission scaled by the duration of the Jovian tour) the condition number can be reduced by approximately two orders of magnitude but not below $\kappa_{max} = 4.50 \cdot 10^{14}$ which is required to retain at least one significant digit. Note that, however, the condition number shows a large sensitivity to the settings used. This is especially true for the JUICE conditional uncertainty as discussed in Section 8.1.1. Therefore, for the actual settings the condition number might be either larger (e.g. in case the uncertainty of the astrometry is overestimated) or smaller (e.g. in case the JUICE conditional uncertainty is larger). Therefore it can only be concluded that the condition number can be substantially reduced close to a value which is required to retain at least one significant digit.

This Pareto front is acquired using JUICE uncertainty case 1 which poses the largest challenge in reducing the condition number as discussed in Section 8.1.1. This is related to the fact that a low conditional uncertainty of JUICE reduces the relative contribution of the JANUS optical astrometry as the radiometric tracking observations are assigned a higher weight (a low uncertainty corresponds to a high weight). Thus, deteriorating the JUICE conditional uncertainty will reduce the attainable condition number. However, the resulting formal errors will be higher.

8.3. Analysis of the Resulting Observation Epochs

For the observation planning of the JUICE mission it is important to know when the JANUS camera should be used for optical astrometry such that the observation schedule, data downlink, etcetera can be planned accordingly. Section 8.3.1 discusses the general characteristics of the optimized solution in the parameter space (epochs for JANUS astrometry). A more detailed analysis to the events for which a large number of optical astrometry is selected by the NSGA-II algorithm is provided in Section 8.3.2.

8.3.1. General Characteristics of Optimized Solution in Parameter Space

Figure 8.5 provides insight in the distribution of the optimized epochs among both the moons and the different mission phases. The most important aspects of Figure 8.5 are summarized in Table 8.1.

Comparing Figure 8.5(a) and (c) it can be seen that no dominant observations are selected for Europa and that most of the selected epochs for Io are located in or close to the Europa science phase (this might be difficult to observe in Figure 8.5(a) where many markers are located above eachother).

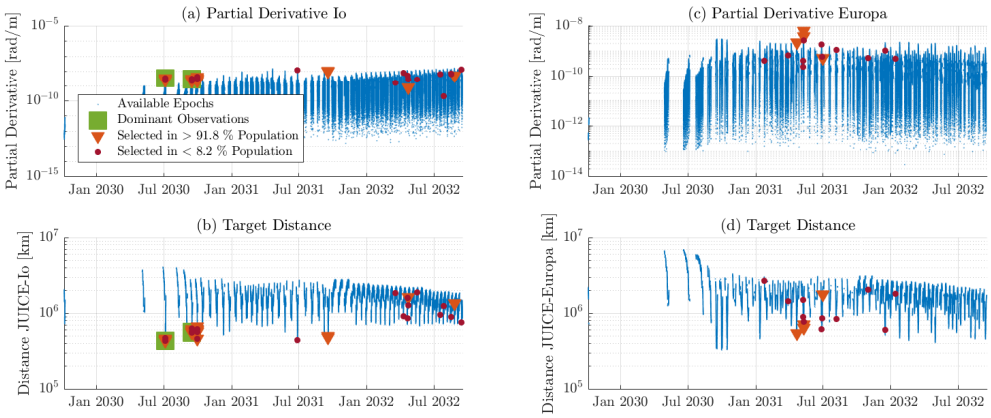

Figure 8.5: Figure (a) and (c) represent the norm of the partial derivative of the lateral position (both α and δ) with respect to the position of respectively Io and Europa while figure (b) and (d) represent the distance between the JUICE spacecraft and respectively Io and Europa. Note that the markers in figure (a) and (b) refer to Io optical astrometry and the markers in figure (c) and (d) refer to Europa optical astrometry. The dominant observations (green squares) refer to the observations that are selected more than one time in a single individual by the NSGA-II algorithm. The orange triangles represent the epochs of the converged individuals (black square on the Pareto front in Figure 8.4(b)). The red circles represent the epochs which are selected by the remaining 8.2 % of the individuals on the Pareto front.

Furthermore, observing the square and triangular markers in Figure 8.5 it can be observed that most of the epochs belonging to the converged point on the Pareto front (black square in Figure 8.4(b)) which are represented by an orange triangles have both a high norm of the partial derivative the lateral position with respect to the position of Io or Europa as well as a close separation to the observed target (either Io or Europa). Finally, it can be observed that the observations selected in the non converged part of the Pareto front (represented by the + signs in Figure 8.4(b)) do not necessarily have a high partial derivative of the observation with respect to the state of the target body or a low distance between the spacecraft and the target body. Therefore, these observations are associated with a lower weight and are slightly less effective in stabilizing the system of normal equations (or increasing the number of linearly independent rows). Nevertheless, these observations provide a better temporal signature of the dynamics of Io and Europa due to fact that these observations are more evenly distributed among the JUICE trajectory such that the resulting formal errors are marginally improved (which is observed in Figure 8.4(b)).

Table 8.1: This table summarizes the most important results found in Figure 8.4. Note that the bulleted entries are part of the Io optical astrometry. All percentages refer to the total number of observations epochs (40 epochs at 50 images/epoch). $\mu(\sigma_{JANUS})$ is the average JANUS uncertainty during a specific event. $\mu(d_{JUICE-target})$ denotes the average distance between the JUICE spacecraft and the target body. T_{rep} refers to the period of repetition of the Laplace resonance as shown in Figure 2.3. Subsequently, the conjunction which belongs to the respective fraction of T_{rep} is given in the last column. Where to two letters denote the first letter of the respective moon.

	Percentage of Total [%]	$\mu(\sigma_{JANUS})$ [km]	$\mu(d_{JUICE-target})$ [km]	Fraction of T_{rep} [-]	Conjunction
Io	90.0	1.42	$5.58 \cdot 10^5$	-	-
• *3G3*	37.5	1.41	$4.34 \cdot 10^5$	0.51	IG
• *6E1*	27.5	1.26	$5.64 \cdot 10^5$	0.72	IE
• *7E2*	15.0	1.33	$5.67 \cdot 10^5$	0.74	IE
• *Other*	10.0	2.03	$9.82 \cdot 10^5$	-	-
Europa	10.0	3.72	$9.10 \cdot 10^5$	-	-

The most important results of Figure 8.5 are summarized in Table 8.1. Firstly, it can be directly observed that 90 % of the epochs are used for Io astrometry and only 10 % of the epochs is used for Europa astrometry. These results are in line with the results of Dirkx et al. (2017) which conclude that the optical

astrometry is crucial for Io and only of secondary importance for Europa. This is also apparent while comparing the average uncertainty and target distance between the astrometry for both moons in the third and fourth column of Table 8.1. The corresponding values are somewhat lower for Io indicating that the optimized epochs for Io are more ideal. A low uncertainty σ_{JANUS} and distance to the target $d_{JUICE-target}$ is directly associated with a higher partial derivative in the weighted normal equations matrix (due to the high weight for a low uncertainty). However, the fact that only 10 % of the optimized epochs are selected for Europa astrometry might be partially related to the fact that norm of the formal error of Europa is not an objective variable such that the Europa astrometry does not directly benefit the overall performance. Nevertheless, Europa optical astrometry is at least of secondary importance considering the optimization of the condition number.

The target distance has a dual influence on the weighted partial derivatives. Firstly, the positional uncertainty is lower for a close-by object as the angular uncertainty does not vary with the distance between the spacecraft and the target satellite, such that the positional uncertainty scales linearly with the distance between the spacecraft and the observed moon. Secondly, when a satellite is observed at a small distance, the sensitivity of the partial derivative of the lateral position with respect to the initial state of the satellite increases, resulting in higher unweighted partial derivatives. This can be explained by observing Equation 5.4 which computes the rows of the normal equations matrix. In case the lateral observation h_l^k is acquired at a relatively small distance from the target satellite (either Io or Europa), the sensitivity of the observation with respect to the state of the target satellite $\partial h_l^k / \partial \vec{x}(t_j)$ increases. The sensitivity of the current state of the satellite with respect to the initial state vector $\partial \vec{x} / \vec{c}(t_j)$ is mostly dependent on the time passed since t_0 which is related to the fact that an different initial state will have a more pronounced effect after a longer amount of time. Thus an astrometric observation acquired at a small distance with respect to the target satellite will have a higher information content and a more pronounced signature of the dynamics of the observed moon. Therefore the observability of the dynamics of states of the moons is improved for observations with higher entries in the corresponding row of the normal equations matrix.

Notice that the positional uncertainties $\mu(\sigma_{JANUS})$ provided in Table 8.1 are quite optimistic. This is a result of the adopted model which does not account for the variable distance at which the images are acquired as proposed by Antreasian et al. (2005) to make sure the results were in line with Tajeddine et al. (2015). However, whether these results are actually attainable for JANUS requires further research to, among others, the state-of-the art with which the uncertainty of a close-by limb can be determined. These recommendations are listed in more detail in Chapter 9. In case the actual positional uncertainties are higher, the resulting condition number will also be higher (see Section 8.1.3 in which the influence of the larger limb-fitting error assessed). However, this effect is relatively small. Nevertheless, even in case the limb-finding uncertainty increases substantially during images which are acquired at a close distance, Figure 7.6(b) (in which the model by Antreasian et al. (2005) is implemented) shows that the positional uncertainty is minimum during the point of closest approach. Thus, as the results presented in Figure 8.5 show a clear preference for close-by imaging, the optimized epochs are not expected to change significantly in case a different weight model is adopted.

8.3.2. Characteristics of Clustered Optical Astrometry Epochs

Table 8.1 shows that a large number (80 % of the total selected epochs) of optical astrometric observations are clustered around the 3G3, 6E1, and 6E2 flybys. Note however that no optical astrometry is performed within 24 hours around the time of closest approach of a flyby. Nevertheless, these clustered observations are characterized by a low target distance and a low positional uncertainty (these go hand-in-hand). Furthermore, it can be observed that although the specific geometry of the inner Galilean moons (characterized by T_{ref} in Table 8.1) is not directly influencing the optimal JANUS astrometry epochs, it does have an influence on the proximity of Io to JUICE during a flyby. It can be noticed that for the JANUS astrometry epochs around Ganymede flyby, Ganymede and Io are close to conjunction. This directly implies that the separation between Ganymede and Io (and thus between JUICE and Io) is small. Similar behavior can be observed for JANUS astrometric observations which are located near the Europa flybys.

To show that this behavior is not related to the absolute observation uncertainty but only to the observational geometry, Figure 8.6 shows the norm of the unweighted partial derivatives of the positions of (a) Io, (b) Europa, and (c) Ganymede. It can be observed that the JANUS epochs selected by the optimization algorithm do all have high partial derivative for the position of all the three inner Galilean

moons. Note that this figure only shows the astrometry for Io during the three flybys, as 80 % of the total available observations converged to these events. However, the optimized Europa epochs as well as the remainder of the Io epochs (except for three epochs for which no clear logic was identified) show similar behavior which can be observed in Figure 8.5(a) for Io and Figure 8.5(b) for Europa.

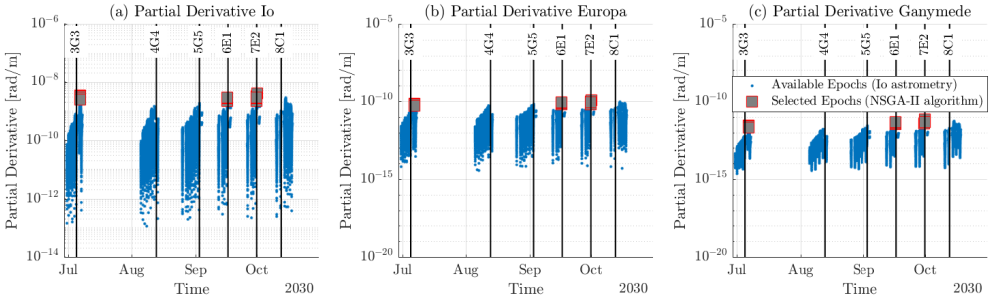

Figure 8.6: The norm of the unweighted partial derivatives in radians per meter of the positions of Io, Europa, and Callisto. The partial derivatives refer to the JANUS astrometry of Io. The red squares denote the selected epochs for JANUS astrometry as found by the optimization algorithm for the converged point on the Pareto front. Note that the y-axis has a different scale for Io compared to the scale used for Europa and Ganymede. The black lines denote the flybys where the ID of the flyby is denoted by a two numbers and one letter. The letter represents the first letter of the flyby moon. And the first and second number represent respectively the total flyby count and the flyby count for the respective moon. The x-axis for all figures denotes the date in UTC.

As discussed in Section 8.3.1 the partial derivative $\partial h_l^k / \partial \vec{x}$ increases in case the distance between the observer and the target is small. In addition, Figure 8.6 shows that the norm of the partial derivatives of Io is at least an order of magnitude higher than for Europa and Ganymede. The baseline case, including only radiometric tracking observations of Europa, Ganymede, and Callisto, however, has low entries in the H matrix for columns representing the state of Io as $\partial h_l^k / \partial \vec{x}_{Io}$ is low in case Io is not observed directly. Consequently the matrix product $H^T W H$, required to obtain the covariance matrix P using Equation 5.7, has relatively similar rows (which are thus linearly dependent) for the state of Io. Therefore, the rank of matrix is will be smaller than the number of variables to be estimated such that the $H^T W H$ matrix is singular which results in high condition numbers (as the singular matrix $H^T W H$ needs to be inverted to acquire P). Thus, observations which have a high partial derivative of Io in the rows of the H matrix make the rows (representing the initial state of Io) in the matrix $H^T W H$ less linearly dependent. Subsequently, the rank increases which results in a lower condition number and thus a more stabilized system of normal equations.

To gain more insight to the mechanism that causes the partial derivatives to be high, the image properties (target distance, fraction of image that is filled, the phase angle and the observation uncertainty in pixels) are shown in Figure 8.7. Similar to Figure 8.6 this figure focuses on the Europa science phase considering only Io astrometry as 80 % of the optimized epochs were represented by those criteria.

Figure 8.7(a) stresses again that a close proximity to Io is required to reduce the condition number for the estimation of the ephemerides of the Galilean moons. Imaging close-by satellites, however, result in a high fraction of the image that is filled by the moon, which can be observed Figure 8.7(b). Nevertheless, note that the maximum fraction of the image that is filled by Io is less than 0.3 which is substantially lower than maximum allowed fraction of $1/\sqrt{5}$ as required by Boutonnet et al. (2018), such that astrometric reduction is still possible. An advantage of observing close to the flybys is that the trajectory design of JUICE is chosen in such a way that the illumination conditions are favorable for, among others, mapping of the surface of the moons. This means that low phase angles are observed (see Figure 8.7(c)) during the optimized JANUS epochs which is beneficial in terms of astrometric reduction of the images and which will result in lower limb-fitting uncertainties. Finally, observing the observation uncertainty Figure 8.7(d), shows that the proximity to the target is more important than the observation uncertainty in pixels. This is especially visible for the JANUS epochs which are located in the proximity of the 3G3 flyby. Note that for these epochs, the observation uncertainty is somewhere halfway between its upper and lower value. Nevertheless, the close proximity to Io results in a lower positional uncertainty such that these epochs are favorable in reducing the condition number of the normal equations.

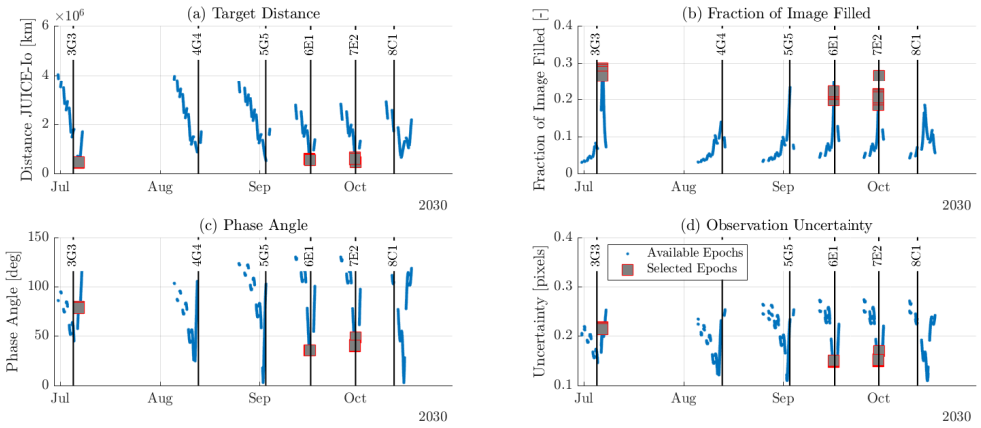

Figure 8.7: (a) The target distance between the spacecraft and the observed moon in kilometers, (b) the fraction of the images which is filled by the moon in one dimension referring to the diameter of the moon. Furthermore, the phase angle (c) is given in degrees and the observation uncertainty (d) in pixels. The blue dots denote the available epochs where the red boxes show the epochs which are selected for JANUS astrometry by the optimization algorithm. All selected epochs refer to optical astrometry of Io. The x-axis for all figures denotes the date in UTC.

8.4. Analysis of the Formal Errors

This section discusses the improvement of the formal errors as a result of implementation of the optimized JANUS observation schedule (see Section 8.2). The formal errors for the baseline case (without optical astrometry) as well as the relative improvements using the optimized JANUS epochs are presented in Table 8.2. As no biases are estimated the baseline formal errors of especially Europa are severely underestimated. For Ganymede the effect is limited as the data which provides the best signature of the dynamics of Ganymede is acquired during the Ganymede orbital phase in which the conditional uncertainty is assumed to be equal to the marginal uncertainty (as discussed in Section 5.2). Therefore the effect of not estimating observational biases is less pronounced.

Table 8.2: The baseline column presents the formal errors in case no optical astrometry is present in meters. Note that as no observation biases are estimated the formal errors of especially Europa severely underestimated. The relative improvement is given for both the dominated JANUS epochs (observation epochs which were selected twice by the NSGA-II algorithm) as well as for the optimized epoch to which 91.2 % of the population has converged. The improvement is given as a percentage of the baseline formal errors. Note that the formal errors of Callisto are not included in this table as these are not improved beyond 5 % by the optical astrometry which is related to the limited dynamic coupling between Callisto and the other Galilean moons.

	Io		Europa		Ganymede	
	IP	OP	IP	OP	IP	OP
Baseline Formal Error [m]	378.8	246.1	30.2	17.8	7.2	5.5
Improvement [%]						
NSGA-II Dominated JANUS Epochs $n = 350$	−73.5	−85.4	−27.7	−42.1	−64.6	−77.4
NSGA-II Epochs JANUS $n = 2000$	−83.3	−93.9	−35.0	−41.9	−70.7	−86.1

Note that for the optimized solution, the condition number ($\kappa = 4.9 \cdot 10^{14}$) is not below the threshold required to retain at least one significant digit ($\kappa_{max} = 4.50 \cdot 10^{14}$). However, due to the large uncertainties in, among others, the conditional uncertainty of JUICE and the attainable accuracy of the JANUS camera, the uncertainty in the computed condition number is too large to draw an general conclusion regarding the amount of significant digits that can be retained (see also Section 8.2).

Table 8.2 shows the largest improvement of the formal errors for Io, which is expected as using the optical astrometry enables direct observations of Io which are absent for the radiometric tracking observables. Note that especially the out-of-plane component of the Io uncertainty is improved. The relative improvement with respect to the in-plane component of the position of Io can be related to the

fact that optical astrometry only measures the lateral position of Io. However, the with edge-on viewing geometry the in-plane dynamics are more accurately observed by Doppler observations which are not present for Io, hence the relatively improved in-plane position of Io.

For Europa, however, the improvement is less pronounced compared to Io (see Table 8.2). This is most likely related to the fact that precise radiometric tracking data is already included in the baseline solution for Europa. Furthermore, as only 10 % (as discussed in Section 8.1.3) optical astrometric observations is devoted to Europa, the effect is expected to be less pronounced. Furthermore, the baseline formal errors for Europa are already substantially lower compared to Io (which is mostly related to the fact that no observation biases are estimated). Finally, the improvement of the formal errors in the out-of-plane component of Europa is larger than the improvement of the in-plane formal errors. This is related to the fact that the out-of-plane dynamics have a larger signature the astrometric observations compared to the in-plane dynamics which are better constrained in the Doppler-observations.

Table 8.2 shows that the formal errors of Ganymede are also substantially reduced, especially in the out-of-plane components. As no direct optical astrometry was included for Ganymede, this effect can be fully attributed to the fact that the optical astrometry of Io and Europa can be used to provide an additional signature of the dynamics of Ganymede in the observed dynamics of both Io and Europa. The out-of-plane formal error of Ganymede can be substantially reduced by decorrelating the limited dynamic coupling by the Laplace resonance in the out-of-plane component.

Finally, for Callisto no improvement is observed, and is therefore not included in Table 8.2. This is directly related to the fact that Callisto is not part of the Laplace resonance such that its dynamics is not correlated to the dynamics of the inner three moons. Therefore, accurate radiometric tracking enables accurate determination its initial position.

Note that the formal errors as presented in this section are generally optimistic, and the true-to-formal error ratio for the determination of planetary ephemerides using spacecraft tracking generally on the order 10. The latter is a result of the weighting matrix which might contain results from initial judgment such that the formal errors are not valid in a statistical sense but rather show the relative contribution or performance of the optical astrometry (Schutz et al. 2004). Furthermore, the fact that no biases are estimated will result in substantially higher formal error for especially Europa and to a lesser extend Ganymede. Therefore, the results presented in this section should only be interpreted in a relative manner. In addition, the relative contribution of the optical astrometry for Europa and Ganymede might be less pronounced. The results for Io, however, are not expected to change substantially as its signature is mostly determined using the optical astrometry. In optical astrometry the effect of the biases is limited as the spacecraft position uncertainty only marginally affects the total observational uncertainty.

8.5. Discussion on the Results

From the results presented in the previous sections it can be observed that for the current observation settings and uncertainty models the condition number could not be reduced to a level which is required to retain at least one significant digit. This does, however, not mean that such condition numbers are not attainable using optical space-based astrometry. As shown in Section 8.1, both the conditional uncertainty of the position of JUICE as well as the magnitude of the limb-fitting uncertainty have a large impact on the attainable conditions numbers. As both the actual uncertainty in the orbit determination of JUICE and the uncertainty with which the center-of-figure of the limb can be determined are not exactly known beforehand, it is difficult to obtain an accurate estimation on the attainable condition number (and thus the number of significant digits that can be retained) without, among others, a more accurate spacecraft position uncertainty.

The condition number is shown to be optimal for close-by astrometry of Io. As discussed in Section 5.3.2, accurate fitting of the apparent limb is more difficult for a satellite with a larger apparent diameter. Thus, the uncertainty in the astrometry for especially the epochs selected by the optimization algorithm might be underestimated, reducing the stabilizing effect. This effect, however, is slightly less important for images with low phase angles, for which the center-of-figure of the limb can be determined more accurately (which is the case for most of the selected epochs as shown in Figure 8.7). Furthermore, even in case the uncertainty of the astrometric observation scales with the apparent diameter (thus accounting for the increasing uncertainty in case the image is acquired at a close proximity), the positional uncertainty is minimum at the point of closest approach as confirmed by Figure 7.6(b). Nev-

ertheless, the need for close-by astrometry poses an additional challenge in stabilizing the system of normal equations.

The uncertainty model that is used for this thesis, assumes that the refined limb finding algorithm as used by Tajeddine et al. (2015) substantially reduces the uncertainty in finding the center-of-figure of a satellite. In this algorithm, the sensitivity of detecting the terminator of the apparent limb (as discussed in Section 4.4) is increased, especially for higher phase angles. However, for future work the performance of this refined limb finding for especially close-by images should be assessed. Nevertheless, the results of Tajeddine et al. (2015) (in which the limb-fitting was performed with a higher sensitivity) show an uncertainty ceiling at approximately one arcsecond which corresponds to approximately 0.8 pixels (refer to Appendix A.10 for the actual data). This shows that even images for which a large part of the image is occupied by the satellite can be fitted with substantially improved accuracy compared to the variable weight model proposed by Antreasian et al. (2005) as shown in Figure 7.6(a). The uncertainty ceiling, however, is substantially larger than the limb finding uncertainty in this thesis (see Figure 7.8(c)). This is partially related to the small field-of-view of the cassini NAC such that the pointing errors dominate which is different compared to JANUS and NavCam in which the limb-finding uncertainty is expected to be dominant (see Figure 5.2).

The model used throughout this thesis assumes the average limb-finding uncertainty in pixels, such that the uncertainty as presented in this thesis might be underestimated, especially for the close-by astrometric observations as also discussed in the previous paragraph. However, as discussed in Section 8.3.1, the qualitative analysis of the observation epochs is not expected to change substantially in case of a different limb-finding uncertainty.

The optimized observation schedule shows a high concentration of epochs during which JANUS optical astrometry is required shortly after a flyby. Such a schedule is not ideally in terms of operations which is related to the high data volume associated with JANUS astrometry. JUICE Science Study Team (2014) show a cumulative data volume of 76 Gigabits during a Europa flyby. Assuming the JANUS observation epochs shortly after the 6E1 flyby are saved with monochrome color at 8 bits per pixel (e.g. Beesley 2001) and a data compression ratio of 8/5 for lossless compression (as full quality of the image is required for accurate astrometric reduction) (Beser 1994), the total data volume associated with this tracking arc is roughly 8.3 Gigabits. This comprises roughly one tenth of the total data volume of the Europa flyby which poses an high demand on the operational flexibility of the mission designers. This is generally not an issue for many missions as the astrometric observations are more evenly distributed over the total mission. Furthermore, the required pointing for space-based astrometry might conflict with required pointing of the high gain antenna for down-link to Earth.

It should thus be assessed how the condition number is affected while reducing the total number of astrometric observations close to one of the three flybys. Figure 8.4(a) shows that only assessing the dominant observations (which are selected twice for some individuals in the total population of the optimization framework) has already a substantial stabilizing effect and only has a data volume of 5.2 Gbits divided over two arcs. Thus bearing in mind the fact that astrometry for Io is optimal during the closest approaches, a reduced observation schedule can be proposed with a close to similar stabilizing effect but at a substantially lower data volume.

Finally, the optimized results might be different in case more model parameters are estimated. Especially, when the parameter (k_2/Q) is considered (which is the combination of the tidal Love number k_2 and the tidal lag angle Q). (k_2/Q) has a secular effect on the semi-major axis and eccentricity (as shown in Equations 2.9 and 2.10). Thus the mean motion will change such that the effect on the longitude will be cumulative (Lainey et al. 2009, supplementary information). Therefore the signature of tidal dissipation on the orbit increases quadratically in time (Dirkx et al. 2016). This means that the signature of the tidal dissipation in Io on the dynamics will be unobservable for the optimized JANUS astrometric observations which are concentrated around the Europa science phase. This advocates the inclusion of Earth-based astrometry (which is available over a period of 120 years) which enables to observe a signature which is approximately 1200 times as strong compared to the signature during the nominal duration of JUICE (Dirkx et al. 2016). Finally, as proposed by Dirkx et al. (2017) the inclusion of Earth-based astrometry could be beneficial in coupling the signatures on Europa provided by both JUICE spacecraft and the Europa Multiple Flyby Mission (Lam et al. 2018). Using the Europa observations of both missions enables to observe a signature of the dynamics of Europa which is much wider spaced in time (Dirkx et al. 2017).

9

Conclusions and Recommendations

In this chapter the research questions as posed in Chapter 1 will be answered in Section 9.1. Furthermore, recommendations for future work will be given in Section 9.2.

9.1. Conclusions

For this thesis one research question was posed which is divided into three sub-questions. To a retain a logical structure, the conclusions to the sub-questions will be discussed before the main question. The conclusions to the sub-questions will be given in Section 9.1.1 after which the conclusions to the main research question will be given in Section 9.1.2.

9.1.1. Sub-Questions

The sub-questions as posed in Chapter 1 will be discussed below.

1. **What is the impact of the range of illumination conditions of the different Galilean moons on the uncertainty of the observations (right ascension and declination) related to JUICE-based optical astrometry of the different Galilean moons?**
   The illumination condition of the moon, represented by the phase angle (where a completely illuminated moon has a phase angle of 0° and a moon which is not visible has a phase angle of 180°), has an impact on the accuracy with which the center-of-figure of the moon can be determined. The uncertainty in the determination of the center-of-figure, along with the pointing uncertainty and the spacecraft position uncertainty, determine the total uncertainty with which the lateral position of a moon can be determined using JUICE-based optical astrometry.
   Due to the relatively large field-of-view of both JANUS and NavCam, which enables the detection of more background stars (see Table 5.3), the expected pointing error for JANUS is substantially lower than for the Cassini NAC (see Figure 5.2). Moreover, the derivative of the pointing uncertainty with respect to the number of stars is lower for JANUS. Therefore, the amount of stars in field-of-view has a less pronounced effect on JANUS compared to Cassini NAC (see Figure 5.2). As a result, the uncertainty with which the center-of-figure can be determined is substantially more important for JANUS (see Figure 7.8) compared to the pointing uncertainty.
   Studies using space-based astrometry of especially the Saturnian moons by the Cassini spacecraft showed that the center-of-figure was determined with a positive bias in the direction of the Sun. This implies that a large phase angle results in a higher uncertainty in the location of the center-of-figure. The latter was confirmed in literature by generating artificial images for different phases of a moon. The resulting center-of-figure clearly showed a bias in the direction of the Sun. However, more recent literature showed that by increasing the sensitivity of the limb-finding algorithm, this bias was no longer present (see Figure 7.7). The latter, however, does not mean that the uncertainty is indifferent of the phase angle of the moon. Therefore, this effect was modeled to a limited extend such to prefer images with a lower phase angle (of which a larger part is illuminated by the Sun).
   Another important factor which determines the accuracy by which the center-of-figure of the moon

can be determined is the proximity to the moon, where a close proximity results in a higher uncertainty in the determination of the center-of-figure of the moon (see Figure 7.6(a)). Models accounting for this behavior, however, provided substantially higher uncertainties compared to recent literature (see Figure 7.6(a) and (c)). To fully account for the proximity to the moon under consideration, the model proposed should be fitted through multiple data-sets. To conclude, the illumination condition has some influence on the uncertainty (and thus the variance) of the right ascension and declination of the observed moon. However, detailed assessment of additional data provided by earlier studies showed this influence to be limited. Furthermore, the proximity might have a more pronounced influence compared to the illumination conditions.

2. **What is the impact of the optimization of the observation schedule of the JANUS instrument to complement the JUICE radiometric tracking data on the condition number of the normal equations?**
   With the given settings (especially the low conditional uncertainty of JUICE), inclusion of JUICE-based optical astrometry to complement the radiometric tracking data resulted in a reduction of the condition number by almost two orders of magnitude (from 10^{16} to 10^{14} as shown in Figure 8.4). However, the minimum condition number found in this thesis is not sufficient to retain at least one significant digit in the resulting estimated parameters in case double precision is used. The condition number, however, showed a large dependency on both the limb-finding uncertainty and the conditional uncertainty of the JUICE spacecraft (see Figure 8.1 and 8.3). Thus, the resulting condition number can be either improved or deteriorated in case the real values for these parameters are used.
   The optimized epochs for JUICE-based astrometry, as selected by the optimization algorithm, were found to be preferentially distributed around the closest approaches of JUICE with respect to Io (see Figure 8.5 and Table 8.1). This is related to (1) the higher sensitivity of the partial derivatives of the right ascension and declination with respect to the initial states of the moons and (2) the lower positional uncertainty of the astronomic observations which scales with the distance to the moon that is observed.
   It was found that 80 % of events are located close to the flybys 3G3, 6E1, and 7E2. These flybys were closely located in time to a conjunction (the moment in time where two moons line up with the central planet) of Io and the moon for which a flyby was performed (see Figure 8.5 and Table 8.1). This specific geometry results in a close approach with respect to Io. Furthermore, the astrometry of Europa was found to be of secondary importance in reducing the condition number. This is related to the fact that only 10 % of the optimized epochs were selected for Europa (see Table 8.1).
   Certain epochs close to both the 3G3 and 6E1 flybys were chosen more than once by the NSGA-II algorithm and were considered to be dominant. Only considering these dominant epochs establishes a large part of the improvement of the condition number at the expense of only a fraction of the total observations (see Figure 8.4).

3. **What is the impact of optimization of the observation schedule of the JANUS instrument to complement the JUICE radiometric tracking data on the formal errors of the ephemerides of the Galilean moons given that the condition number of the normal equations is sufficiently low?**
   As previously discussed, for the given observational settings, the condition number is not below the threshold required to retain at least one significant digit (note that the uncertainty on the condition number is substantial). However, substantial improvements on the formal errors as a result of adding space-based astrometry were observed. It was found that optimizing the observation schedule of the JANUS camera is especially beneficial in reducing the formal errors of Io (see Table 8.2), which is directly related to the lack of direct radiometric tracking of the dynamics of Io. This improvement is slightly more pronounced in the out-of-plane component as this component is well constrained by astrometric observations. Moreover, the signature of the in-plane dynamics is better constrained by Doppler observations, hence the lower improvement of the formal error of the in-plane position of Io.
   For Europa, the enhancement of the formal errors is less evident (see Table 8.2). This is associated with limited optical astrometry which was selected for Europa by the NSGA-II algorithm (see Figure 8.5 and Table 8.1) Furthermore, compared to Io, its dynamics are already better con-

strained in the radiometric tracking observations.
The formal errors of Ganymede are slightly improved in both the in-plane and out-of-plane component (see Table 8.2). As no direct optical astrometry was used for Ganymede, this effect is related to the signature of its dynamical behavior in the dynamics of especially Io and to a lesser extend Europa.
Finally, a large part of the improvement was established by only using the dominant epochs for optical astrometry (similar to the condition number) at a fraction of the number of required images (see Table 8.2).

9.1.2. Conclusions

Will optimization of the observation schedule of the JANUS instrument to complement the JUICE radiometric tracking data improve the estimation of the ephemerides of the Galilean moons in terms of stability of the solution and the uncertainty in the estimation?

As discussed in the previous section, the inclusion of JUICE-based astrometry using the current observation settings will not result in a reduction of the condition number to a level which is required for accurate generation of the ephemerides. Nevertheless, the condition number is improved by two orders of magnitude with respect to the case in which only radiometric tracking observations are used. Furthermore, the condition number shows substantial variation with the conditional uncertainty of the position of JUICE and the magnitude of the limb-fitting uncertainty (see Section 8.1.1 and 8.1.3). Therefore, different settings can yield different condition numbers which might be sufficient to retain at least one-significant digit. However, varying these settings will, most likely, not substantially improve the condition number with respect to the condition number obtained in this thesis (see Section 8.2).

By observing the distribution of the selected epochs it can be concluded that the inclusion of space-based astrometry is crucial for Io in reducing the condition number. Furthermore, the formal errors of the inner Galilean moons are all improved. However, this improvement was most pronounced for Io which is directly related to the lack of radiometric tracking arcs and the large focus on the optical astrometry of this moon.

Furthermore, a sensitivity analysis on the observation settings showed that in case the VLBI uncertainty can be reduced to $\sigma_{VLBI} = 0.5$ nrad, scheduling a VLBI tracking campaign during the two Europa flybys is beneficial in stabilizing the solution of the normal equations matrix. Moreover, deteriorating the resolution of the JANUS camera to limit the data volume will have a substantial negative impact on the attainable condition numbers and should thus be avoided.

Nevertheless, further research is required as the uncertainty of the astrometric observations is subject to assumptions which have a substantial impact on the corresponding uncertainties. As shown with a sensitivity analysis (in Section 8.1) this also influences the attainable condition numbers. However, it can be concluded that the inclusion of space-based astrometry using the JANUS camera will substantially improve both the quality and stability of the solution. More importantly, it was found that the relative contribution is higher when the JUICE spacecraft has a close proximity to Io. It is recommended to use this knowledge to plan the JANUS astrometry to effectively reduce both the condition number and the formal errors of especially Io.

9.2. Recommendations

Following the conclusions, the recommendations for this thesis are divided among recommendations to improve the uncertainty model for the optical astrometry which is discussed in Section 9.2.1, general recommendations for further research which are discussed in Section 9.2.2, and recommendations for the observation planning of the JUICE mission which are discussed in Section 9.2.3.

9.2.1. Recommendations for the Uncertainty Model for Optical Astrometry

Section 7.4 showed that the modeled uncertainty of the optical astrometry was modeled to be roughly consistent with the results of previous studies. For future research, however, the model which predicts the uncertainty of the astrometric observations should be improved. This encompasses both the pointing and limb-finding uncertainties. The estimation of the pointing uncertainty can be modeled more realistically by using an actual star catalog to retrieve the real number of observable stars with their corresponding magnitude to estimate the pointing uncertainty. This, however, requires a better link between the exposure time, satellite size, and the faintest star that is visible for a certain exposure

time. The data of Cooper et al. (2014) can be used for this purpose as the data-set presented in the supplementary information contains all the aforementioned parameters such that the number of stars can be estimated more accurately. Furthermore, the actual orientation of the spacecraft should be considered such that the uncertainty can be determined for both the right ascension and declination individually.

Moreover, validating the current uncertainty, it was shown that the limb-fitting errors were overestimated for distant images and underestimated for close-by targets. Therefore, the variable weight model of Antreasian et al. (2005) should be fitted to the results of Tajeddine et al. (2015) to find a more realistic representation for the limb-finding uncertainty.

Finally, Cooper et al. (2014) show that using multiple event astrometry (in which two satellites are observed simultaneously) enables elimination, to a large extend, of both the pointing and limb-finding uncertainties. This, however, might be conflicting with the need to image Io at close distances (such that both satellites are not observed simultaneously). Nevertheless, this type of astrometry should be considered in further research.

9.2.2. Recommendations for Further Research

This study has shown that close-by astrometry of Io is required to reduce the condition number most effectively. This knowledge can be used for two purposes in further research. Firstly, the sensitivity analysis as presented in this thesis should be performed considering the epochs at which JUICE has a close proximity with respect to Io. Such a sensitivity analysis would yield a better insight in the attainable condition number as a function of especially the conditional uncertainty of JUICE and the uncertainty in the astrometric observations. Secondly, the concentration of a large number of observations as found in the optimized epochs, is not beneficial in an operational context. Therefore, the influence of dividing the images over a larger number of Io approaches should be considered. Furthermore, the effect of the total number of observations and their respective division over the closest approaches of Io should be further considered, using a method similar to the method employed for the sensitivity analysis in this thesis (see Section 6.3.2).

To get more insight in realistically attainable condition numbers, the actual mission planning should be used considering, among others, available pointing modes and avoiding epochs which are required for downlink. This can be considered by using the instrument kernels as provided on the JUICE SPICE repository.[1]

To address the underlying problem of the high condition number, the method proposed by Dirkx et al. (2017) should be employed in which the radio tracking data of multiple missions (e.g. NASA Juno and Europa Multiple Flyby Mission) should be used to improve the observability of the signature of the dynamics of Europa in the tracking data. In this way, the science return of the individual missions can be improved using the combined data.

As discussed in Section 5.2.3, the current formal errors are overly optimistic. Therefore, in further research, the true estimation error should be estimated given the optimal JANUS observation schedule presented in this thesis. In this case a full least-squares analysis should be employed to more robustly quantify the uncertainties in the estimated states as a function of the respective tracking geometry. Contrary to this thesis, observation biases should be estimated to account for the uncertainty in the positions of the moons (to which the position of the spacecraft is determined). As the contribution of the position uncertainty of the spacecraft is negligible with respect to the uncertainty with which the center-of-figure of a satellite can be determined using optical astrometry, estimating the observation biases is not necessary for the optical astrometry.

9.2.3. Recommendations for the JUICE Observation Planning

As stated in Section 9.1 optical astrometry of Io can substantially reduce the condition number of the normal equations. Optimization of the optical astrometry revealed that the distance between JUICE and the target satellite is the determining variable for the effectiveness of optical astrometry. Therefore, regardless of the actual mission design the closest approaches of Io should be considered for Io astrometry. For the CReMA 3.2 trajectory (trajectory 141a) this means that close JANUS observations should be considered close to the 3G3, 6E1, and 6E2 flybys.

Moreover, to increase the efficiency of the astrometry, the uncertainty should be minimized. There-

[1] `ftp://spiftp.esac.esa.int/data/SPICE/JUICE/kernels` (accessed October 1, 2018)

fore, especially the exposure time should be carefully selected to balance between the need of sufficient reference stars and the need for a bright image which increases the accuracy which with the center-of-figure of the satellite can be determined. For the current mission design, the phase angle is favorable during the closest approaches of Io (< 90 degrees).

Appendix A

This appendix presents all the equations, tables, and figures that are not directly relevant in the report. They are referred to in the main content of this report.

A.1. Geodesy Normalization Geo-potential Coefficients

Given the geo-potential coefficients C_{nm} and S_{nm}, the geodesy normalized coefficients $\bar{C}_{nm}$ and $\bar{S}_{nm}$ are given by Equation A.1.

$$\begin{Bmatrix} \bar{C}_{nm} \\ \bar{S}_{nm} \end{Bmatrix} = \sqrt{\frac{(n+m)!}{(2-\delta_{0m})(2n+1)(n-m)!}} \begin{Bmatrix} C_{nm} \\ S_{nm} \end{Bmatrix} \tag{A.1}$$

In this equation δ_{0m} is the Kronecker symbol for which $\left(\delta_{nm} = \begin{Bmatrix} 1 \\ 0 \end{Bmatrix} for \begin{Bmatrix} n = m \\ n \neq m \end{Bmatrix}\right)$. The resulting acceleration imposed on body i by Jupiter can now be computed using Equation A.2.

$$\ddot{\boldsymbol{r}}_i = \nabla \frac{GM_{\mathrm{♃}}}{r} \sum_{n=0}^{\infty} \sum_{m=0}^{n} \frac{R_{\mathrm{♃}}^n}{r^n} \bar{P}_{nm}(\sin\phi)(\bar{C}_{nm}\cos(m\lambda) + \bar{S}_{nm}\sin(m\lambda)) \tag{A.2}$$

In which $\bar{P}_{nm}$ is the normalized associated Legendre function given by Equation A.3.

$$\bar{P}_{nm} = \sqrt{\frac{(2-\delta_{0m})(2n+1)(n-m)!}{(n+m)!}} P_{nm} \tag{A.3}$$

In which P_{nm} is the unnormalized Legendre function as given in Equation 3.6. As a result of the normalization, $\bar{P}_{nm}$ show a less distinct variation with n and m (Montenbruck and Gill 2012).

A.2. Used Kernels

The SPICE kernels used for the simulation of the dynamics of the Galilean moons are listed below. The kernels can be found on the JUICE SPICE repository. [1] The kernel required for the position of Saturn sat393.bsp can be found on the website of the Navigation and Ancillary Information Facility (NAIF). [2]

Leap Seconds Kernel (LSK)

`naif0012.tls`

[1] `ftp://spiftp.esac.esa.int/data/SPICE/JUICE/kernels` (accessed October 1, 2018)

[2] NAIF "Planetary Data System Navigation Node" naif.jpl.nasa.gov `https://naif.jpl.nasa.gov/pub/naif/generic_kernels/` (accessed October 3, 2018)

Text-style (most) Physical Constants Kernels (PCK)

```
pck00010.tpc
de-403-masses.tpc
gm_de431.tpc
juice_jup000.tpc
```

Spacecraft and Target Body Ephemerides Kernels (SPK)

```
NOE-5-2010-GAL-a.bsp
de406.bsp
jup310.bsp
jup300.bsp
sat393.bsp
juice_mat_crema_3_2_20220601_20330626_v01.bsp
```

A.3. The Galactic Reference Frame

The Galactic longitude l and latitude b can be computed using the equatorial right ascension and declination (α,δ) using Equation A.4 (Poleski 2013).

$$\begin{aligned} \sin b &= \cos\delta\cos\delta_G\cos(\alpha-\alpha_G)+\sin\delta\sin\delta_G \\ \sin(l_{NGP}-l)\cos b &= \cos\delta\sin(\alpha-\alpha_G) \\ \cos(l_{NGP}-l)\cos b &= \sin\delta\cos\delta_g-\cos\delta\sin\delta_G\cos(\alpha-\alpha_G) \end{aligned} \tag{A.4}$$

Where α_G and δ_G are the equatorial coordinates of the Galactic North Pole and l_{NGP} is the Galactic longitude of the Celestial North Pole. The values are given below for respectively α_G, δ_G, and l_{NGP}.

$$\alpha_G = 192.85948^\circ,\ \delta_G = 27.12825^\circ,\ l_{NGP} = 122.93192^\circ$$

A.4. Unit Vector in Equatorial Reference Frame

Equation A.5 gives transformation of the unit vectors in an inertial reference frame to the unit vectors in a spherical reference system. The unit vectors in the inertial reference frame are required to map the conditional uncertainty of the JUICE spacecraft to the synthetic observations as discussed in Section 5.2

$$\begin{bmatrix} \hat{\mathbf{r}} \\ \hat{\boldsymbol{\alpha}} \\ \hat{\boldsymbol{\delta}} \end{bmatrix} = \begin{bmatrix} \cos\alpha\cos\delta & \sin\alpha\cos\delta & \sin\delta \\ -\sin\alpha & \cos\alpha & 0 \\ \cos\alpha\sin\delta & \sin\alpha\sin\delta & -\cos\delta \end{bmatrix} \begin{bmatrix} \hat{\mathbf{x}} \\ \hat{\mathbf{y}} \\ \hat{\mathbf{z}} \end{bmatrix} \tag{A.5}$$

A.5. Comparison of the Saturnian and Galilean Satellites

Table A.1 gives the radii and the geometric albedo for a number of Saturnian moons and for the Galilean moons. These properties are used to select the moons in the Saturnian system which are most appropriate to estimate the performance of space-based astrometry in the Jovian system.

Table A.1: Radius and geometric albedo for both the Saturnian and Galilean satellites. [3]

	Saturnian System					
Satellite	Mimas	Enceladus	Tethys	Dione	Rhea	Iapetus
Radius [km]	198.2	252.1	533.0	561.7	764.3	735.6
Albedo [-]	0.962	1.375	1.229	0.998	2.949	0.6
	Jovian System					
Satellite	Io	Europa	Ganymede	Callisto		
Radius [km]	1821.6	1560.8	2631.2	2410.3		
Albedo [-]	0.63	0.67	0.43	0.14		

A.6. Number of Stars

Figure A.1 shows the number of stars found in the images provided by Tajeddine et al. (2015) observing both Rhea and Tethys as a function of both the Galactic longitude and latitude. It can be observed in Figure A.1(b) that for the images of both Tethys and Rhea more stars are observed in case the camera is pointing close to the Galactic plane (for which the Galactic latitude is close to zero $b = 0$). This behavior is expected as a higher number of stars is concentrated in the Galactic plane (plane of the Milky Way).

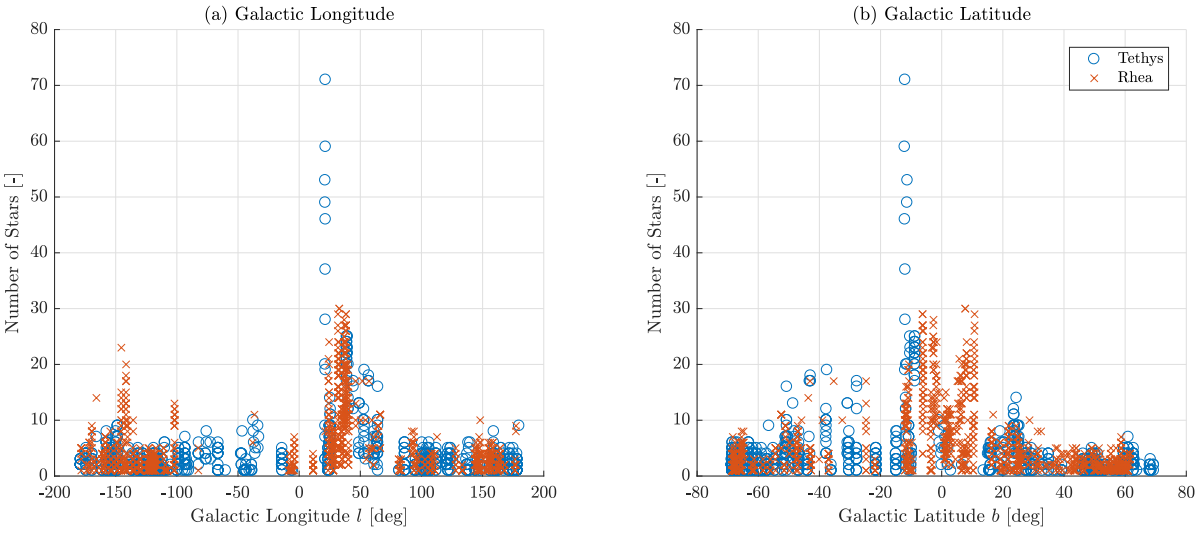

Figure A.1: Galactic longitude and latitude versus number of stars observed in the images of Tethys and Rhea.

Given the direction in which the optical axis of the camera is pointing, the number of stars within field-of-view can be determined using the UCAC2 star catalog (Zacharias et al. 2004). However, the number of stars within field-of-view far exceeds the number of stars actually present in the images provided by Tajeddine et al. (2015). This can be related to the exposure time of the image such that faint stars are not observable. To this end, the maximum apparent magnitude of the faintest star visible within an image is determined to ensure the number of stars observed in the UCAC2 catalog is equal to the number of stars observed in the actual image. Figure A.2(a) shows the misfit between the extracted number of stars and the actual number of observed stars. It can be observed that this misfit is relatively low. Moreover, Figure A.2(b) shows the apparent magnitude of the faintest star. It can be observed that this variable shows a large spread among the different images. The results presented in Figure A.2 are used to acquire the observation settings regarding the exposure time as presented in Section 6.4.4.

[3] Solar System Dynamics "Planetary Satellite Physical Parameters" ssd.jpl.nasa.gov `https://ssd.jpl.nasa.gov/?sat_phys_par#ref28` (accessed October 5, 2018)

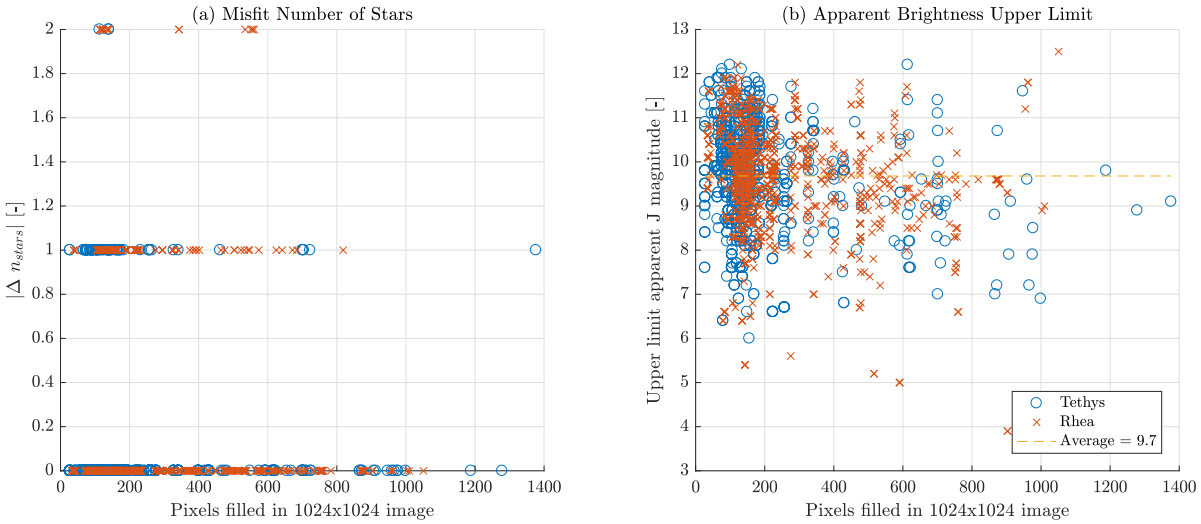

Figure A.2: On the left the misfit between the number of stars found in the UCAC2 catalog and the number of stars actually appearing in the image of Tajeddine et al. (2015) for Tethys and Rhea versus the number of pixels filled by the satellite. On the right the maximum apparent magnitude of the faintest star in the image versus the number of pixels filled by the satellite.

A.7. Propagation Results

Figure A.3 denotes the distance between the Earth and Ganymede. Note that three trends can be observed in this plot.

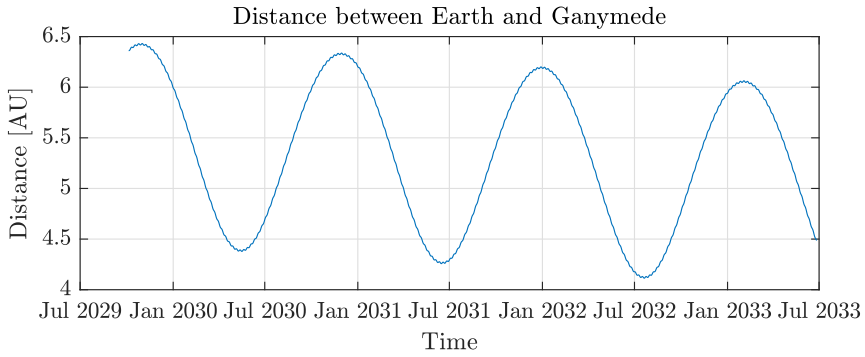

Figure A.3: The distance between the center of the Earth and Ganymede in astronomical units (AU) during the JUICE mission. Note that the time on the x-axis refers to UTC time.

First of all, the largest periodic variation (no full period can be captured during the complete JUICE mission) is due to the eccentricity of the orbit of Jupiter around the Sun with a period of 11.8 years. [4]. The second largest variation (best visible in Figure A.3) is due to the Earth orbiting the Sun at a higher mean orbital motion compared to Jupiter. Therefore, the distance between both planets varies as the solar elongation angle varies between 0 and 180 degrees. Finally, the smallest variation is due to the orbit of Ganymede around Jupiter (hardly visible in this figure but best visible during solar occultation and solar opposition of Jupiter with respect to the Earth).

A.8. Progression of the Condition number and Formal Errors during the Optimization

Figure A.4 shows the progression of both the condition number (Figure A.4(a) and the norm of the formal error of the position of Io (Figure A.4) over the number of generations. Note that the most substantial

[4] NASA Solar System Dynamics "Planets and Pluto: Physical Characteristics" ssd.jpl.nasa.gov `https://ssd.jpl.nasa.gov/?planet_phys_par` (accessed October 16, 2018)

improvement is realized in the first 2000 generations. In the last 6000 generations only a very small improvement is realized, which is in line with the relative improvement as presented in Figure 7.9(b).

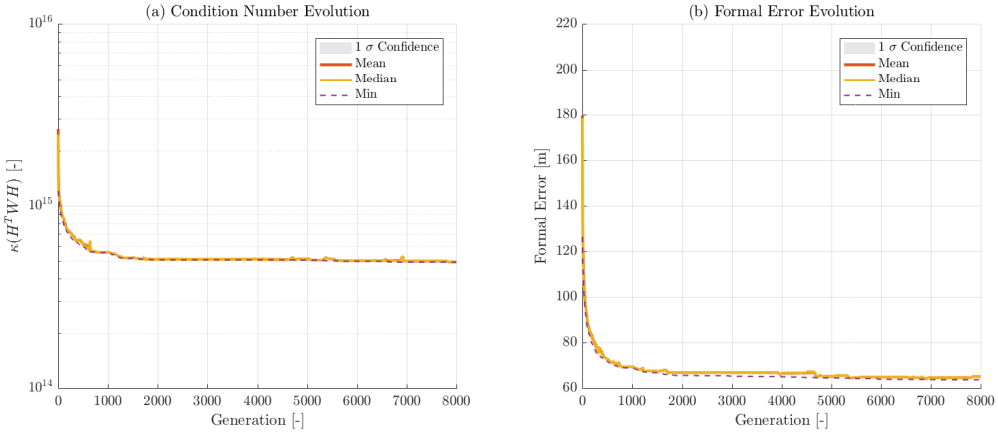

Figure A.4: Figure(a) shows the evaluation of the condition number over the number of generations. Note that the minimum, mean, median and 1σ confidence region are given. Figure(b) shows the evolution of the norm of the formal error in meters of the position of Io with the number of generations.

A.9. Partial Derivatives of the Space-Based Astrometry

Figure A.5 shows the norm of the partial derivative of the position of Io, Europa, and Ganymede for the complete Jovian tour. Note that the red boxes indicate the JANUS epochs as selected by the optimization epoch.

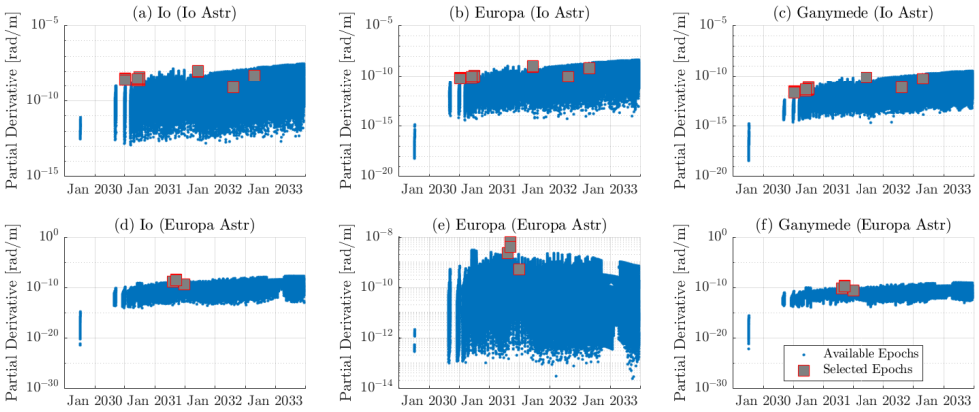

Figure A.5: The norm of the unweighted partial derivatives of the positions of Io, Europa, and Callisto. The partial derivatives refer to the JANUS astrometry of Io. The red squares denote the selected epochs for JANUS astrometry as found by the optimization algorithm. Note that the y-axis has a different scale for all different plots.

A.10. Uncertainty Model Analysis

Figure A.6 shows the difference between the uncertainty of the astrometric observations of Mimas and Enceladus on one hand (generated by Tajeddine et al. (2013) and Tethys and Rhea on the other hand (generated by Tajeddine et al. (2015). Note that the former show a systematic bias in the direction which is not present for the latter as a result of a limb fitting algorithm which is set to a higher sensitivity for images with higher phase angles.

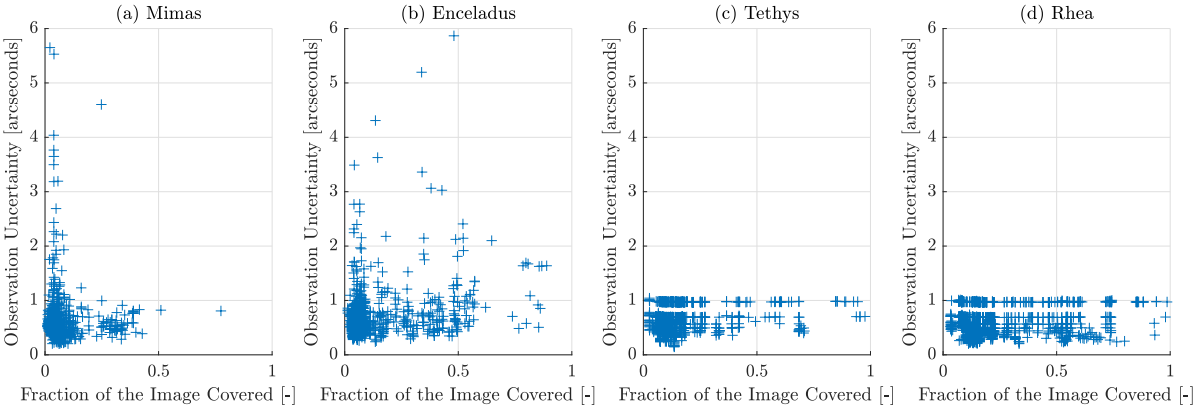

Figure A.6: The total astrometric uncertainty in arcseconds for the Saturnian moons Mimas, Enceladus, Tethys, and Rhea as a function of the fraction of the image which is filled by the satellite. This fraction is calculated by dividing the diameter of the moon by the width of the image in kilometers.

Bibliography

Alessi, E. M., Cicalo, S., Milani, A. and Tommei, G. (2012), 'Desaturation manoeuvres and precise orbit determination for the bepicolombo mission', *Monthly Notices of the Royal Astronomical Society* **423**(3), 2270–2278.

Antreasian, P., Ardalan, S., Bordi, J., Criddle, K., Ionasescu, R., Jacobson, R., Jones, J., MacKenzie, R., Parcher, D., Pelletier, F. et al. (2008), Cassini orbit determination results january 2006-end of prime mission, *in* 'AIAA/AAS Astrodynamics Specialist Conference and Exhibit', p. 6747.

Antreasian, P., Bordi, J., Criddle, K., Ionasescu, R., Jacobson, R., Jones, J., MacKenzie, R., Meek, M., Pelletier, F., Roth, D. et al. (2005), 'Cassini orbit determination performance during the first eight orbits of the saturn satellite tour', *Advances in the Astronautical Sciences* **312**(5).

Archinal, B. A., A'Hearn, M. F., Bowell, E., Conrad, A., Consolmagno, G. J., Courtin, R., Fukushima, T., Hestroffer, D., Hilton, J. L., Krasinsky, G. A. et al. (2011), 'Report of the iau working group on cartographic coordinates and rotational elements: 2009', *Celestial Mechanics and Dynamical Astronomy* **109**(2), 101–135.

Arlot, J.-E., Desmars, J., Lainey, V. and Robert, V. (2012), 'The astrometry of the natural planetary satellites applied to their dynamics before and after gaia', *Planetary and Space Science* **73**(1), 66–69.

Beesley, J. E. (2001), *Immunocytochemistry and in situ hybridization in the biomedical sciences*, number 577.27 IMM, Springer.

Beser, N. D. (1994), 'Space data compression standards.', *Johns Hopkins APL Technical Digest* **15**, 206–223.

Bocanegra-Bahamón, T., Calvés, G. M., Gurvits, L., Duev, D., Pogrebenko, S., Cimò, G., Dirkx, D. and Rosenblatt, P. (2018), 'Planetary radio interferometry and doppler experiment (pride) technique: A test case of the mars express phobos flyby-ii. doppler tracking: Formulation of observed and computed values, and noise budget', *Astronomy & Astrophysics* **609**(A59).

Border, J. S. and Koukos, J. A. (1993), 'Technical characteristics and accuracy capabilities of delta differential one-way ranging (deltador) as a spacecraft navigation tool'.

Boué, G., Correia, A. C. and Laskar, J. (2016), 'Complete spin and orbital evolution of close-in bodies using a maxwell viscoelastic rheology', *Celestial Mechanics and Dynamical Astronomy* **126**(1-3), 31–60.

Boutonnet, A. and Varga, G. (2017), Juice - jupiter icy moons explorer consolidated report on mission analysis (crema), CReMA 3.2 - JUI-ESOC-MOC-RP-001, European Space Operations Centre. Unpublished - ESA Unclassified - For Official Use.

Boutonnet, A., Varga, G., Rocchi, A., Martens, W. and Mackenzie, R. (2018), Juice - jupiter icy moons explorer consolidated report on mission analysis (crema), CReMA 4.0 - JUI-ESOC-MOC-RP-001, European Space Operations Centre. Unpublished - ESA Unclassified - For Official Use.

Cassen, P., Peale, S. J. and Reynolds, R. T. (1980), 'On the comparative evolution of ganymede and callisto', *Icarus* **41**(2), 232–239.

Cheney, E. W. and Kincaid, D. R. (2012), *Numerical mathematics and computing*, Cengage Learning.

Cicalò, S., Schettino, G., Di Ruzza, S., Alessi, E., Tommei, G. and Milani, A. (2016), 'The bepicolombo more gravimetry and rotation experiments with the orbit14 software', *Monthly Notices of the Royal Astronomical Society* **457**(2), 1507–1521.

Coello, C. A. C., Dhaenens, C. and Jourdan, L. (2010), Multi-objective combinatorial optimization: Problematic and context, *in* 'Advances in multi-objective nature inspired computing', Springer, pp. 1–21.

Cooper, N., Murray, C., Lainey, V., Tajeddine, R., Evans, M. and Williams, G. (2014), 'Cassini iss mutual event astrometry of the mid-sized saturnian satellites 2005–2012', *Astronomy & Astrophysics* **572**, A43.

Curkendall, D. W. and Border, J. S. (2013), 'Delta-dor: The one-nanoradian navigation measurement system of the deep space network—history, architecture, and componentry', *The Interplanetary Network Progress Report* **42**, 193.

Darwin, G. H. (1880), 'On the secular changes in the elements of the orbit of a satellite revolving about a tidally distorted planet', *Philosophical Transactions of the Royal Society of London* **171**, 713–891.

Deb, K. (2001), *Multi objective optimization using evolutionary algorithms*, John Wiley and Sons.

Deb, K., Pratap, A., Agarwal, S. and Meyarivan, T. (2002), 'A fast and elitist multiobjective genetic algorithm: Nsga-ii', *IEEE transactions on evolutionary computation* **6**(2), 182–197.

Dirkx, D. (2015), Interplanetary Laser Ranging, PhD thesis, Delft University of Technology.

Dirkx, D., Gurvits, L. I., Lainey, V., Lari, G., Milani, A., Cimò, G., Bocanegra-Bahamon, T. M. and Visser, P. N. (2017), 'On the contribution of PRIDE-JUICE to Jovian system ephemerides', *Planetary and Space Science* **147**(September), 14–27.

Dirkx, D., Lainey, V., Gurvits, L. I. and Visser, P. (2016), 'Dynamical modelling of the galilean moons for the juice mission', *Planetary and Space Science* **134**, 82–95.

Dirkx, D., Prochazka, I., Bauer, S., Visser, P., Noomen, R., Gurvits, L. I. and Vermeersen, B. (2018), 'Laser and radio tracking for planetary science missions—a comparison', *Journal of Geodesy* pp. 1–16.

Duxbury, T. and Callahan, J. (1981), 'Pole and prime meridian expressions for phobos and deimos', *The Astronomical Journal* **86**, 1722–1727.

Efroimsky, M. and Lainey, V. (2007), 'Physics of bodily tides in terrestrial planets and the appropriate scales of dynamical evolution', *Journal of Geophysical Research: Planets* **112**(E12).

Farebrother, R. W. (1988), *Linear least squares computations*, Marcel Dekker, Inc.

Ferraz-Mello, S., Rodríguez, A. and Hussmann, H. (2008), 'Tidal friction in close-in satellites and exoplanets: The darwin theory re-visited', *Celestial Mechanics and Dynamical Astronomy* **101**(1-2), 171–201.

Folkner, W., Iess, L., Anderson, J., Asmar, S., Buccino, D., Durante, D., Feldman, M., Gomez Casajus, L., Gregnanin, M., Milani, A. et al. (2017), 'Jupiter gravity field estimated from the first two juno orbits', *Geophysical Research Letters* **44**(10), 4694–4700.

Folkner, W. M., Williams, J. G., Boggs, D. H., Park, R. S. and Kuchynka, P. (2014), 'The planetary and lunar ephemerides de430 and de431', *Interplanet. Netw. Prog. Rep* **196**, 1–81.

Golub, G. H. and Van Loan, C. F. (2012), *Matrix computations*, Vol. 3, JHU Press.

Grasset, O., Dougherty, M. K., Coustenis, A., Bunce, E. J., Erd, C., Titov, D., Blanc, M., Coates, A., Drossart, P., Fletcher, L. N., Hussmann, H., Jaumann, R., Krupp, N., Lebreton, J. P., Prieto-Ballesteros, O., Tortora, P., Tosi, F. and Van Hoolst, T. (2013), 'JUpiter ICy moons Explorer (JUICE): An ESA mission to orbit Ganymede and to characterise the Jupiter system', *Planetary and Space Science* **78**, 1–21.

Gratton, S. (1996), 'On the condition number of linear least squares problems in a weighted frobenius norm', *BIT Numerical Mathematics* **36**(3), 523–530.

Greenberg, R. (1987), 'Galilean satellites: Evolutionary paths in deep resonance', *Icarus* **70**(2), 334–347.

Greenberg, R. (2010), 'The icy Jovian satellites after the Galileo mission', *Reports on Progress in Physics* **73**(3), 036801.

Halim, A. H. and Ismail, I. (2017), 'Combinatorial optimization: Comparison of heuristic algorithms in travelling salesman problem', *Archives of Computational Methods in Engineering* pp. 1–14.

Hull, T., Enright, W., Fellen, B. and Sedgwick, A. (1972), 'Comparing numerical methods for ordinary differential equations', *SIAM Journal on Numerical Analysis* **9**(4), 603–637.

Hussmann, H., Choblet, G., Lainey, V., Matson, D. L., Sotin, C., Tobie, G. and Van Hoolst, T. (2010), 'Implications of rotation, orbital states, energy sources, and heat transport for internal processes in icy satellites', *Space science reviews* **153**(1-4), 317–348.

Iess, L., Di Benedetto, M., James, N., Mercolino, M., Simone, L. and Tortora, P. (2014), 'Astra: Interdisciplinary study on enhancement of the end-to-end accuracy for spacecraft tracking techniques', *Acta Astronautica* **94**(2), 699–707.

Iess, L., Folkner, W., Durante, D., Parisi, M., Kaspi, Y., Galanti, E., Guillot, T., Hubbard, W., Stevenson, D., Anderson, J. et al. (2018), 'Measurement of jupiter's asymmetric gravity field', *Nature* **555**(7695), 220.

Jacobson, R. A. (2001), The Gravity Field of the Jovian System and the Orbits of the Regular Jovian Satellites, *in* 'AAS/Division for Planetary Sciences Meeting Abstracts #33', Vol. 33, p. 11.01.

Jones, D. L., Folkner, W. M., Jacobson, R. A., Jacobs, C. S., Dhawan, V., Romney, J. and Fomalont, E. (2015), 'Astrometry of cassini with the vlba to improve the saturn ephemeris', *The Astronomical Journal* **149**(1), 28.

JUICE Science Study Team (2012), Juice assessment study report (yellow book), Technical report, ESA/SRE (2011).
URL: *http://sci.esa.int/juice/49837-juice-assessment-study-report-yellow-book/*

JUICE Science Study Team (2014), Juice assessment study report (red book), Technical report, ESA/SRE(2014).
URL: *http://sci.esa.int/juice/54994-juice-definition-study-report/*

Kaplan, G. H. (2011), 'Time scales in astronomical and navigational almanacs', *Science and Technology Series* **113**, 201–214.

Kaula, W. M. (1964), 'Tidal dissipation by solid friction and the resulting orbital evolution', *Reviews of Geophysics* **2**(4), 661–685.

Lainey, V., Arlot, J. E., Karatekin, Ö. and Van Hoolst, T. (2009), 'Strong tidal dissipation in Io and Jupiter from astrometric observations', *Nature* **459**(7249), 957–959.

Lainey, V., Arlot, J. and Vienne, A. (2004), 'New accurate ephemerides for the galilean satellites of jupiter-ii. fitting the observations', *Astronomy & Astrophysics* **427**(1), 371–376.

Lainey, V., Dehant, V. and Pätzold, M. (2007), 'First numerical ephemerides of the martian moons', *Astronomy & Astrophysics* **465**(3), 1075–1084.

Lainey, V., Duriez, L. and Vienne, A. (2004), 'New accurate ephemerides for the galilean satellites of jupiter-i. numerical integration of elaborated equations of motion', *Astronomy & Astrophysics* **420**(3), 1171–1183.

Lainey, V., Duriez, L. and Vienne, A. (2006), 'Synthetic representation of the galilean satellites' orbital motions from l1 ephemerides', *Astronomy & Astrophysics* **456**(2), 783–788.

Lam, T., Buffington, B. and Campagnola, S. (2018), A robust mission tour for nasa's planned europa clipper mission, *in* '2018 Space Flight Mechanics Meeting', p. 0202.

Lanyi, G., Bagri, D. S. and Border, J. S. (2007), 'Angular position determination of spacecraft by radio interferometry', *Proceedings of the IEEE* **95**(11), 2193–2201.

Lari, G. (2018), 'A semi-analytical model of the galilean satellites' dynamics', *arXiv preprint arXiv:1802.07878* .

Li, H. and Zhang, Q. (2009), 'Multiobjective optimization problems with complicated pareto sets, moea/d and nsga-ii', *IEEE Transactions on evolutionary computation* **13**(2), 284–302.

Liebe, C. C. (1995), 'Star trackers for attitude determination', *IEEE Aerospace and Electronic Systems Magazine* **10**(6), 10–16.

Majid, W. A. and Bagri, D. S. (2008), Precision spacecraft tracking using in-beam phase referencing, *in* 'Aerospace Conference, 2008 IEEE', IEEE, pp. 1–7.

Malkin, Z., Jacobs, C., Arias, F., Boboltz, D., Böhm, J., Bolotin, S., Bourda, G., Charlot, P., De Witt, A., Fey, A. et al. (2015), 'The icrf-3: Status, plans, and progress on the next generation international celestial reference frame', *arXiv preprint arXiv:1511.08035* .

Meyer, C. D. (2000), *Matrix analysis and applied linear algebra*, Vol. 71, Siam.

Milani, A. and Gronchi, G. (2010), *Theory of orbit determination*, Cambridge University Press.

Montenbruck, O. and Gill, E. (2012), *Satellite orbits: models, methods and applications*, Springer Science & Business Media.

Murray, C. D. and Dermott, S. F. (1999), *Solar system dynamics*, Cambridge university press, 32 Avenue of the Americas, New York, NY 10013-2473, USA.

Pasewaldt, A., Oberst, J., Willner, K., Wählisch, M., Hoffmann, H., Matz, K.-D., Roatsch, T., Hussmann, H. and Lupovka, V. (2012), 'New astrometric observations of deimos with the src on mars express', *Astronomy & Astrophysics* **545**, A144.

Petit, G. and Luzum, B. (2010), Iers conventions (2010), Technical report, BUREAU INTERNATIONAL DES POIDS ET MESURES SEVRES (FRANCE).

Poleski, R. (2013), 'Transformation of the equatorial proper motion to the galactic system', *arXiv preprint arXiv:1306.2945* .

Prince, P. J. and Dormand, J. R. (1981), 'High order embedded runge-kutta formulae', *Journal of Computational and Applied Mathematics* **7**(1), 67–75.

Schäff, S. and Wiegand, A. (2015), Advanced electric orbit-raising optimization for operational purpose, *in* 'Proceedings of the 25th International Symposium on Space Flight Dynamics', DLR Space Operations Munich.

Schubert, G., Anderson, J., Spohn, T. and McKinnon, W. (2004), 'Interior composition, structure and dynamics of the galilean satellites', *Jupiter: The planet, satellites and magnetosphere* **1**, 281–306.

Schubert, G., Hussmann, H., Lainey, V., Matson, D., McKinnon, W., Sohl, F., Sotin, C., Tobie, G., Turrini, D. and Van Hoolst, T. (2010), 'Evolution of icy satellites', *Space Science Reviews* **153**(1-4), 447–484.

Schutz, B., Tapley, B. and Born, G. H. (2004), *Statistical orbit determination*, Elsevier.

Showman, A. P. and Malhotra, R. (1999), 'The galilean satellites', *Science* **286**(5437), 77–84.

Showman, A. P., Stevenson, D. J. and Malhotra, R. (1997), 'Coupled orbital and thermal evolution of ganymede', *Icarus* **129**(2), 367–383.

Strange, N., Goodson, T. and Hahn, Y. (2002), Cassini tour redesign for the huygens mission, *in* 'AIAA/AAS Astrodynamics Specialist Conference and Exhibit', p. 4720.

Tajeddine, R., Cooper, N., Lainey, V., Charnoz, S. and Murray, C. (2013), 'Astrometric reduction of cassini iss images of the saturnian satellites mimas and enceladus', *Astronomy & Astrophysics* **551**, A129.

Tajeddine, R., Lainey, V., Cooper, N. and Murray, C. (2015), 'Cassini iss astrometry of the saturnian satellites: Tethys, dione, rhea, iapetus, and phoebe 2004–2012', *Astronomy & Astrophysics* **575**, A73.

Thomas, P., Burns, J., Helfenstein, P., Squyres, S., Veverka, J., Porco, C., Turtle, E., McEwen, A., Denk, T., Giese, B. et al. (2007), 'Shapes of the saturnian icy satellites and their significance', *Icarus* **190**(2), 573–584.

Thornton, C. L. and Border, J. S. (2003), *Radiometric tracking techniques for deep-space navigation*, John Wiley & Sons.

Wakker, K. F. (2015), 'Fundamentals of astrodynamics'.

Wang, H., Tu, C. and Chen, K. (2015), 'Supplier selection and production planning by using guided genetic algorithm and dynamic nondominated sorting genetic algorithm ii approaches', *Mathematical Problems in Engineering* **2015**.

Weise, T. (2009), 'Global optimization algorithms-theory and application', *Self-published* **2**.

Yoder, C. F. (1979), 'How tidal heating in io drives the galilean orbital resonance locks', *Nature* **279**(5716), 767–770.

Zacharias, N., Urban, S. E., Zacharias, M. I., Wycoff, G. L., Hall, D. M., Monet, D. G. and Rafferty, T. J. (2004), 'The second us naval observatory ccd astrograph catalog (ucac2)', *The Astronomical Journal* **127**(5), 3043.